공학박사학위논문

Modeling of Combustion and Emission Characteristics in a Dual-fuel Engine by Combining Diffusion and Premixed Combustion

확산 연소와 예혼합 연소의 결합을 통한
혼소 연소 엔진의 연소 및 배기 배출물 모델링

2013 년 2 월

서울대학교 대학원

협동과정 자동차공학

이 상 열

Modeling of Combustion and Emission Characteristics in a Dual-fuel Engine by Combining Diffusion and Premixed Combustion

지도교수 민 경 덕

이 논문을 공학박사 학위논문으로 제출함

2013 년 2 월

서울대학교 대학원

협동과정 자동차공학

이 상 열

이상열의 공학박사 학위논문을 인준함

2013 년 2 월

위 원 장 고 상 근 (인)

부위원장 민 경 덕 (인)

위 원 차 석 원 (인)

위 원 송 한 호 (인)

위 원 김 득 상 (인)

Acknowledgements

This project on my Ph.D thesis would not be happened without the advices and helps of following people.

First and foremost, I would like to express my respect and gratitude to my advisor, Professor Kyoungdoug Min. During the graduate course, my knowledge and personality were grown up with his invaluable advices. He gave the inspirations of this study and his guidance and encouragement were the source of power overcoming many difficulties during the project.

I would like to special thanks to the project members who offered assistance, valuable discussions and beautiful memories of friendship. Kyeonghyeon Lee, Won-ah Park, Joohan Kim and Gyujin Kim assisted lots of the study. Dr. Hyuksun Kwon and Dr. Jaeman Lim also gave basic knowledge and inspirations as a senior. This work would never have been achieved without their efforts and patients. Also, I'd like to thanks to my graduate schoolmate Joonhyun Cho for unforgettably joyful lab life.

I would like to present my deepest respect and gratitude to my parents, Sungsoon Lee and Jeongyeon Kim, for their great sacrifice, thoughtful consideration, unimaginable patience, and endless love. My beloved wife, Hyerim Ha was my emotional anchor and supported my long school days with infinite faith and boundless love. It was, it is, and it will be the greatest happiness in my life to be with her. *I love you*.

Abstract

Modeling of Combustion and Emission Characteristics in a Dual-fuel Engine by Combining Diffusion and Premixed Combustion

Sangyul Lee
Interdisciplinary Program in Automotive Engineering
The Graduate School
Seoul National University

Dual-fuel combustion is a combustion concept which uses a split injection strategy where the second injected fuel is used as an ignition trigger and the first injected fuel is used as heat release. Classical dual-fuel combustion has been studied for a long time to reduce the usage of liquid fuel. Recently, the dual-fuel combustion concept is coupled with the HCCI combustion concept and it receives much attention. However, the numerical approach to the dual-fuel combustion needs a great deal of calculation costs because there is no dual-fuel combustion models so they solve chemical kinetic directly. Classical dual-fuel combustion uses liquid fuel and RCCI combustion uses higher reactivity fuel as an ignition trigger and combustion propagates from the ignition source although the specific combustion behaviors are different to each other. Therefore, the dual-fuel combustion could be arranged into the couple of diffusion flame characteristics and premixed flame characteristics. In this study, dual-fuel combustion and emission models were developed from the laminar flamelet

model which could describe the diffusion flame and from the level-set model which could describe the premixed flame.

At first, the laminar flamelet model was applied to describe the diffusion combustion in dual-fuel combustion. The second injected fuel is ignited by the high temperature and pressure without spark plug during the compression stroke. In addition, the first injected fuel has a possibility to auto-ignite by the high temperature, pressure and radicals. By the early injection, multiple ignition points could be generated and it was also described in this study.

Secondly, the level-set model was applied to the combustion model to describe the combustion propagation. The flame propagation speed was determined by competition between ignition propagation speed by the flamelet model and flame propagation speed by the level-set model. The burned gas composition and flame brush species composition were pre-calculated by the flamelet solution database.

This new model was preliminary applied to a simple planar geometry to investigate the fundamentals of model behavior. In this two-dimensional mesh, the combustion model described the ignition of the higher reactivity fuel and flame propagation to the lower reactivity fuel. Then, three-dimensional CFD simulations were performed in a practical engine mesh. The simulation results were compared with the experimental data and showed a very good agreement with experimental cylinder pressure curve. The predicted levels of NOx, soot, and THC emissions showed reasonable agreement to the experimental data.

Keywords: dual-fuel combustion engine, three-dimensional CFD simulation, flamelet model, level-set model, NOx emission, soot emission, dual-fuel combustion model

Student Number: 2008-30291

List of Tables

List of Figures

Acronym

CFD	Computational Fluid Dynamics
RIF	Representative Interactive Flamelet
PM	Particulate Matter
HSDI	High Speed Direct Injection
HCCI	Homogeneous Charge Compression Ignition
SOC	Start of Combustion
SOI	Start of Injection
EOI	End of Injection
TDC	Top Dead Center
BTDC	Before TDC
ATDC	After TDC
RCCI	Reactivity Controlled Compression Ignition
(I)DI	(In)Direct Injection
CAD	Crank Angle Degree
CI	Compression Ignition
SI	Spark Ignition
LHV	Low Heating Value
BMEP	Brake Mean Effective Pressure
AF ratio	Air-Fuel ratio

Chapter 1. Introduction

1.1 Backgrounds and Motivations

1.1.1 Overview

Globally, there are two big issues to the automotive engineers, one is efficiency due to rising oil prices and the other is emissions due to strict emission regulations. Figure 1.1.1 shows the monthly averaged crude oil prices since May 1987. During the most of this period, the prices had been rising continuously and finally recent price is about 3 times greater than that of 10 years ago. By this reason, fuel efficiency needs to be improved than before. Meanwhile, Figure 1.1.2 shows the European emissions standards for heavy duty Diesel engines. First introduced in 1992, the European emissions regulations for on-load Diesel engines are commonly referred to as Euro 1 through Euro 5. Emissions regulations of vehicles exist not only in Europe but also in USA (Tier), Japan and Korea, etc. Therefore, reduction techniques of emissions should be improved to reduce automotive emissions. Compared to the gasoline engine, Diesel engine shows higher efficiency due to the higher compression ratio and unthrottled operation. However, combustion noise, vibrations, harshness and emissions such as NOx from the high combustion temperature by diffusion flame and particulate matter (PM) from rich fuel spray are the weaknesses of Diesel engines compared to the gasoline engines. In contrast, gasoline engines could solve the most problems about the engine-out emissions using 3-way catalyst but the fuel efficiency is lower than Diesel engines.

Many researchers have been investigated to acquire the advantages of premixed combustion of gasoline engines and diffusion combustion of Diesel engines simultaneously. In case of gasoline engines, gasoline direct injection (GDI) to the in-

cylinder, instead of port injection, could almost obtain the same level of efficiency to Diesel engines with the specific power of the gasoline engine [1-3] . In case of Diesel engines, improved spray equipment such as common rail or piezo injector and injection strategies such as multiple injections are the key factor of improving the fuel efficiency and engine-out emissions. It is called as high speed direct injection (HSDI) Diesel engine [4-6].

Additional after-treatment systems to reduce the tail-pipe emissions as well as engine itself also have been investigated widely. DPF (Diesel Particulate Filter), LNT (Lean NOx Filter), NSC (NOx Storage Catalyst) and urea SCR (Selective Catalyst Reduction) were developed to reduce NOx or PM. Although they show good emission reduction, they may increase vehicle's weight, complicate vehicle systems and increase vehicle costs [7].

Some researchers have focused on the low temperature combustion, neither a premixed combustion nor diffusion combustion. Homogeneous charged compression Ignition (HCCI) engine is the typical combustion concept to realize the low temperature combustion [8-10]. Early injection timing could make homogeneous lean air-fuel mixture and the mixture is compressed during the compression stroke. The pressure and temperature of this homogeneous lean mixture is high and then it ignites at the overall in-cylinder region by chemistry. This concept produces much less PM and NOx emissions. The lean mixture produces much less PM than Diesel engine combustion. The low combustion temperature of HCCI concept produces much less NOx emission than gasoline or Diesel engine combustion. In addition, the efficiency of HCCI combustion is as good as the efficiency of Diesel engine because of high compression ratio and no throttling loss. However, HCCI concept has some problems to apply to the real engine. The SOC (Start of Combustion) timing and heat release rate are hard to control because ignition starts by only chemistry, not by injection timing or spark timing. In addition, very short combustion duration could make much noise and damage the engine cylinder. Wall wetting of the fuel spray due to the early injection could also be a

problem. Therefore, a huge number of techniques and modified HCCI concepts have been developed. UNIBUS separated the main injection into two, so the first injection was used as an early injection and the second injection was used as an ignition trigger [11]. They could control the SOC timing with this method. Recently, partially premixed charged compression ignition (PPCCI) concepts are studied widely [12-14]. They use somewhat early injection timing but not too early as HCCI concept. This could mitigate the limitations of HCCI concepts in part as documented above.

1.1.2 Potentials of Dual-Fuel Engine

Unexpectedly, the dual-fuel system has a very long history. Due to limited resources of fossil fuels, alternative solutions have been proposed by many researchers at the beginning of the 19th century. The origin of dual-fueled system was developed for this reason. Cave in 1929 and Helmore and Sokes in 1930 performed the earliest experiments on dual-fuel system that used hydrogen as a secondary fuel in Diesel engines and they saved 20% of Diesel fuel [15]. Due to the shortage of liquid fuels, many researchers had worked to develop the dual-fuel engines during World War II.

Until recently, researches about dual-fuel engine have been studied very actively. Lots of researches for the efficiency and emissions have been studied under various engine speed and load conditions. The effect of load on combustion noise for the Diesel and dual fuel engine at an engine speed of 1200 rpm was examined by Selim [16]. Concentration of pollutant was investigated with Diesel alone and dual-fuel mode at different loads (10, 20, 30 and 40 kW) by Uma et. al. [17]. Papagiannakis and Hountalas investigated to examine the effect of dual fuel combustion on the performance and pollutant emissions of a DI Diesel engine experimentally [18]. Mansour et. al. measured the emission and performance levels with respect to the engine speed on a chassis dynamometer under steady and

unsteady conditions [19]. Selim examined the effect of engine speed on combustion noise, torque, peak pressure and thermal efficiency of the dual fuel engine and Diesel cases [16]. The effect of advanced injection timing on the performance of natural gas used as primary fuel in dual-fuel combustion has been examined by Nwafor [20].

Pilot injection timings or mass quantities were investigated also. Abd et. al. investigated the effects of injection timings at BTDC 25, 27.5, 30 CAD (Crank Angle Degree) on the performance of an IDI Diesel engine in order to improve thermal efficiency and fuel efficiency at the low load conditions [21]. Krishnan et. al. tried different pilot injection timings in a single cylinder CI engine to achieve low NOx and good fuel efficiency from pilot ignited natural gas combustion [22]. Selim compared the effect of pilot Diesel injection timing and injected mass on the combustion noise (maximum pressure rise rate during combustion) of a dual fuel engine to 100% Diesel case [23]. Nwafor examined the effect of advanced injection timing on the performance of natural gas used as primary fuel in dual-fuel combustion [24].

Aside from these researches, Kusaka et. al. varied the intake manifold temperature and examined the thermal efficiency. Selim [16] also studied about the engine combustion noise and peak pressure with various types of fuels. Papagiannakis and Hountalas also experimented types of fuels and verified their effects to the engine performance and emissions [18]. In addition to these studies, a number of researches have been studied with various fuel combinations.

Recently, Reactivity controlled compression ignition (RCCI) combustion concept has been studied widely [25-30]. RCCI is a variant of HCCI combustion because it uses early injection timing to optimize combustion phasing, duration and magnitude based on HCCI combustion concept. Nevertheless, RCCI is also a variant of dual-fuel combustion because it uses two different fuels which have different reactivity to control the fuel reactivity. Generally, it uses lower reactivity gasoline

fuel as a primary fuel and small quantity of higher reactivity Diesel fuel in Diesel engines with a gasoline injector in intake manifold. It could produce low NOx and soot emissions simultaneously. More detail combustion characteristics of RCCI combustion would be described in the Chapter 1.2.1.

1.1.3 Numerical Approach as an Engine Development Tool

Computational fluid dynamics (CFD) has been an essential tool in engine development thanks to the advancement in computational power and accuracy of numerical models during the last decade [31-33]. In CFD, the parameters of engine operating conditions could be set freely, and the isolation of dependent and independent variables is easily done. Furthermore, the results of CFD analysis provide a set of detailed information on the physical and thermodynamic variables, and an arbitrary number of measurement points could be located in the analysis domain without any perturbations on the fluid field. In addition, the experiments with extreme conditions could be performed without any risks and virtual production of prototypes with arbitrary configuration is possible with low cost.

To observe spray behavior, velocity field, temperature distribution and flame surface location of the in-cylinder, it requires a lot of cost and exhaustive efforts experimentally. In CFD, not only those variables but also species distribution could be observed by solving the governing equations.

To obtain meaningful solutions from the CFD analysis, accurate numerical models implemented in the analysis should be ensured. Dual-fuel combustion is complicated and interconnected with each other that include turbulent flow, gaseous or liquid fuel injection, ignition of fuel-air mixtures, propagation, chemical reactions including fuel oxidation, and pollutant formations with the moving mesh describes a real engine. Therefore, the modeling of dual-fuel combustion requires delicate integration of the individual models as well as the accurate descriptions of the

individual physics. In this research, several numerical models are developed newly, that describe the turbulent flame ignition, propagation and complex chemical reaction system of dual fuel engine, and they are integrated into a combustion and emission model for a dual fuel engine.

1.1.4 History and Limitations of Numerical Models for the Dual Fuel Combustion

Model for dual-fuel combustion has not been studied widely due to its complicate combustion behavior and expensive computational cost of two types of fuels. Zhang et. al. used multi-dimensional CFD to study about the Diesel-Natural gas dual-fuel engine [34]. The Shell model was used as a simplified reaction mechanism to simulate the auto-ignition of hydrocarbon fuels. The mechanism consisted of five generic species and eight generic reactions representing the initiation, propagation, branching and termination steps. The five generic species included fuel, oxygen, radicals, intermediate species and branching agents. This ignition model needs to be tuned the model constant to match the ignition delay time and apparent heat release rate for gasoline and Diesel fuels. After the ignition process (i.e., when the local gas temperature is greater than 1200 K), the characteristics time combustion (CTC) model simulated the subsequent high temperature combustion. The CTC model calculated the equilibrium concentration of each species and the corresponding laminar and turbulent characteristic times to determine species conversion rates. Seven major species are considered: fuel, oxygen, nitrogen, carbon dioxide, hydrogen, vapor and carbon monoxide. They showed not perfect but good results compared to the experimental results.

Tamagna *et. al*. studied PCCI combustion with gasoline and Diesel fuels using the same methods as before [35]. They showed more accurate pressure and apparent heat release rate with respect to the time compared to the experimental results.

However, it needs some simulation constant to match the experimental results. In addition, emission trends (NOx, CO, CO2, HC) were not matched with the experimental results.

Recently, simulation researches for RCCI combustion were studied widely [26, 28, 36, 37]. They used detailed chemistry to predict the emissions such as NOx and soot as well as pressure and heat release rate. However, detailed chemistry could not be applied directly due to the expensive calculation cost. Therefore, they used adaptive multi-grid chemistry (AMC) model of Shi *et. al.* [38]. This method could reduce calculation time more than a factor of three while maintaining an accurate prediction of the emissions results [39]. This method is very good to apply to the RCCI combustion because it shows good prediction to the pressure, heat release rate and emissions trends. In spite of these advantages, the calculation time is still too long because they should solve the chemistry.

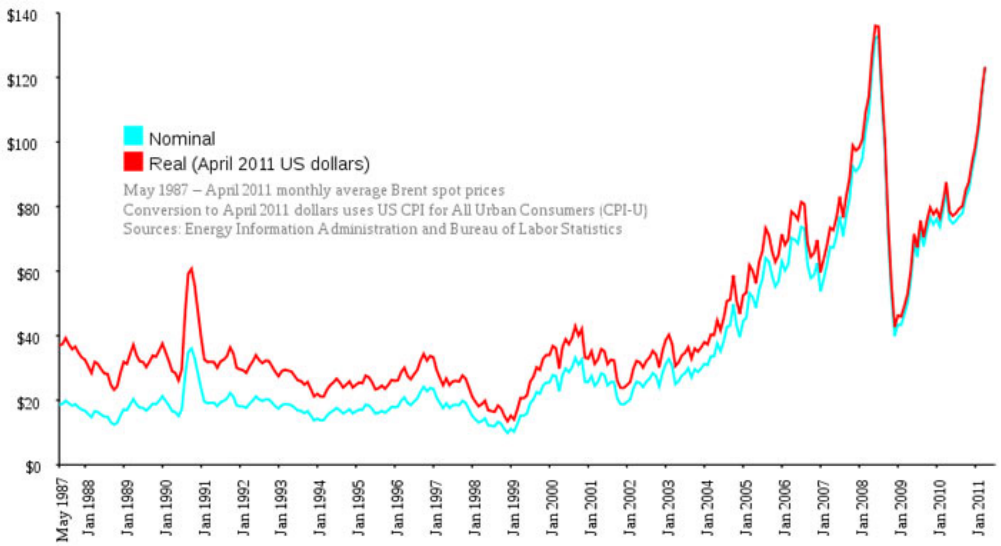

Figure 1.1.1 Monthly average Brent spot prices conversion to April 2011 dollars [40]

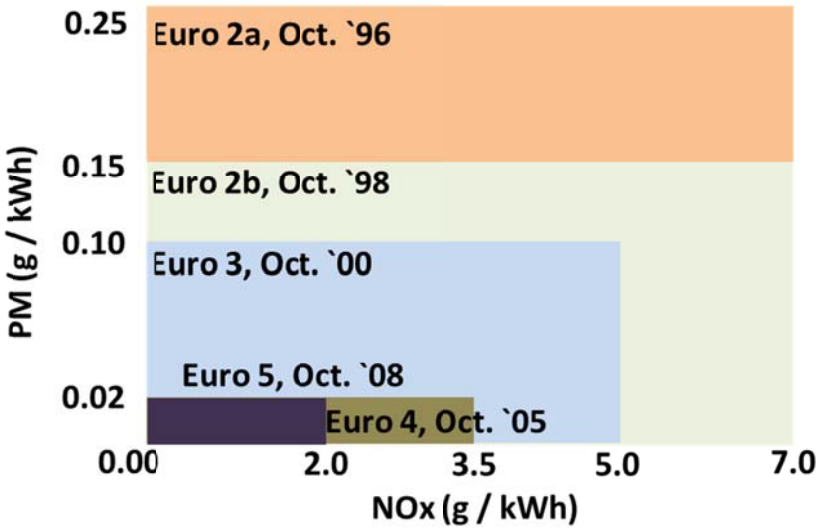

Figure 1.1.2 European emissions standards for HD Diesel engines [41].

1.2 Combustion Characteristics of Dual-Fuel Engine

The general dual-fuel combustion system features essentially a homogeneous gas-air mixture compressed rapidly below its auto-ignition conditions, and ignited by the injection of pilot liquid fuel near the top dead center (TDC) position [42]. The primary gaseous fuel controls the power output and the pilot liquid fuel contributes little fraction of power. Although the objectives and methods of the classical dual-fuel combustion are slightly different to the RCCI combustion, the basic combustion characteristics of the two combustion methods are essentially identical. RCCI combustion uses earlier injection timing than the classical dual-fuel combustion where the mixing time is enough to mix the higher reactivity fuel injected later with the lower reactivity fuel injected earlier. Hence, it shows different combustion behavior.

1.2.1 Flame structure characteristics

The procedure of classical dual-fuel combustion proceeds as follow: During the intake stroke, gaseous fuel is injected into the intake port and the air premixed with gaseous fuel is inducted into the cylinder like SI engine. Then, liquid pilot fuel is injected near the TDC. After ignition delay time of the liquid pilot fuel, multi-ignition points are generated by the non-premixed combustion from the injected liquid fuel.

A classical dual-fuel combustion procedure could be divided into three steps insisted by Carlucci *et. al*. [43]. The first step is the non-premixed combustion by the pilot injected liquid fuel. The second step is the combustion of the mixture of gaseous fuel and liquid fuel by the ignition from the non-premixed combustion at the first step. The mixture which locates vicinity of ignition points exposed to the high pressure, temperature and rich equivalence ratio conditions. Premixed

combustion is good to evolve in this environment. After these steps, at last, the premixed flame of the mixture of gaseous fuel and air which did not combust yet propagates with the turbulent flame from ignition nuclei. These procedures are shown in Figure 1.2.1 as a heat release rates according to the CAD.

The most important and distinguished point of the classical dual-fuel combustion compared to the conventional CI combustion is that premixed combustion and non-premixed combustion occurred at the one cycle simultaneously. Figure 1.2.2 shows the schematic diagram of the classical dual-fuel combustion from the top view.

On the other hands, RCCI combustion is a combustion concept based on the PCCI combustion which enables increased control of PCCI- and HCCI-like operation by tailoring the in-cylinder fuel chemistry to meet engine requirements and thus better optimize the combustion of a premixed auto-ignition regime [30]. It is the same as the dual-fuel combustion that the first ignition source is generated from the secondary injected fuel. However, the reactivity of the first injection of RCCI also has the auto-ignition features. The ignition is occurred from the mixture of the lower reactivity fuel and the higher reactivity fuel, not just from the higher reactivity fuel. From these ignition sources, the flame propagation speed is the competition between the auto-ignition and the flame propagation speed of the turbulent burning velocity of the first injected fuel. Therefore, the flame speed is faster than the flame propagation speed of SI engine but it is slower than the flame speed of HCCI combustion [44]. Figure 1.2.3 shows the characteristics of dual-fuel combustion. Eventually, higher reactivity fuel is used as an ignition trigger at all cases of dual-fuel combustion and combustion propagates to the lower reactivity fuel. The different point between the classical dual-fuel combustion and RCCI in the combustion characteristic aspect is the mixing ratio of the higher reactivity fuel and lower reactivity fuel. From this reason, the ratio of combustion stages seen in the figure 1.2.3 is being slightly different. The three stages are clearly appeared for the

classical dual-fuel combustion. Whereas the first and second stages are appeared for the RCCI combustion but the third stage, flame propagation by the lower reactivity fuel, is not appeared clearly. However, fundamental combustion characteristics of RCCI combustion are identical to the classical dual-fuel combustion.

1.2.2 Emission characteristics

In the case of conventional HSDI Diesel engine, high temperature non-premixed combustion is occurred from injected liquid fuel. From this high temperature flame region, much NOx emission is generated. In addition, soot emission is produced due to rich fuel region inside the spray pocket. In the case of conventional SI engine, high temperature combustion is occurred from the equivalence ratio of premixed fuel. The best advantage of dual fuel combustion is decreasing NOx and soot emission simultaneously without applying EGR.

Conventional dual fuel combustion uses somewhat lean gaseous fuel/air mixture (natural gas, LPG, propane, iso-octane or gasoline) and small quantity of liquid fuel (n-heptane or Diesel). Therefore, the total equivalence ratio is less than 1. Most of the researches reported that dual-fuel combustion could reduce PM emission thanks to the lean mixture [17, 18, 45]. However, in the case of NOx, emission trend is not regular. In the most researches, NOx emission produced by a dual fuel engine is smaller compared to the conventional Diesel combustion [18, 46, 47] but, on the contrary, in some researches, NOx emission is worse [45]. The reason of high NOx emission would expect from the inhomogeneous mixture fraction of gaseous fuel by high engine speed. Locally slightly rich mixture near stoichiometric mixture fraction would produce high combustion temperature and then it makes higher NOx emission. In the case of RCCI combustion, NOx emission is decreased at the wide operating conditions. At low load, slightly lower NOx emission is produced compared to the conventional Diesel combustion because of lower rate of premixed controlled combustion of gaseous fuel and lower charge

temperature inside the combustion chamber. Contrary to the low load, NOx emission at high load condition is considerably lower than that from conventional Diesel combustion [48].

In the case of CO and THC, dual-fuel combustion is much higher than conventional Diesel combustion. Although premixed gaseous fuel makes lean mixture, this lean mixture is not burned completely because the burning velocity is slower than stoichiometric condition. Lower combustion temperature due to this lean mixture is also an important factor of high CO and THC emissions. If lean mixture is not burned until the end of expansion stroke, these emissions come out at the tail-pipe. This phenomenon could also be occurred in RCCI combustion.

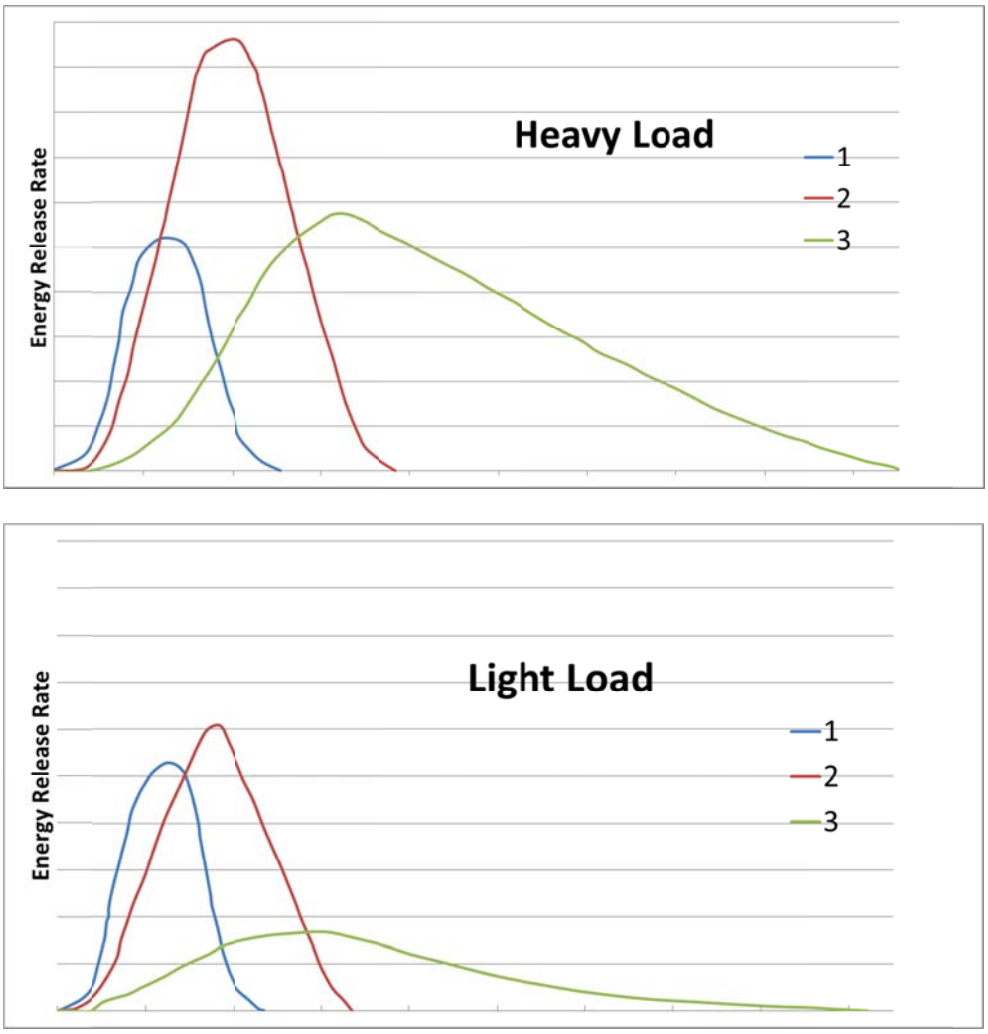

Figure 2.2.1 Schematic representation of the contribution of the various parts of the combustion process to the effective energy release rate under heavy and light load condition in a typical dual fuel engine [49]

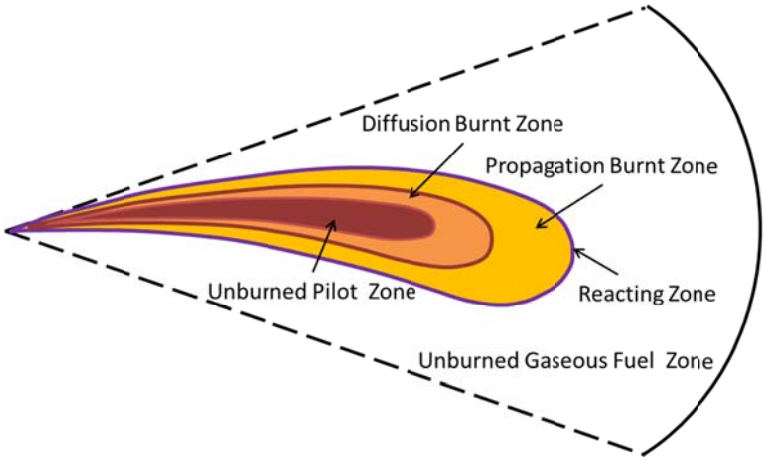

Figure 1.2.2 Schematic zone divisions during the classical dual-fuel combustion [15]

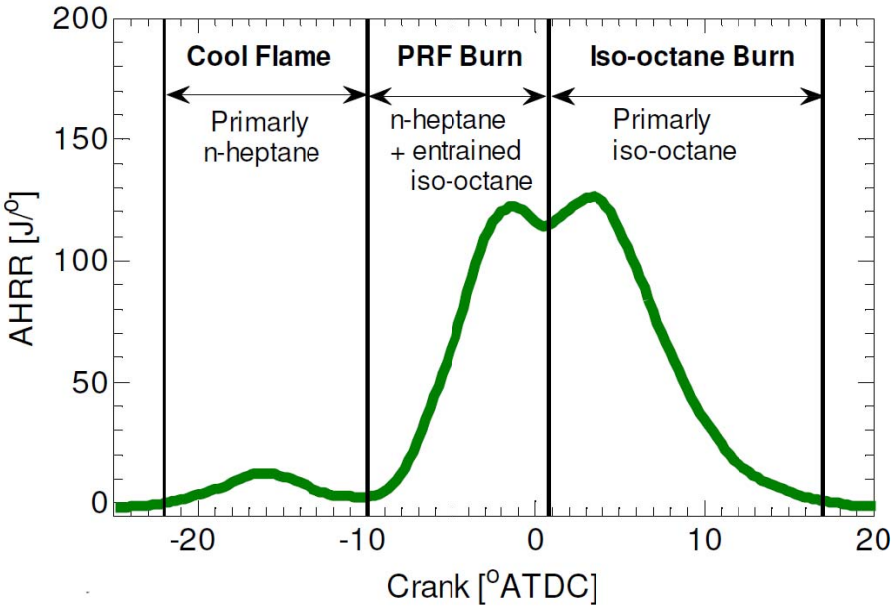

Figure 1.2.3 Heat release rate of dual-fuel combustion (3 stages) cool flame, first energy release from mixed fuels and final energy release from lower reactivity fuel [50].

1.3 Objectives

Dual-fuel combustion engine has its own distinguishing combustion and emission characteristics different from SI engine or CI engine. In this study, the combustion process and pollutant formation of a classical dual-fuel engine and RCCI engine were simulated by one numerical model based on the premixed flame propagation model and non-premixed flame model. The objectives of the modeling are:

1. Modeling of turbulent flame propagation to describe the location of flame front in partially premixed situation with consideration on the laminar flame speed-mixture stoichiometry relationship and spatial fluctuation of local equivalence ratio,

2. Coupling turbulent flame propagation to the ignition model to describe the procedure of dual-fuel combustion

3. Modeling of chemical state change from unburned to burnt with implementing reduced chemical reaction mechanism of iso-octane and propane, and

4. Modeling of pollutant formation which includes sub-models for, NOx formation and particularly soot formation in partially premixed condition of a dual-fuel engine.

Chapter 2. Combustion and Emission Models Review

Turbulent combustion is subdivided into two classes: premixed and non-premixed combustion [51]. In the SI engine, fuel and oxidizer could be mixed down to the molecular level during the intake stroke and compression stroke. The flame kernel generated from the spark grows at first by laminar flame speed, but it turns to the turbulent burning velocity soon. Therefore, turbulent burning velocity is an important parameter in the SI engine. In the CI engine, on the other hands, fuel is injected into the high pressure, high temperature air in the engine cylinder. Injected fuel is auto-ignited after some physical and chemical ignition delay time of the fuel. Inside of the fuel spray is very rich region and outside of the fuel spray is very lean region or pure air region. Ignition is occurred at the stoichiometric region between two regions. Therefore, the combustion occurs under non-premixed conditions.

2.1 Classical Turbulence Models with Combustion

2.1.1 Moment Methods

In CI engine, GDI engine and dual fuel engine simulation, two-phase fluid flows should be described by the governing equations due to liquid fuel injection. The equation for the gas phase density ρ is [52]

$$\frac{\partial \rho}{\partial t} + \frac{\partial (\rho v_\alpha)}{\partial x_\alpha} = \rho \dot{S} \tag{2.1.1}$$

where $\dot{S}$ is a source or sink term due to the presence of the liquid phase. The rate of change of gas phase momentum in each direction α is

$$\frac{\partial(\rho v_\alpha)}{\partial t} + \frac{\partial(\rho v_\alpha v_\beta)}{\partial x_\alpha} = -\frac{\partial p}{\partial t} + \frac{\partial \tau_{\alpha\beta}}{\partial x_\alpha} + f_\alpha^s \tag{2.1.2}$$

where f_α^s is the rate of momentum gain per unit volume due to its interaction with the second phase. $\tau_{\alpha\beta}$ is the symmetric stress tensor. In CFD analysis, Newtonian fluid is assumed as

$$\tau_{\alpha\beta} = \mu\left(\frac{\partial v_\alpha}{\partial x_\beta} + \frac{\partial v_\beta}{\partial x_\alpha}\right) + \delta_{\alpha\beta}\lambda\frac{\partial v_\gamma}{\partial x_\gamma}, \;\; \lambda = -\frac{2}{3}\mu \tag{2.1.3}$$

where μ is the dynamic viscosity and $\delta_{\alpha\beta}$ is the Kronecker delta. Although equations (2.1.1) and (2.1.2) could be an appropriate initial and boundary conditions to describe the flow field, the flow conditions in in-cylinder engine is turbulent. Since various sizes of scales exist in this turbulence, equations (2.1.1) and (2.1.2) should be solved in the smallest time and length scale. It is called as direct numerical simulation (DNS) but it is impossible to solve these equations at the case of engine simulations which have complicated engine geometry and high Reynolds number in the smallest mesh size and time step practically due to the computational power. Therefore, we need the other solutions to solve these equations and the simplest method is modeling the small motion. Although modeling the small motion could abandon the minor information occurred in a small motion, it saves the computational calculation time without loss of important information. The general reduction method is an averaging the original equations.

Turbulence consists of random velocity fluctuations so that it must be treated with statistical methods [53]. To describe the turbulent flow, a simple decomposition of all velocity and scalar quantities such as temperature and mass fractions measured at a location $\vec{x}$ into a mean value (overbar) and a fluctuation with zero mean, for example, u

$$u(\vec{x}, t) = \bar{u}(\vec{x}, t) + u'(\vec{x}, t), \text{ where } \bar{u}'(\vec{x}, t) = 0 \tag{2.1.4}$$

For the case of large density changes flow like combustion, introducing Favre average, a density weighted average $\tilde{u}$ rather than $\bar{u}$ is good to be applied.

$$\mathrm{u}(\vec{x},t) = \tilde{u}(\vec{x},t) + u''(\vec{x},t), \text{ where } \overline{\rho u''}(\vec{x},t) = 0 \qquad (2.1.5)$$

2.1.2 Turbulence models

The averaging could be applied to the governing equations instead of a single quantity. The ensemble averaging procedure yields the Reynolds Averaged Navier-Stokes (RANS) equations. RANS equations describe only the motion of integral scales. In this research, RANS method is used to describe the in-cylinder turbulent flow.

The balance equations could be transformed using Favre average like below

Continuity

$$\frac{\partial \bar{\rho}}{\partial t} + \frac{\partial (\bar{\rho}\widetilde{v_\alpha})}{\partial x_\alpha} = 0 \qquad (2.1.6)$$

Momentum

$$\bar{\rho}\frac{\partial \widetilde{v_\beta}}{\partial t} + \bar{\rho}\widetilde{v_\alpha}\frac{\partial \widetilde{v_\beta}}{\partial x_\alpha} = -\frac{\partial \bar{p}}{\partial x_\beta} + \frac{\partial \overline{\tau_{\alpha\beta}}}{\partial x_\alpha} - \frac{\partial}{\partial x_\alpha}\left(\bar{\rho}\widetilde{v''_\alpha v''_\beta}\right) + \bar{\rho}g_\beta, \ \ \beta = 1,2,3 \qquad (2.1.7)$$

In equation (2.1.7), l.h.s represents the local rate of change and convection. r.h.s of equation (2.1.7) shows the pressure gradient, molecular transport due to viscosity, turbulent transport and forces due to buoyancy, respectively.

Among these terms, Reynolds stress tensor $\bar{\rho}\widetilde{v''_\alpha v''_\beta}$ is not easy to solve generally because it is an unclosed term. This is so-called second moment closure or Reynolds stress equation modeling and it represents the classical closure

problem of turbulent flow models. Therefore, some closure assumption have been proposed to solve this term [54]. To solve this turbulent transport term, Boussinesq proposed the concept of the eddy viscosity, ν_t, using a gradient transport hypothesis [55]

$$\bar{\rho}\widetilde{v''_\alpha v''_\beta} = -\bar{\rho}\widetilde{\nu_t}\left[2\frac{\partial\widetilde{v_\alpha}}{\partial x_\beta} - \frac{2}{3}\frac{\partial\widetilde{v_\gamma}}{\partial x_\gamma}\right] + \frac{2}{3}\bar{\rho}\tilde{k}\,, \alpha = \beta \tag{2.1.8}$$

$$= -\bar{\rho}\widetilde{\nu_t}\left[\frac{\partial\widetilde{v_\alpha}}{\partial x_\beta} + \frac{\partial\widetilde{v_\beta}}{\partial x_\alpha}\right], \alpha \neq \beta$$

Among several developed eddy viscosity models, two-equation standard $k-\varepsilon$ model is the most popular model [56]. Turbulent length scale, l, time scale, τ, and turbulent viscosity, $\widetilde{\nu_t}$, could be described by turbulent kinetic energy, $\tilde{k}$, and turbulent dissipation rate, $\tilde{\varepsilon}$, like below:

$$l = \frac{\tilde{k}^{3/2}}{\tilde{\varepsilon}},\ \tau = \frac{\tilde{k}}{\tilde{\varepsilon}},\ \widetilde{\nu_t} = c_\mu\frac{\tilde{k}^2}{\tilde{\varepsilon}},\ c_\mu = 0.09 \tag{2.1.9}$$

In the standard $k-\varepsilon$ model, the equation for the turbulent kinetic energy is

$$\frac{\partial\bar{\rho}\tilde{k}}{\partial t} + \frac{\partial}{\partial x_\alpha}\left[\bar{\rho}\widetilde{v_\alpha}\tilde{k} - \left(\mu + \frac{\mu_t}{\sigma_\gamma}\right)\frac{\partial\tilde{k}}{\partial x_\alpha}\right] = \mu_t\left(S_{\alpha\beta}\frac{\partial\widetilde{v_\alpha}}{\partial x_\beta} - \frac{\overline{g_\alpha}}{\sigma_{h,t}}\frac{1}{\bar{\rho}}\frac{\partial\bar{\rho}}{\partial x_\alpha}\right) - \bar{\rho}\tilde{\varepsilon} -$$

$$\frac{2}{3}\left(\frac{\partial\widetilde{v_\beta}}{\partial x_\beta} + \rho\tilde{k}\right)\frac{\partial\widetilde{v_\beta}}{\partial x_\beta} \tag{2.1.10}$$

The equation for the turbulent energy dissipation rate is

$$\frac{\partial\bar{\rho}\tilde{\varepsilon}}{\partial t} + \frac{\partial}{\partial x_\alpha}\left[\bar{\rho}\widetilde{v_\alpha}\tilde{\varepsilon} - \left(\mu + \frac{\mu_t}{\sigma_\gamma}\right)\frac{\partial\tilde{\varepsilon}}{\partial x_\alpha}\right] = C_{\varepsilon1}\frac{\tilde{\varepsilon}}{\tilde{k}}\left[\mu_t P - \frac{2}{3}\left(\mu_t\frac{\partial\widetilde{v_\beta}}{\partial x_\beta} + \bar{\rho}\tilde{k}\right)\frac{\partial\widetilde{v_\beta}}{\partial x_\beta}\right] +$$

$$C_{\varepsilon2}\frac{\tilde{\varepsilon}}{\tilde{k}}\mu_t P_B - C_{\varepsilon3}\bar{\rho}\frac{\widetilde{\varepsilon^2}}{\tilde{k}} + C_{\varepsilon4}\bar{\rho}\frac{\partial\widetilde{v_\beta}}{\partial x_\beta} \tag{2.1.11}$$

where σ_γ is the turbulent Prandtl number and $C_{\varepsilon 1}, C_{\varepsilon 2}, C_{\varepsilon 3}$ and $C_{\varepsilon 4}$ are coefficients listed in Table 2.1.1.

In this study, RNG (ReNormalization Group) $k-\varepsilon$ model, modified formation of the standard $k-\varepsilon$ model was used to model the turbulent flow in a dual fuel engine [57]. Many previous studies applied the RNG $k-\varepsilon$ model and obtained good results [58-60]. In this model, the equation for the turbulent kinetic energy was not changed but the equation for the turbulent dissipation rate was changed like

$$\frac{\partial \bar{\rho}\tilde{\varepsilon}}{\partial t}+\frac{\partial}{\partial x_\alpha}\left[\bar{\rho}\widetilde{v_\alpha}\tilde{\varepsilon}-\left(\mu+\frac{\mu_t}{\sigma_\gamma}\right)\frac{\partial \tilde{\varepsilon}}{\partial x_\alpha}\right]=C_{\varepsilon 1}\frac{\tilde{\varepsilon}}{\tilde{k}}\left[\mu_t P-\frac{2}{3}\left(\mu_t\frac{\partial \widetilde{v_\beta}}{\partial x_\beta}+\bar{\rho}\tilde{k}\right)\frac{\partial \widetilde{v_\beta}}{\partial x_\beta}\right]+$$

$$C_{\varepsilon 2}\frac{\tilde{\varepsilon}}{\tilde{k}}\mu_t P_B-C_{\varepsilon 3}\bar{\rho}\frac{\widetilde{\varepsilon^2}}{\tilde{k}}+C_{\varepsilon 4}\bar{\rho}\frac{\partial \widetilde{v_\beta}}{\partial x_\beta}-\frac{C_\mu\eta^3(1-\eta/\eta_0)\bar{\rho}}{1+\phi\eta^3}\frac{\widetilde{\varepsilon^2}}{\tilde{k}} \quad (2.1.12)$$

where $\eta=S\frac{\tilde{k}}{\tilde{\varepsilon}}$ and η_0, ϕ are empirical coefficients listed in Table 2.1.2.

Table 2.1.1 Coefficients of the Standard $k-\varepsilon$ Turbulence Model

C_μ	σ_k	σ_ε	σ_h	$C_{\varepsilon 1}$	$C_{\varepsilon 2}$	$C_{\varepsilon 3}$	$C_{\varepsilon 4}$
0.09	1.0	1.22	0.9	1.44	1.92	0.0 or 1.44*	-0.33

Table 2.1.2 Coefficients of the RNG $k-\varepsilon$ Turbulence Model

C_μ	σ_k	σ_ε	σ_h	$C_{\varepsilon 1}$	$C_{\varepsilon 2}$	$C_{\varepsilon 3}$	$C_{\varepsilon 4}$	η_0	β
0.085	0.719	0.719	0.9	1.42	1.68	0.0 or 1.42*	-0.33	4.38	0.012

2.2 Models for the Non-premixed Combustion

2.2.1 Basics in premixed turbulent combustion

2.2.1.1 The mixture fraction variable

The mixture fraction is an extremely useful variable in combustion, in particular for diffusion flames [51]. Fig 2.2.1 shows a two-feed system where a fuel stream with mass flux, $\dot{m}_1$, is mixed with an oxidizer stream with mass flux, $\dot{m}_2$. Then, the mixture fraction could be defined as

$$Z = \frac{\dot{m}_1}{\dot{m}_1 + \dot{m}_2} \tag{2.2.1}$$

With the mixture fraction, the mass fraction of the fuel in the mixture is proportional to the mass fraction in the fuel stream as

$$Y_{F,u} = Y_{F,1} Z \tag{2.2.2}$$

where $Y_{F,1}$ is the mass fraction of fuel in the fuel stream. As the same way, mass fraction of oxygen in the mixture could be represented as

$$Y_{O2,u} = Y_{O2,2}(1 - Z) \tag{2.2.3}$$

where $Y_{O2,2}$ is the mass fraction of oxygen in the oxidizer stream. If no EGR is applied, $Y_{O2,2}$ would be 0.232.

From the mixture fraction, Z, we could fix the location of the thin reaction zone as

$$Z(\vec{x}, t) = Z_{st} \tag{2.2.4}$$

A general definition for the mixture fraction was proposed by Peters using a simple convection-diffusion equation [51] as

$$\rho \frac{\partial Z}{\partial t} + \rho \vec{v} \cdot \nabla Z = \nabla \cdot (\rho D \nabla Z) \tag{2.2.5}$$

where D means the diffusion coefficient. In principle, D would be arbitrary but it is convenient to set it equal to thermal diffusivity because $D = \lambda / \rho c_P = D_T$ (λ is the thermal conductivity). Equation (2.2.5) has no source term because Z is a conserved scalar. Z is not generated or consumed by chemical reactions.

Due to the injected fuel, we assume the mixture fraction, Z, to be given in the flow field as a function of space and time as the solution of equation (2.2.5). Also, the surface of the stoichiometric mixture could be determined from equation (2.2.4). The surface of stoichiometric mixture is highly convoluted by the turbulent flow. In turbulent combustion, we need the averaged solution. Therefore, we transformed equation (2.2.5) as Favre averaged form mentioned in Chapter 2.1.

$$\bar{\rho} \frac{\partial \tilde{Z}}{\partial t} + \bar{\rho} \vec{v} \cdot \nabla \tilde{Z} = \nabla \cdot (\bar{\rho} D_t \nabla \tilde{Z}) \tag{2.2.6}$$

In addition to the mean mixture fraction, the mixture fraction variance should be solved. The balance equation for the mixture fraction variance is modeled by standard procedures as

$$\bar{\rho} \frac{\partial \widetilde{Z''^2}}{\partial t} + \bar{\rho} \vec{v} \cdot \nabla \widetilde{Z''^2} = \nabla \cdot \left(\bar{\rho} D_t \nabla \widetilde{Z''^2} \right) + 2 \bar{\rho} D_t \left(\nabla \widetilde{Z''^2} \right)^2 - \bar{\rho} \tilde{\chi} \tag{2.2.7}$$

where $\tilde{\chi}$ is the mean scalar dissipation rate and is defined as

$$\tilde{\chi} = 2D (\nabla \widetilde{Z''})^2 \tag{2.2.8}$$

This mean scalar dissipation rate was modeled typically as [61]

$$\tilde{\chi} = c_x \frac{\tilde{\varepsilon}}{\tilde{k}} \widetilde{Z''^2} \tag{2.2.9}$$

where the time scale ratio, c_x, is assumed to be a constant and a value of 2.0 is typical for internal combustion engines [62].

2.2.1.2 The mixture fraction variable

In non-premixed combustion, characteristic length scale or velocity scale are not important. Instead, strain rate, a, generated by flow field locally is an important variable which means the inverse of a characteristic time. Strain rate and diffusion coefficient, D_{st}, could describe the diffusion thickness as follow:

$$l_D = \left(\frac{D_{st}}{a}\right)^{1/2} \tag{2.2.10}$$

Diffusion thickness, l_D, is also defined using gradient of mixture fraction field $|\nabla Z|_{st}$. Diffusion thickness in the mixture fraction space, $(\Delta Z)_F$, could be defined using diffusion thickness in the physical space, l_D, as

$$(\Delta Z)_F = |\nabla Z|_{st}\, l_D \tag{2.2.11}$$

This diffusion thickness in the mixture fraction space covers the reaction zone and the surrounding diffusion layers as [63]

$$(\Delta Z)_F = 2Z_{st} \tag{2.2.12}$$

We could define another length scale, reaction zone thickness $(\Delta Z)_R$ in the mixture fraction domain, because the fuel consumption layer is much smaller than the oxidation layer. These two thicknesses have the relationship as [64]

$$\frac{(\Delta Z)_R}{(\Delta Z)_F} = \varepsilon_q \left(\frac{\chi_{st}}{\chi_q}\right)^{1/4} \tag{2.2.13}$$

where st means stoichiometry and χ_{st} is the conditional Favre mean scalar dissipation rate. In a turbulent diffusion combustion, the characteristic thickness $(\Delta Z)_R$ and $(\Delta Z)_F$ should be compared with mixture fraction variances defined by the r.m.s of the variance at mean stoichiometric mixture as

$$Z'_{st} = \left(\widetilde{Z''^2}\right)_{st}^{1/2} \tag{2.2.14}$$

Figure 2.2.1 shows the regime diagram for non-premixed turbulent combustion that x-axis means time scale ratio χ_q/χ_{st} and y-axis is the ratio of $Z'_{st}/(\Delta Z)_F$. If the mixture fraction fluctuations are larger than $(\Delta Z)_F$, flamelet is separated. In addition to this threshold, another criterion exists; $Z'_{st}/(\Delta Z)_R$=1. Below this line, the mixture fraction fluctuations are smaller than the reaction zone thickness $(\Delta Z)_R$, and even the reaction zones are connected. It means homogenous mixture fraction field. The last criterion is extinction threshold. If $\chi_q < \widetilde{\chi_{st}}$, flamelet is extinguished.

The shape of a diffusion flame in Figure 2.2.2 shows how local conditions along the contour of mean stoichiometric mixture in a jet diffusion flame would fit into the different regimes of non-premixed turbulent combustion. Since Z'_{st} decreases as $1/x$ and $\widetilde{\chi_{st}}$ approximately as $1/x^2$ along the surface of mean stoichiometric mixture in a turbulent jet flame, the dash-dotted line corresponds to a line with a slope -1/2 [65].

2.2.2 Laminar Flamelet Model

The reactive-diffusive structure of the flamelet is determined by the equation for the mass fraction, Y_i, as [66]

$$\rho\frac{\partial Y_i}{\partial t} + \rho\vec{v}\cdot\nabla Y_i = \frac{1}{Le_i}\nabla\cdot(\rho D\nabla Y_i) + \dot{m}_\iota \quad (i = 1,2,\dots,n) \tag{2.2.15}$$

and the temperature could be expressed as [66]

$$\rho c_p \frac{\partial T}{\partial t} + \rho c_p \vec{v} \cdot \nabla T = \nabla \cdot \left(\rho c_p D_T \nabla Y_i\right) - \sum_{i=1}^{n} h_i m_i + q_R + \frac{\partial p}{\partial t} \quad (2.2.16)$$

In the above equations, $\dot{m}_\iota$ and h_i means the chemical source term and enthalpy of species *i*, respectively, and $\sum_{i=1}^{n} h_i m_i$ means the heat release rate. Y_i means the species mass fraction and p is the pressure, Lewis numbers for all species are assumed

$$Le_i = \frac{\lambda}{\rho c_p D_i} = \frac{D_T}{D_i} \quad (2.2.17)$$

to be constant. In the low Mach number region, $\partial p/\partial t$ could be zero, but the temporal pressure change $\partial p/\partial t$ has been retained.

Peters introduced the concept of a laminar diffusion flamelet residing in the vicinity of the surface where a sufficiently high local mixture gradient exists [67]. A coordinate was introduced that is attached to the surface of the stoichiometric mixture and deduced the following unsteady 2nd order partial differential equations from the equations (2.2.15) and (2.2.16):

$$\rho \frac{\partial Y_i}{\partial t} = \frac{\rho \chi}{2} \frac{\partial^2 Y_i}{\partial Z^2} + \dot{m}_\iota \quad (2.2.18)$$

$$\rho \frac{\partial T}{\partial t} = \frac{\rho \chi}{2} \left(\frac{\partial^2 T}{\partial Z^2} + \frac{1}{c_p} \frac{\partial c_p}{\partial Z} \frac{\partial T}{\partial Z} - \frac{\partial T}{\partial Z} \sum \frac{c_{p,k}}{c_p} \frac{\partial Y_k}{\partial Z}\right) - \frac{1}{c_p} \left(\sum h_k \dot{m}_k - \frac{\partial p}{\partial t}\right) \quad (2.2.19)$$

In the above equations, χ is the scalar dissipation rate and interpreted as the inverse of the characteristics diffusion time. This factor represents the influence of the turbulent flow field on the laminar flamelet. It is defined as

$$\chi = 2D_Z \sum \left(\frac{\partial Z}{\partial x_i}\right)^2 \quad (2.2.20)$$

However, this quantity is difficult to extract from a calculation of a turbulent flow since it requires the instantaneous value of Z. In addition, it is important that the gradual homogenization of the mixture is reflected in the scalar dissipation rate [68]. As the scalar dissipation rate increases, the heat transfer from the reaction zone to the surrounded inertia increases which causes an increase in the ignition delay time. The χ profile with respect to the mixture fraction, Z, in the configuration of counter-flow geometry could be modeled by Peters [65] as

$$\chi = 4a_s Z^2 [erfc^{-1}(2Z)]^2 = 4a_s f(Z) \quad (2.2.21)$$

The turbulent diffusion flame can be considered as an ensemble of laminar diffusion flamelets. Therefore, it could be averaged by the probability density function (PDF).

2.2.3 Turbulent Averaging Laminar Flamelet Equations

In this research, the combustion phenomena with liquid fuel droplets injected were considered. The transport equations for the Favre averaged mixture fraction and the variance are documented as

$$\bar{\rho}\frac{\partial \widetilde{Z}_\iota}{\partial t} + \bar{\rho}\widetilde{v_f} \cdot \nabla \widetilde{Z}_\iota = \nabla \cdot \left(\bar{\rho} D_T \nabla \widetilde{Z}_\iota\right) + \dot{S}_\iota \quad (2.2.22)$$

$$\bar{\rho}\frac{\partial \widetilde{Z''_\iota{}^2}}{\partial t} + \bar{\rho}\widetilde{v_f} \cdot \nabla \widetilde{Z''_\iota{}^2} = \nabla \cdot \left(\bar{\rho} D_T \nabla \widetilde{Z''_\iota{}^2}\right) + 2\bar{\rho} D_T \left(\nabla \widetilde{Z}_\iota\right) - \bar{\rho}\widetilde{\chi}_\iota \quad (2.2.23)$$

where $\widetilde{\chi}_\iota$ is the mean scalar dissipation rate of the mixture *i*, which can be obtained by using the following equation

$$\widetilde{\chi_\iota} = 2D_i \sum \left(\frac{\partial \widetilde{Z_\iota}}{\partial x_i}\right)^2 \tag{2.2.24}$$

and the source term $\dot{S}_\iota$ is equal to the vaporization rate of the liquid droplets.

For one –dimensional flamelet equations, equation (2.2.21) should be scaled by the turbulent properties of the combustion field. The erfc-profile function was defined as

$$f(Z) = Z^2[erfc^{-1}(2Z)]^2 \tag{2.2.25}$$

The scalar dissipation rate of any mixture fraction can be scaled using the value at stoichiometric mixture fraction as

$$\chi(Z) = \chi(Z_{st})\frac{f(Z)}{f(Z_{st})} \tag{2.2.26}$$

Using equation (2.2.26), a local value for the scalar dissipation rate conditioned on stoichiometric mixture, $\chi_{st,l}$, is computed as [69]

$$\chi_{st,l} = \frac{\widetilde{\chi} f(Z_{st})}{\int_0^1 f(Z)P(\tilde{Z})dZ} \tag{2.2.27}$$

where $P(\tilde{Z})$ is the probability density function.

There are many methods to obtain the required mixture fraction PDF. In this research, presumed $\beta - PDF$ was used. It has shown to be a good approximation of jet-diffusion flames [54].

$$P(\tilde{Z}) = \frac{\Gamma(\beta_1+\beta_2)}{\Gamma(\beta_1)\Gamma(\beta_2)} Z^{\beta_1-1} Z^{\beta_2-1} \tag{2.2.28}$$

where Γ-function is defined as

$$\Gamma(\beta) = \int_0^\infty x^{\beta-1} e^{-x} dx \tag{2.2.29}$$

The parameters β_1 and β_2 could be calculated from the mean and the variance of the mixture fraction by

$$\beta_1 = \tilde{Z}\left[\frac{\tilde{Z}(1-\tilde{Z})}{\widetilde{Z''^2}} - 1\right] \tag{2.2.30}$$

$$\beta_2 = (1-\tilde{Z})\left[\frac{\tilde{Z}(1-\tilde{Z})}{\widetilde{Z''^2}} - 1\right] \tag{2.2.30}$$

Averaging these local values on the surface of stoichiometric mixture yields the domain averaged scalar dissipation rate conditioned on stoichiometric mixture as [70]

$$\widehat{\chi_{st}} = \frac{\int_V \chi_{st,l}^{3/2} \bar{\rho} P(Z_{st}) dV'}{\int_V \chi_{st,l}^{1/2} \bar{\rho} P(Z_{st}) dV'} \tag{2.2.31}$$

where V' is the domain of averaging.

The turbulent mean species were obtained by integrating the flamelet solutions with a probability density function in each CFD cell.

$$\widetilde{Y_i} = \int_0^1 P(Z; x_\alpha, t) Y_i(Z,t) dZ \tag{2.2.32}$$

where $Y_i(Z,t)$ is the solutions of laminar flamelet equations (2.2.18) and (2.2.19).

2.2.4 Coupling Flamelet Equations with CFD Code

In this study, commercial CFD code, STAR-CD was used. The representative interactive flamelet model does not require empirical parameters and could separate turbulent time scale and chemical time scale numerically. Therefore, time step of CFD code does not need to be divided as small as chemical time scale. The

following procedure could be used to analyze the combustion phenomena with a detailed chemical kinetic mechanism using STAR-CD.

1. At each time step, the CFD code calculates the transport equations of the mixture fraction, mixture fraction variance, boundary conditions and the scalar dissipation rate of the combustion field at each time step.

2. Based in the scalar dissipation rate and boundary conditions, the flamelet code calculates the species and temperature distributions in the mixture fraction coordinate. This calculation is performed with a much shorter time step than that of the CFD code. The results are delivered to the CFD code in the Favre averaged form for the turbulent flow. Using these results, the CFD code calculates the temperature of each cell.

3. The CHEMKIN library [64] delivers the enthalpy of each cell to the CFD code, and the reaction rate to the flamelet code.

Figure 2.2.3 shows the relationship among the CFD code, flamelet code and CHEMIN library. With this procedure, many researches have been studied successfully [14, 71].

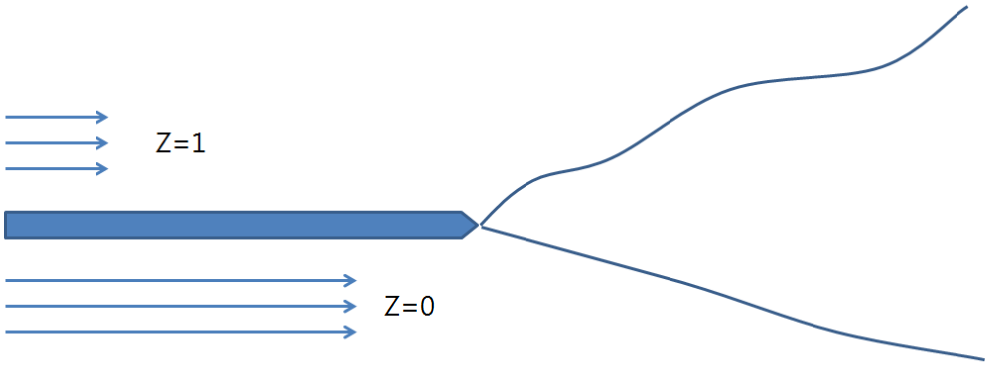

Figure 2.2.1 Mixing behind a splitter plate for a two-feed system [51]

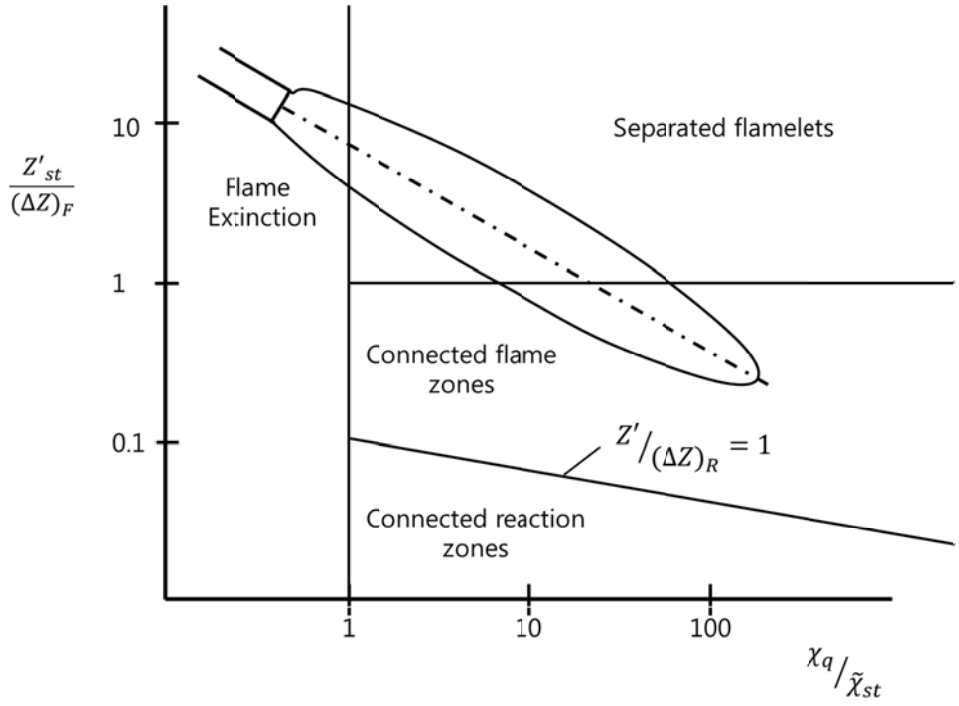

Figure 2.2.2 Regimes in non-premixed turbulent combustion [63]

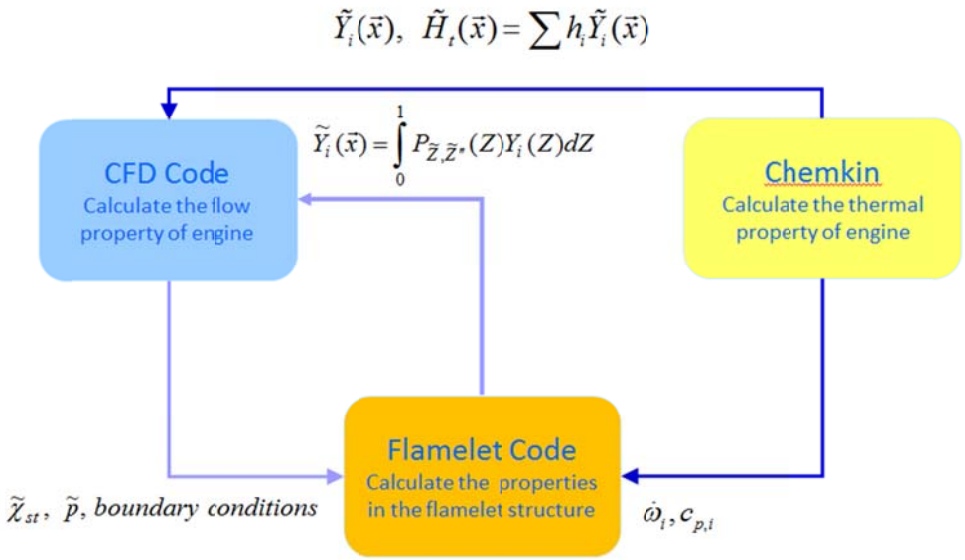

Figure 2.2.3 Schematic of coupling method

2.3 Modeling of Turbulent Flame Propagation

2.3.1 Basics in premixed turbulent combustion

In premixed flame, turbulent length scales and combustion regimes are very important and must be discussed. There are many turbulent length scales such as integral length scale, inertial length scale, Gibson length scale and Kolmogorov length scale. Among these length scales, integral length scale which is the largest length scale and Kolmogorov length scale which is the smallest length scale are the most important length scales.

The integral length scale, l, represent the mean size of the large eddies that contains most of the turbulent kinetic energy. Integral length scale is highly anisotropic and is defined in terms of the normalized two-point velocity correlations. The Kolmogorov length scale, η, corresponds to the size of the smallest eddies in a turbulent flow. The small scales are in high frequency and this is why turbulence is locally isotropic and homogeneous. At this smallest length scale, viscous forces are dominant and the turbulent kinetic energy is dissipated into the fluid's internal energy. From the dimensional analysis, η could be determined with the kinematic viscosity, ν, and kinetic energy dissipation rate, ε, as

$$\eta = \frac{\nu^3}{\varepsilon} \tag{2.3.1}$$

Before concentrating on the turbulent premixed combustion, laminar premixed flame should be reviewed. The premixed flame structure is divided into 3 regions as a preheat zone, an inner layer and an oxidation layer as shown in Figure 2.3.1. Unburned gas is preheated in the preheat zone where little heat is released. Behind the preheat zone is the inner layer whose thickness is of the order δ times thinner than the preheat zone. The fuel is consumed and the chemical reactions mainly

occur in this layer. If the turbulent eddies penetrate into the inner layer, turbulent mixing enhances the heat conduction and radical diffusion and if the enhanced transport of heat and radicals out of the layer exceed their production, the flame will be extinguished. The inner layer characteristic temperature, T^0, relates to the crossover temperature between chain-branching and chain breaking chemical reaction steps [66]. Behind the inner layer is the oxidation layer where CO and H_2 are oxidized to form CO_2 and H_2O. When turbulent eddies penetrate into this layer, these oxidation reactions are influenced. However, feedback from the downstream oxidation layer to the inner layer is very weak [66]. Therefore, turbulence effects within the oxidation layer on the inner layer can be ignored.

The most important length scale in laminar premixed flame is the characteristic flame thickness, l_F, which is defined as

$$l_F = (\lambda/c_p)_0/(\rho S_L^0)_u \tag{2.3.2}$$

where λ is the heat conductivity, c_p is heat capacity and 0 means these values are evaluated at the inner layer with inner layer temperature T^0. Density ρ and laminar burning velocity S_L^0 are the values of unburned gas. This scale is an approximation of the size of the preheat zone. From the previous research, the inner layer length scale is related to the flame thickness, l_F, by $l_\delta = l_F\delta$, where δ=0.1 approximately for stoichiometric, laminar premixed methane flames at ambient pressure [63].

From the turbulent length scales and characteristics flame thickness of laminar premixed flame, turbulent premixed combustion could be classified into 4 regimes. These are wrinkled flamelet, corrugated flamelet, thin reactions zones and broken reaction zones as shown in Figure 2.3.2 [51]. In this figure, y-axis, v'/S_L, means the turbulent intensity and x-axis, l/l_F, means the sizes of eddies. In addition, there are two different Karlovitz numbers, $Ka = l_F^2/\eta^2$ and $Ka_\delta = l_\delta^2/\eta^2$ and these means the ratio of the flame thickness to the Kolmogorov scale and the ratio of the

thickness of the inner layer to the Kolmogorov scale, respectively. The combustion regime of SI engines is usually included in wrinkled flamelet, corrugated flamelet and thin reaction zone regimes [72].

In the wrinkled flamelet and corrugated flamelet regimes, the Kolmogorov length scales are larger than the flame thickness. In the wrinkled flamelet regime, the turnover velocity of eddies is smaller than the laminar burning velocity. It means the flame front cannot be wrinkled by eddies. The flame front corrugation due to turbulent eddies are demolished by the flame propagation in this wrinkled flamelet regime. In the corrugated flamelet regime, the turnover velocity of eddies is larger than laminar burning velocity and it makes flame front corrugated. Furthermore, turbulent eddies of all sizes could not perturb the chemical and transport processes within the flame thickness in these two regimes.

In the thin reaction zone regime, the Kolmogorov eddies penetrate through the preheat zone and they increase the mixing of chemical species and heat transfer rates. However, eddies could not penetrate into the inner layer. Therefore, chemical reactions in the inner layer are not affected. If the Kolmogorov scale eddies enter into the inner layer in the broken reaction zone regime, the chemical reaction rates in the inner layer decrease due to heat and radical species losses. Then, the flame would become extinguished locally.

2.3.2 Flamelet model for laminar premixed combustion

For the premixed combustion, flamelet models are either based on the progress variable, c, or on the scalar G. The flame area evolution (FAE) model developed by Weller *et al.* uses progress variable, c, to simulate the turbulent flame propagation in SI engine [73]. In this method, progress variable, c, is defined as a normalized temperature or normalized product mass fraction,

$$c = \frac{T - T_u}{T_b - T_u}, \tag{2.3.3}$$

the flame structure is assumed to be infinitely thin and no intermediate values of temperature between T_u and T_b are solved. Progress variable is just a step function that separates unburned mixture and burned gas in a given flow field. Although this method is validated by Heel et al. in a SI engine in various speed, load, equivalence ratio and spark timing [74], the accurate location of flame front could not be solved. The value of c is between 0 and 1 representing the probability of flame front location.

The G-equation is a good method to overcome the limitation of FAE model. The G-equation model is based on the level-set method, a numerical technique which can follow the evolution of interfaces [75]. Level-set method tracks the motion of an interface by embedding the interface as the zero level set of the signed distance function. The motion of the interface is matched with the zero level set function resembles a Hamilton-Jacobi equation. In this setting, curvatures and normal may be easily evaluated, topological changes occur in a natural manner, and the technique extends trivially to three dimensions [75].

Level-set method is applied to describe the flame front propagation and this model is G-equation. The flame surface is defined as the iso-surface of $G(\vec{x}, t) = G_0$, and G_0 is typically selected to be zero. Here, G is a non-reacting scalar. The iso-surface divides the flow field into an unburned region $G(\vec{x}, t) < 0$ and $G(\vec{x}, t) > 0$ denotes the burned region as shown in Figure 2.3.3.

Differentiating equation $G(\vec{x}, t) = 0$ with respect to the time, a transport equation for the G is obtained as

$$\frac{\partial G}{\partial t} + \nabla G \cdot \frac{\partial \vec{x}}{\partial t} = 0 \tag{2.3.4}$$

In this equation, the second term, $\frac{\partial \vec{x}}{\partial t}$, in l.h.s means the flame front propagation velocity. Flame propagation velocity consisted of bulk flow velocity at the flame front and flame front burning velocity in the normal direction, $\vec{n}$. $\vec{n}$ is the vector normal to the front in the direction of the unburned gas and it could be represented using G as,

$$\vec{n} = \frac{\nabla G}{|\nabla G|}\Big|_{G=0.0} \tag{2.3.5}$$

Combined with equation (2.3.4) and (2.3.5), a useful equation is generated like as,

$$\frac{\partial G}{\partial t} + \vec{v} \cdot \nabla G = S_L |\nabla G| \tag{2.3.6}$$

This equation is defined at the flame front $G(\vec{x}, t) = 0$ and it is called the G-equation [76].

The laminar flame speed S_L could be decomposed to each term [77, 78].

$$S_L = S_L^0 - S_L^0 Lk - LS \tag{2.3.7}$$

where S_L^0 is the burning velocity of the unstretched planar flame, and k is the flame curvature,

$$k = \nabla \cdot \vec{n} \cdot \left(-\frac{\nabla G}{|\nabla G|}\right) \tag{2.3.8}$$

S is the strain rate imposed on the flame by the velocity gradient and is defined by

$$\mathrm{S} = -\vec{n} \cdot \vec{v} \cdot \vec{n} \tag{2.3.9}$$

L is the Markstein length. It means the effect of strain and curvature on localized burning velocity. The Markstein length divided by the flame thickness which has the same order of magnitude of Markstein length is the Markstein number that characterizes the effect of local heat release of a propagating flame on variations in the surface topology along the flame and the associated local flame front curvature.

Combined with equation (2.3.6) and (2.3.7), G-equation for laminar flame is formulated as

$$\frac{\partial G}{\partial t} + \vec{v} \cdot \nabla G = S_L^0 |\nabla G| - S_L^0 Lk |\nabla G| - LS |\nabla G| \tag{2.3.10}$$

As mentioned before, this G-equation is valid at the flame front. To apply this equation numerically all over the G-field, G values outside the flame front should be defined. The typical way to extend the G-field is to define the gradient of G as $|\nabla G| = 1$ [79]. The advantage of this extension method is $\mathrm{d}G$ can be related to the normal distance to the flame front as

$$dG = dx_n \tag{2.3.11}$$

x_n is the distance from the flame front in the normal direction of the flame front to the burned gas direction.

2.3.3 Flamelet model for turbulent premixed combustion

Based on the G-equation for laminar premixed combustion, G-equation for turbulent premixed combustion should be derived. In the corrugated flamelet region, the reactive-diffusive flame structure is embedded within eddies of the Kolmogorov scale size. So, the equation (2.3.10) would be applied but the curvature term $S_L^0 Lk |\nabla G|$ and the strain term $LS |\nabla G|$ could be neglected. Thus, equation (2.3.10) could be simplified as [61],

$$\frac{\partial G}{\partial t} + \vec{v} \cdot \nabla G = S_L^0 |\nabla G| \tag{2.3.12}$$

In the thin reaction zone regime, the Kolmogorov eddies could enter into the preheat zone. In this case, the laminar burning velocity is not well defined. Therefore, the basic equation (2.3.10) could not be applied directly to this regime. However, the inner layer is laminar because the inner layer is not disturbed by the turbulence. The location of the inner layer could be detected with the inner layer temperature, T_0. The temperature transport energy equation is formulated as

$$\rho \frac{\partial T}{\partial t} + \rho \vec{v} \cdot \nabla T = \nabla \cdot (\rho D \nabla T) + \dot{q}_r \tag{2.3.13}$$

D is the thermal diffusivity and $\dot{q}_r$ is the heat release rate due to chemical reaction.

If the flame front coincides the surface of inner layer temperature, G-equation could be constructed as [61]

$$\frac{\partial G}{\partial t} + \vec{v} \cdot \nabla G = (S_n + S_r)|\nabla G| - Dk|\nabla G| \tag{2.3.14}$$

S_n is the displacement speed due to normal diffusion and S_r is displacement speed due to chemical reaction defined as

$$S_n = \frac{\vec{n} \cdot \nabla (\rho D \vec{n} \cdot \nabla T)}{T} \tag{2.3.14}$$

$$S_r = \frac{\dot{q}_r}{\rho |\nabla G|} \tag{2.3.14}$$

The displacement speed could be neglected due to the analysis of the order of magnitude of other terms, yielding [61]

$$\frac{\partial G}{\partial t} + \vec{v} \cdot \nabla G - Dk|\nabla G| \tag{2.3.15}$$

From the equation (2.3.12) and (2.3.15), G-equation for the turbulent regimes could be formulated. A common equation up to the leading term can be written as,

$$\frac{\partial G}{\partial t} + \vec{v} \cdot \nabla G = S_L^0|\nabla G| - Dk|\nabla G| \tag{2.3.16}$$

By multiplying every term by density, equation (2.3.16) becomes

$$\rho\frac{\partial G}{\partial t} + \rho\vec{v} \cdot \nabla G = \rho S_L^0|\nabla G| - \rho Dk|\nabla G| \tag{2.3.16}$$

ρS_L^0 is the mass flow rate through an unstretched planar flame and is a constant. $\vec{v}$ is the bulk flow velocity at the flame front as mentioned before, D is the diffusion coefficient and k is the flame curvature as also mentioned before.

These scalar and vector could be decomposed as mentioned in 2.1.1. as,

$$G = \bar{G} + G', \quad v = \bar{v} + v' \tag{2.3.17}$$

The mean value of G could be calculated with probability density function as

$$\bar{G}(\vec{x}, t) = \int_{-\infty}^{\infty} GP(G{:}\,\vec{x}, t)dG \tag{2.3.18}$$

$\bar{G}(\vec{x}, t) = 0$ is the probability of location of flame front.

G could be split into another averaging method, Favre average as mentioned before,

$$G = \tilde{G} + G^{"}, \quad v = \tilde{v} + v^{"} \tag{2.3.19}$$

If this Favre averaged values are applied to the G-equation for the corrugated flamelet regime, equation (2.3.12) becomes

$$\bar{\rho}\frac{\partial \tilde{G}}{\partial t} + \bar{\rho}\overrightarrow{v_f} \cdot \nabla \tilde{G} = \rho S_L^0 |\overline{\nabla G}| - \nabla \cdot (\widetilde{\bar{\rho}\overrightarrow{v''}G''}) \tag{2.3.20}$$

For a steady one-dimensional turbulent flame, equation (2.3.20) can be simplified as

$$(\bar{\rho}\vec{u})\frac{\partial \tilde{G}}{\partial x} = \rho S_L^0 |\overline{\nabla G}| \tag{2.3.21}$$

The turbulent flame velocity, S_T^0, is assumed to depend on local mean quantities only. The mass flow rate through the flame is $\bar{\rho}\vec{u} = \bar{\rho}S_T^0$. Therefore, equation (2.3.21) becomes

$$(\bar{\rho}S_T^0)\frac{\partial \tilde{G}}{\partial x} = \rho S_L^0 |\overline{\nabla G}| \tag{2.3.22}$$

Since $dx = d\tilde{G}/|\nabla \tilde{G}|$, equation (2.3.22) could become

$$(\bar{\rho}S_T^0)|\nabla \tilde{G}| = \rho S_L^0 |\overline{\nabla G}| \tag{2.3.23}$$

The term $\nabla \cdot (\widetilde{\bar{\rho}\overrightarrow{v''}G''})$ is not solved easily and should be modeled as

$$-\nabla \cdot \left(\widetilde{\bar{\rho}\overrightarrow{v''}G''}\right) = \nabla \cdot (\bar{\rho}D_T \nabla \tilde{G}) \tag{2.3.23}$$

where D_T is the turbulent diffusivity. Equation (2.3.23) is split into a normal diffusion term and a curvature term.

$$\nabla \cdot \left(\bar{\rho}D_T \nabla \tilde{G}\right) = \bar{n} \cdot \nabla\left(\bar{\rho}D_T \bar{n} \cdot \nabla \tilde{G}\right) - \bar{\rho}D_T \widetilde{k_M}|\nabla \tilde{G}| \tag{2.3.24}$$

where $\widetilde{k_M}$ is the curvature of the mean flame front calculated from

$$\widetilde{k_M} = \tilde{\vec{n}} \cdot \nabla = \nabla \cdot \left(\frac{\nabla \tilde{G}}{|\nabla \tilde{G}|}\right) \tag{2.3.25}$$

Equation (2.3.24) could become as

$$-\nabla \cdot \left(\widetilde{\bar{\rho}\overrightarrow{v''}G''}\right) = -\bar{\rho} D_T \widetilde{k_M} \left|\nabla \tilde{G}\right| \tag{2.3.26}$$

Since the diffusion normal to the $\tilde{G}$ iso-surface has been included in the burning velocity, it disappeared in equation (2.3.26)

Therefore, the Favre averaged G-equation for the corrugated flamelet regime becomes

$$\bar{\rho}\frac{\partial \tilde{G}}{\partial t} + \bar{\rho}\overrightarrow{v_f} \cdot \nabla \tilde{G} = \bar{\rho} S_T^0 \left|\nabla \tilde{G}\right| - \bar{\rho} D_T \widetilde{k_M} \left|\nabla \tilde{G}\right| \tag{2.3.27}$$

With the same way, Favre averaged G-equation for the thin reaction zone regime becomes [61]

$$\bar{\rho}\frac{\partial \tilde{G}}{\partial t} + \bar{\rho}\overrightarrow{v_f} \cdot \nabla \tilde{G} = \bar{\rho} S_T^0 \left|\nabla \tilde{G}\right| - \bar{\rho} D_T \widetilde{k_M} \left|\nabla \tilde{G}\right| \tag{2.3.28}$$

Equation (2.3.27) and (2.3.28) show the same form, so the common equation for the turbulent regimes is equation (2.3.28). If S_T^0 is estimated by regarding the unburned gas density, ρ_u, the mass flow rate, $\bar{\rho} S_T^0$, becomes $\overline{\rho_u} S_T^0$. $\bar{\rho}$ is the gas density at the mean flame front position. From this assumption, equation (2.3.28) becomes

$$\bar{\rho}\frac{\partial \tilde{G}}{\partial t} + \bar{\rho}\overrightarrow{v_f} \cdot \nabla \tilde{G} = \overline{\rho_u} S_T^0 \left|\nabla \tilde{G}\right| - \bar{\rho} D_T \widetilde{k_M} \left|\nabla \tilde{G}\right| \tag{2.3.29}$$

In a conventional SI engine combustion, combustion stays in a corrugated flamelet regime, not in a thin reaction zone regime generally [80]. Dual-fuel combustion also has the similar combustion regimes because momentum where the ignition is occurred by the injected fuel is weakened. The last term in r.h.s, $\bar{\rho} D_T \widetilde{k_M} \left| \nabla \tilde{G} \right|$, is the restoration term by turbulence. However the restoration is not dominant during the flame propagation duration. Therefore, we used equation (2.3.29) except the last term in r.h.s. in this research.

2.3.4 Numerical calculation of laminar flame speed

The laminar flame speed or laminar burning velocity model plays an important role in flame propagation model because it is an essential part in SI engine combustion. It determines the turbulent burning velocity and flame thickness. Therefore, many previous researches have been investigated the laminar flame speed by experimental measurements or numerical calculations. In the case of experiments, it is very difficult to measure the laminar flame speed because the fuel is hard to be gasified before combustion at room temperature. In addition, the effect of stretch, heat loss and buoyancy at high pressure and temperature conditions are difficult to be eliminated completely in experimental conditions.

On the contrary, numerical calculation for the laminar flame speed of hydrocarbon fuels seems to be suitable to predict accurately [81]. If such prediction by calculation is well matched to the experimental data over wide ranges of temperature and pressure conditions, it could be used to the simulation by approximated expressions. When a planar steady-state premixed flame normal to the x-direction with the unburned mixture goes to negative infinite and burned mixture goes to positive infinite, the one-dimensional isobaric balance equations for continuity, mass fractions of the chemical species and energy are written as,

$$\frac{d(\rho v)}{dx} = 0 \tag{2.3.30}$$

$$\rho v \frac{dY_i}{dx} = \frac{dj_i}{dx} - \omega_i \tag{2.3.31}$$

$$\rho v c_p \frac{dT}{dx} = \frac{d}{dx}\left(\lambda \frac{dT}{dx}\right) - \sum_{i=1}^{n} h_i \omega_i - \sum_{i=1}^{n} c_{p,i} j_i \frac{dT}{dx} \tag{2.3.32}$$

where v is the velocity in x-direction, ρ is the density, Y_i is the mass fraction of species *i*, c_p and $c_{p,i}$ is the specific heat of the mixture and species *i* at constant pressure, respectively. j_i is the diffusion flux of species *i*, λ is the thermal conductivity, h_i is the specific enthalpy of species *i*, ω_i is the chemical production rate of species *i*.

The continuity equation may be integrated to yield the laminar flame speed, S_L, defined with respect to the unburned mixture as an eigenvalue of the problem as

$$\rho v = \rho_u v_u \tag{2.3.33}$$

This laminar flame speed is calculated by PREMIX code [82] that utilizes modified damped Newton's method and adaptive grid refinement was used to solve the governing equations of one-dimensional premixed flame in conjunction with the CHEMKIN and TRANSPORT subroutine [83, 84]. The laminar flame speed data of gasoline was obtained by this method and validated in the previous works [85]. In this research, laminar flame speed of the lower reactivity fuels such as iso-octane and propane are calculated using this method. Figure 2.3.4 shows the laminar flame speed of the propane in various temperature and pressure conditions. The initial equivalence ratio is not 1 but 0.4 which is an ordinary condition of dual-fuel combustion.

The laminar flame speed needs to be converted into turbulent flame speed due to the in-cylinder turbulent motion to be used in CFD code. The turbulence velocity was evaluated by Peters as [86]

$$S_T = S_L + u' \left\{ -\frac{ac^2}{2b} Da + \left[\left(\frac{ac^2}{2b} Da \right)^2 + ac^2 Da \right]^{1/2} \right\} \qquad (2.3.31)$$

where u' is the turbulence intensity, and $a = 0.78$, $b = 2.0$, $c = 1.0$ are constants derived from the turbulence model and $Da = S_L l / u' l_F$ and l is the turbulence integral length scale. Finally, $l_F = (\lambda / c_p)_0 / (\rho S_L)_u$ is the flame thickness. The heat conductivity, λ, and heat capacity, c_p, are evaluated at the inner layer temperature.

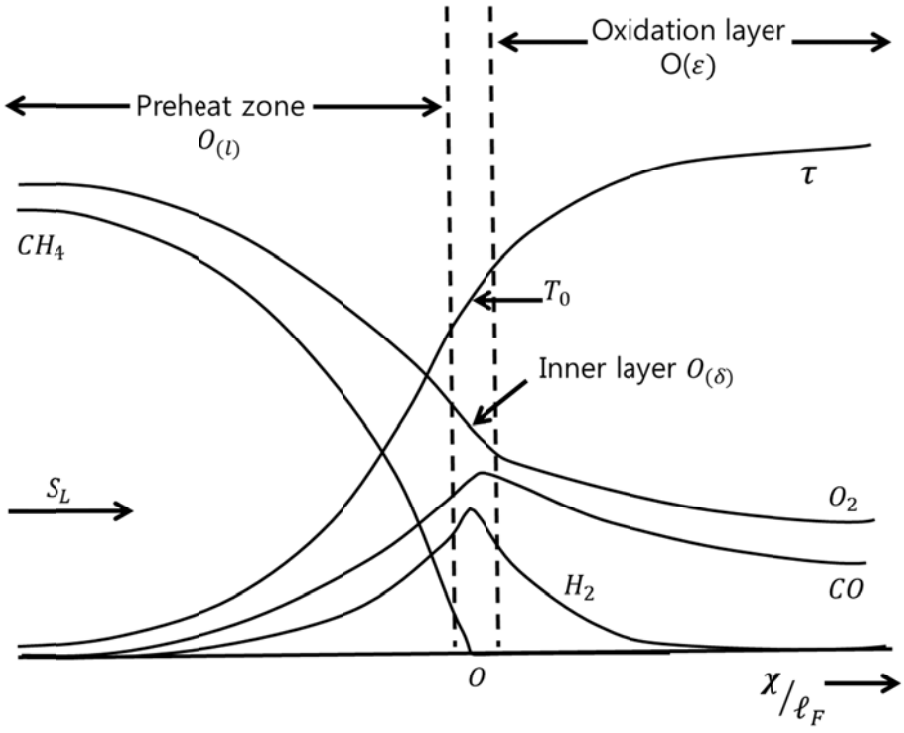

Figure 2.3.1 The structure of a laminar, stoichiometric methane-air flame [66]

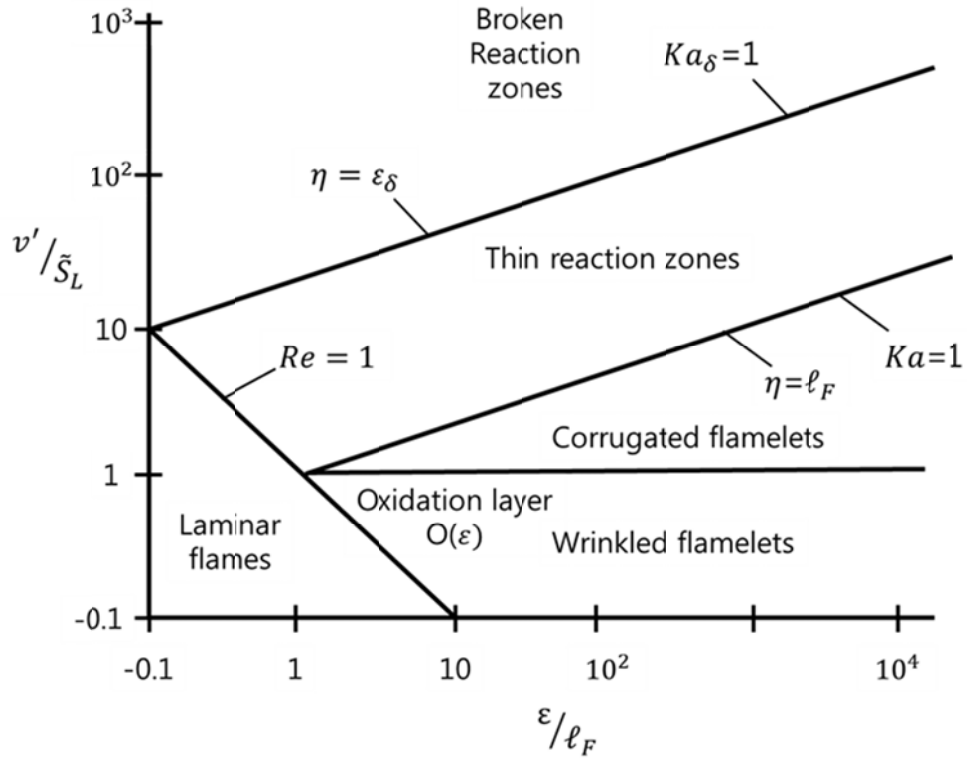

Figure 2.3.2 Regime diagram for premixed turbulent combustion [86]

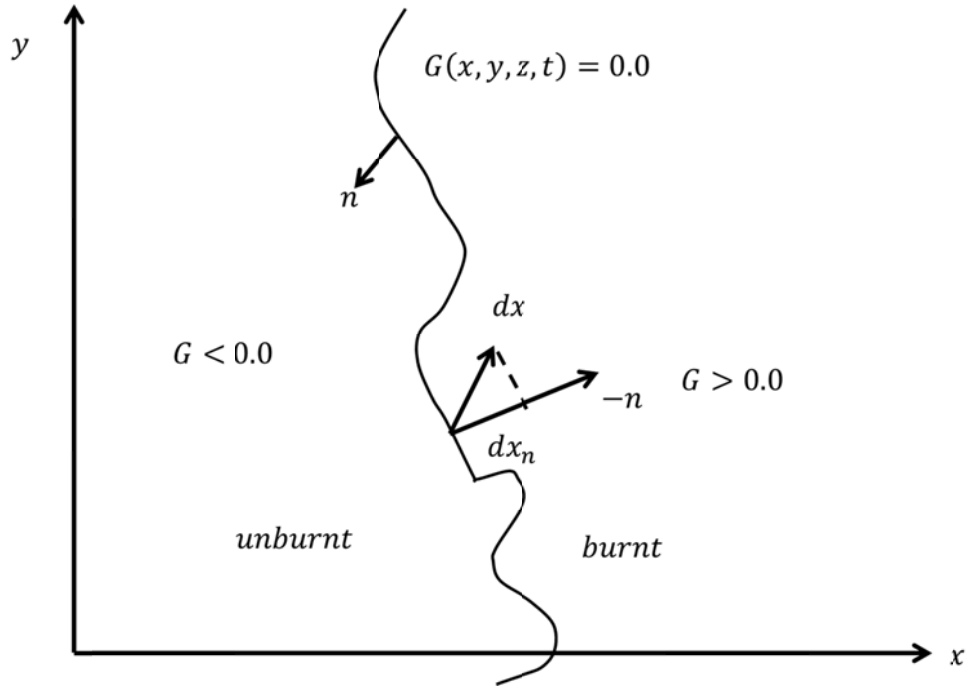

Figure 2.3.3 Flame front defined by the iso-scalar surface G(x,t) = 0 [86]

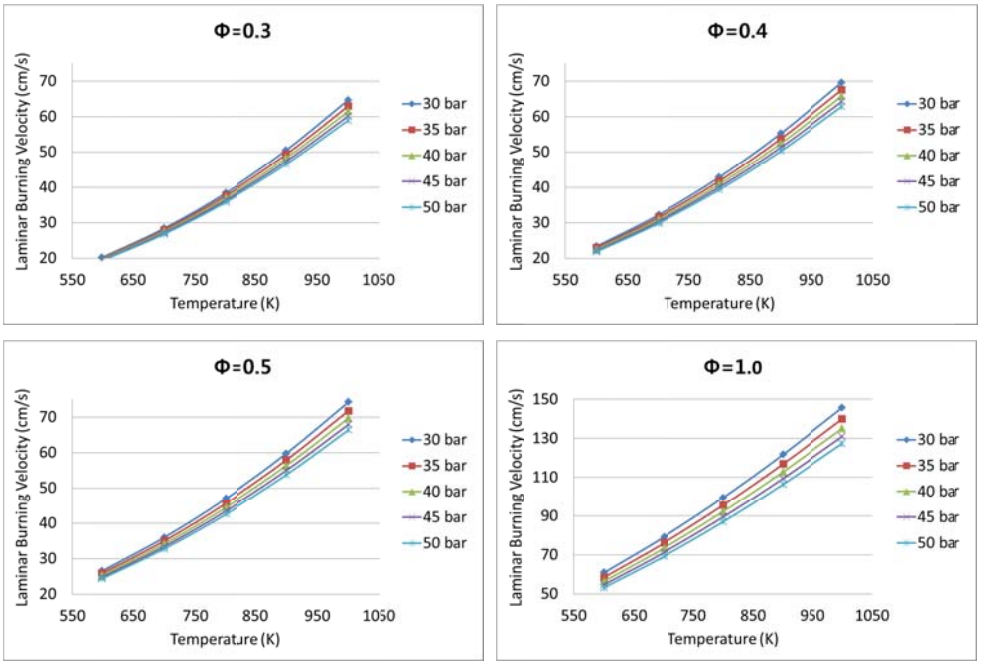

Figure 2.3.4 Laminar flame speed of propane in the various ambient temperature and pressure conditions (Equivalence ratio:0.3, 0.4, 0.5, 1.0)

2.4 Modeling of burnt gas composition

Classically, mass fractions of species in burned region are mapped as the burned species with the perfect combustion assumption in premixed combustion models. However, it could not reflect the combustion rate and could not have unburned species mass fraction or intermediate radicals. Since dual-fuel combustion is occurred after the auto-ignition of the liquid injected fuel in conventional Diesel engine, it is affected by the turbulence induced by swirl or tumble motion and momentum by injection. Therefore, although there are not much gradient of mixture fraction in dual-fuel combustion engine, mass fraction in the burned region should be reflected by the turbulence.

In this research, the steady-state solution of flamelet equations were obtained at various flamelet boundary conditions and composed into a flamelet library for numerical implementation.

2.4.1 Flamelet library approach

In dual-fuel combustion, flame propagation is occurred after the ignition of the second injected fuel. Generally, burned gas composition from the equilibrium calculation should be assigned behind the flame sheet. This burned gas composition is based on the assumption that the grid is perfectly mixed and calculated by the thermodynamic data at each temperature, pressure and species concentration conditions. However, there are turbulent effects in the physical in-cylinder such as turbulent kinetic energy or turbulent energy dissipation rate at each grid.

As mentioned in previous chapter 2.2.2, flamelet model could reflect the turbulent effects using scalar dissipation rate. This method is very useful because the three-dimensional vector could be described by one scalar. Premixed

combustion could also be expressed by conserved scalar $\tilde{Z}$ and $\widetilde{Z''^2}$ like non-premixed combustion. Basic equations and concepts are same to those of non-premixed combustion as documented in chapter 2.2.2. Unlike the non-premixed combustion, only one mixture fraction value exists in premixed combustion because the equivalence ratio is fixed in premixed combustion and it is same in dual-fuel combustion. In premixed combustion condition, transient transport equation is not solved but the pre-calculated steady-state solution of flamelet equations in Eqs. (2.1.18) and (2.1.19) should be applied to the burned gas composition. This approach has been applied to the previous studies on the flame structure of opposed flow diffusion flame by Pitsch and Peters [70], modeling of lifted turbulent jet diffusion flames [87], combustion modeling of premixed combustions in conventional SI and Diesel engines [88, 89], and GDI applications [85].

To use the flamelet library approach, steady-state flamelet solutions should be pre-calculated in the various conditions because transient solutions needs too much calculation costs. In the dual-fuel combustion, solutions according to the calculation time are not important because the states in front of the flame sheet and behind the flame sheet are totally different. Therefore, pre-calculated flamelet solutions could be mapped to the behind of the flame sheet as the burned gas composition. The species concentrations calculated from the flamelet equations are Favre-averaged by a presumed PDF function as the final solutions as

$$\tilde{Y}_{i,b}\left(\tilde{Z}, \widetilde{Z''^2}, \widetilde{\chi_{st}}\right) = \int_0^1 Y_i(Z, \chi_{st}) P(Z) dZ \tag{2.4.1}$$

Here, $Y_i(Z, \chi_{st})$ is calculated by the flamelet equations for the first injected fuel. If the region is within the turbulent flame brush, the species concentrations are interpolated with the burned species and unburned species as

$$\tilde{Y}_i = c\tilde{Y}_{i,b} + (1-c)\tilde{Y}_{i,u} \tag{2.4.2}$$

2.4.2 Library generation

These flamelet libraries should be pre-calculated due to the calculation time. However, parameters from the flow field such as temperature, pressure and scalar dissipation rate which need to calculate flamelet equations could not be provided directly. Therefore, representative parameters should be selected to pre-calculate the flamelet equations and then the instantaneous species concentrations in the flow field should be interpolated from the pre-calculated representative solutions. The representative parameters are selected from the previous research [85]. In this research, the steady-state solutions of flamelet equations were obtained at various temperatures, scalar dissipation rates and equivalence ratio conditions. These conditions are listed in Table 2.4.1. The major species concentration with respect to the mixture fraction at the condition of initial temperature 1100 K and initial pressure 50 bar was shown in Figure 2.4.1.

Table 2.4.1 Calculation conditions for flamelet library of the first injected fuels

Parameter	Value	Description	No. of validation
Temperature (K)	700~1200	100 K interval	6
Mixture fraction	0~1	0~0.2: 0.001 interval 0.2~1: 0.04 interval	141
Scalar dissipation rate (1/s)	0.01~20	0.01, 0.1, 1, 2, 5, 10, 20	7

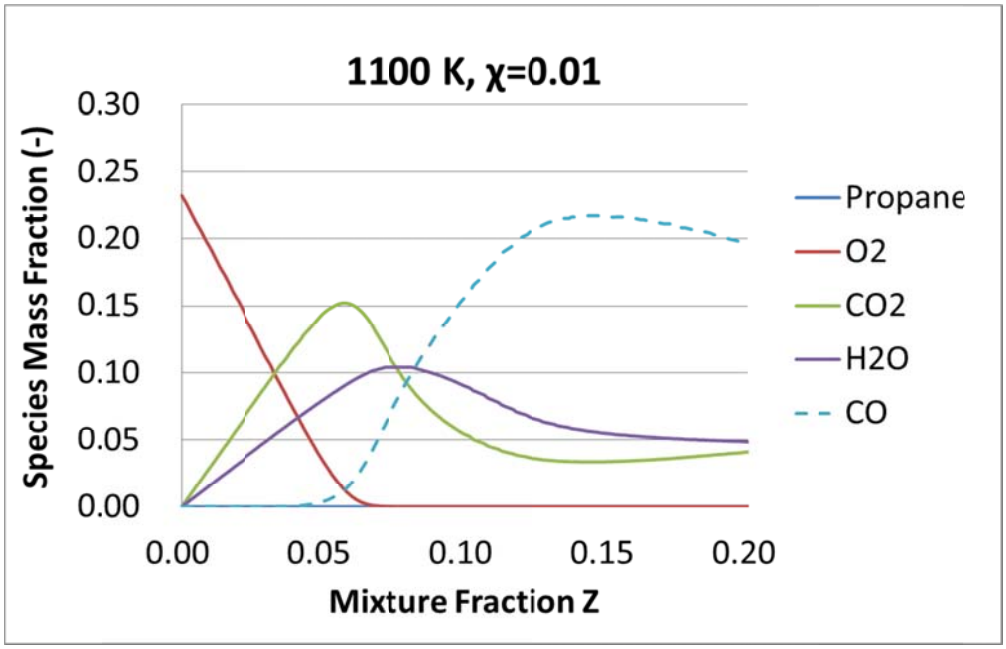
1100 K, χ=0.01
Species Mass Fraction (-)
0.30
0.25
0.20
0.15
0.10
0.05
0.00
0.00
0.05
0.10
0.15
0.20
Mixture Fraction Z
Propane
O2
CO2
H2O
CO

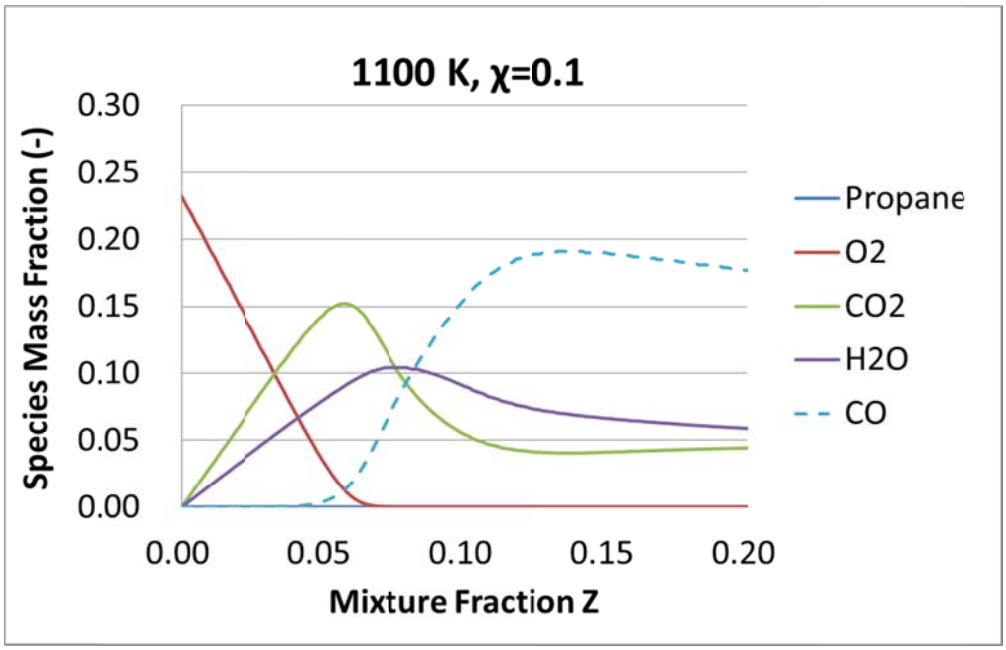
1100 K, χ=0.1
Species Mass Fraction (-)
0.30
0.25
0.20
0.15
0.10
0.05
0.00
0.00
0.05
0.10
0.15
0.20
Mixture Fraction Z
Propane
O2
CO2
H2O
CO

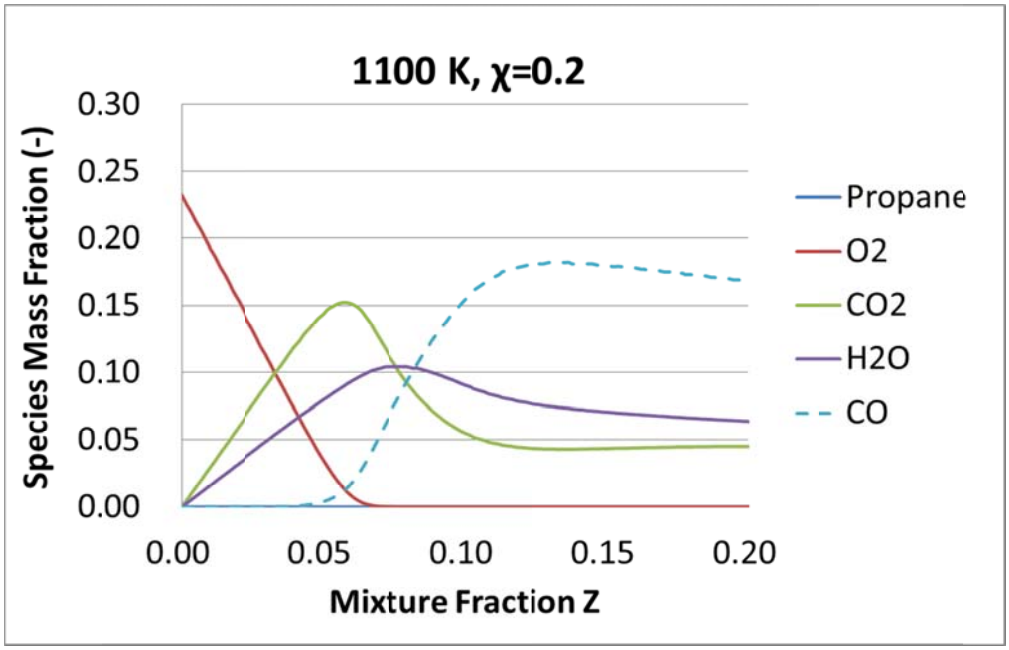
1100 K, χ=0.2
Species Mass Fraction (-)
0.30
0.25
0.20
0.15
0.10
0.05
0.00
0.00
0.05
0.10
0.15
0.20
Mixture Fraction Z
Propane
O2
CO2
H2O
CO

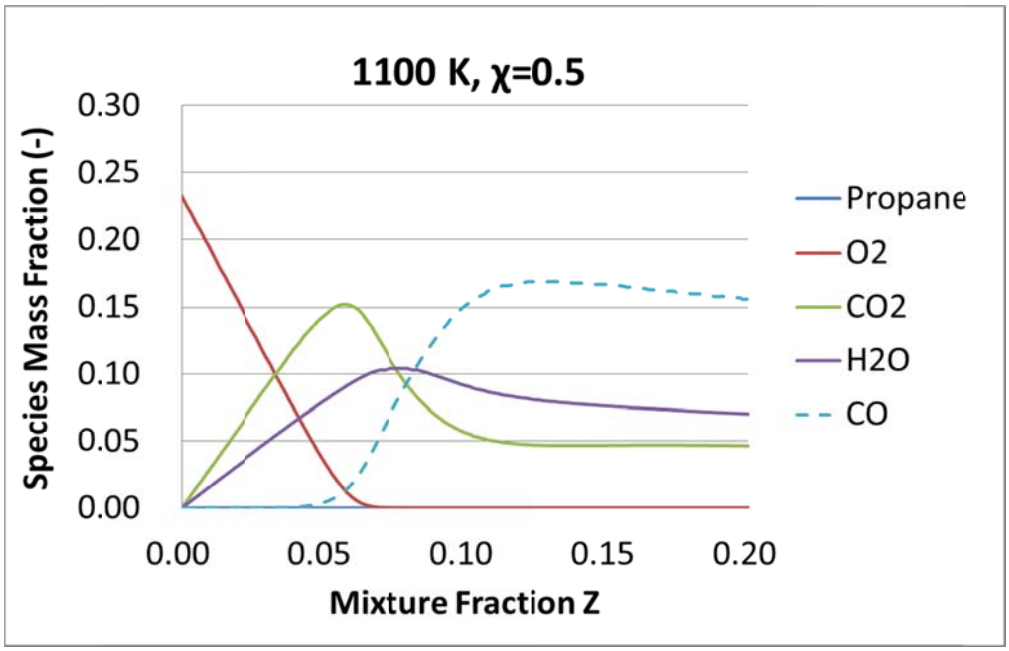
1100 K, χ=0.5
Species Mass Fraction (-)
0.30
0.25
0.20
0.15
0.10
0.05
0.00
0.00
0.05
0.10
0.15
0.20
Mixture Fraction Z
Propane
O2
CO2
H2O
CO

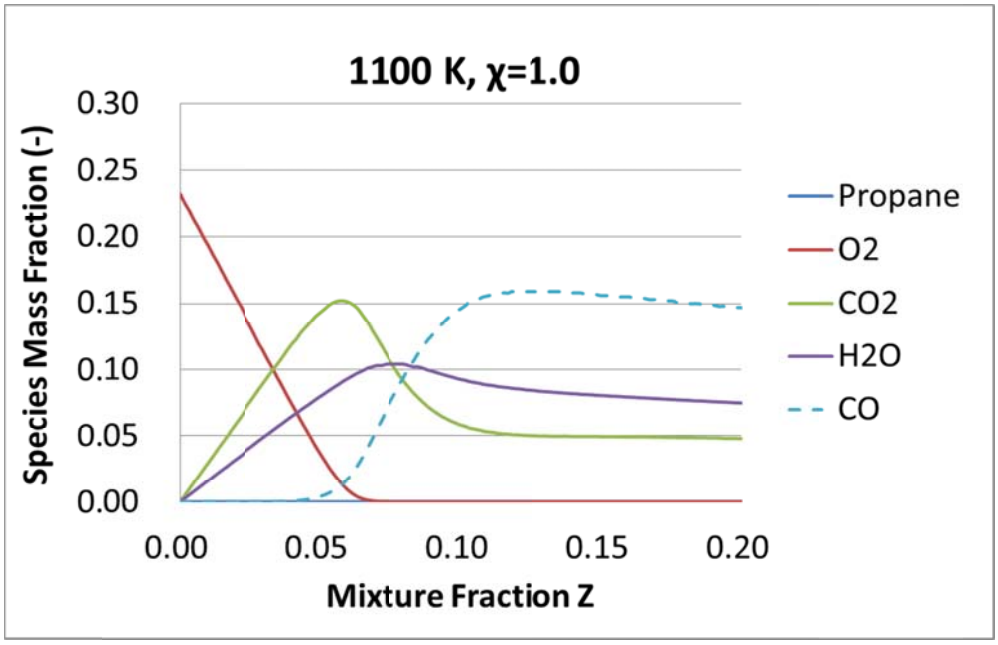
1100 K, χ=1.0
Species Mass Fraction (-)
0.30
0.25
0.20
0.15
0.10
0.05
0.00
0.00
0.05
0.10
0.15
0.20
Mixture Fraction Z
Propane
O2
CO2
H2O
CO

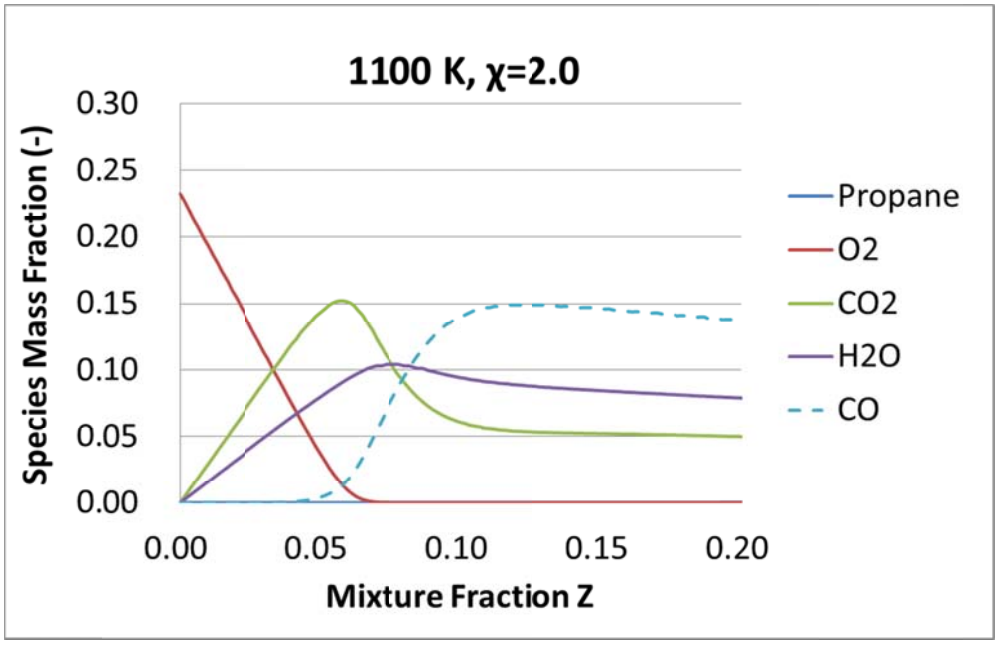
1100 K, χ=2.0
Species Mass Fraction (-)
0.30
0.25
0.20
0.15
0.10
0.05
0.00
0.00
0.05
0.10
0.15
0.20
Mixture Fraction Z
Propane
O2
CO2
H2O
CO

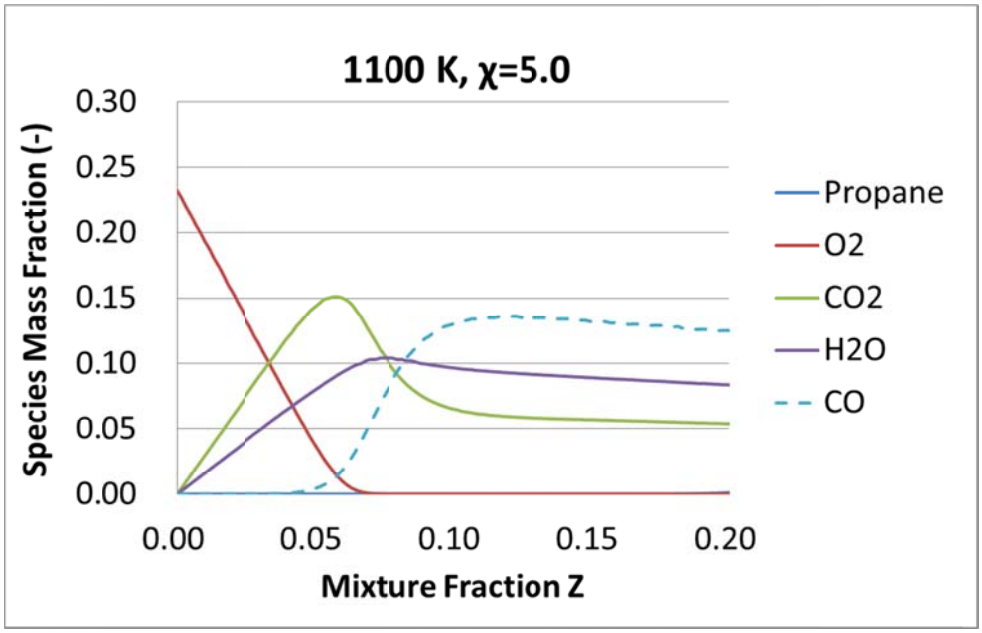

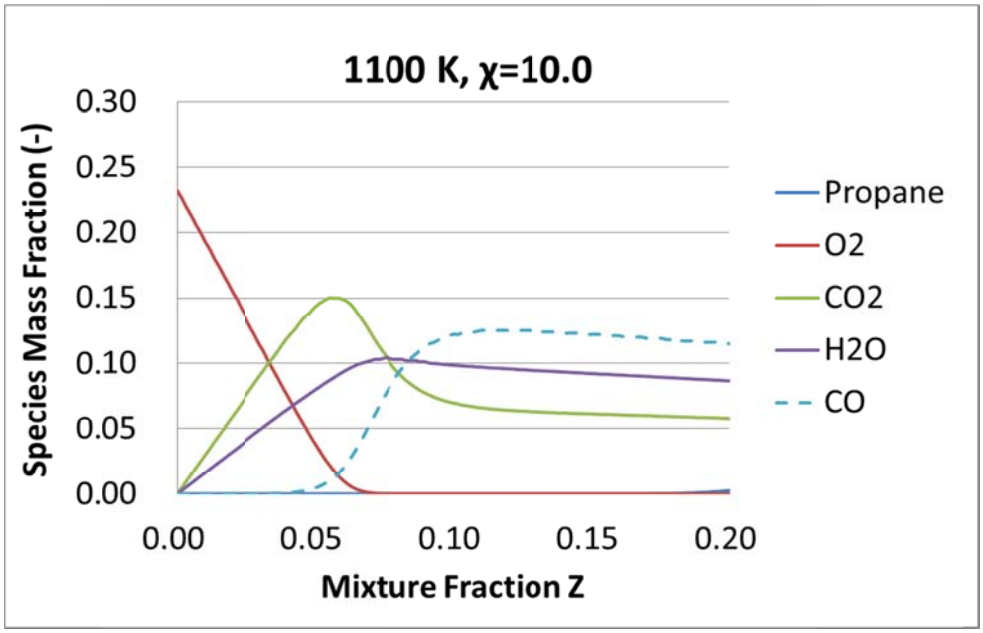

Figure 2.4.1 Flamelet steady-state solution library for the propane and n-heptane chemical kinetics in a various scalar dissipation rate and equivalence ratio at the initial temperature 1100 K and no EGR condition.

2.5 Chemical Kinetics

2.5.1 Normal heptane

Generally, Diesel is used to be selected as a higher reactivity fuel in the dual-fuel studies. In this study, n-heptane was used to simulate the Diesel fuel because the ignition delay time is very similar to that of Diesel. Chemical kinetics of n-heptane used in this study was developed and validated by Lee et. al. [90]. The mechanism is consisted of 32 species and 44 reactions.

2.5.2 Propane

Various gaseous or liquid fuels are used as the lower reactivity fuel in the dual-fuel studies generally. Among them, propane was chosen as the lower reactivity fuel in this study because propane is easy to apply to the experiment. To use the propane chemical kinetic mechanism and n-heptane mechanism simultaneously, a new reduced chemical kinetic mechanism including both n-heptane and propane need to be developed. To combine the two mechanisms into one, a new reduced propane mechanism was developed based on the propane mechanism developed by USC which is consisted of 50 species and 244 reactions because the form of the two mechanisms need to be similar due to the combination. The new propane chemical kinetics uses the reaction set for the low molecular weight species used in the n-heptane mechanism. And the total mechanism follows the general oxidation scheme.

Figure 2.5.1 shows the comparison of the ignition delay time between new developed propane mechanism and USC mechanism at 40 bar of the initial pressure, 1 of the equivalence ratio and various initial temperature conditions. The ignition

delay time of the new reduced propane mechanism is well matched to the original chemical mechanism by USC.

The combined chemical kinetic mechanism of n-heptane and propane was shown in Table 2.5.1. It was consisted of 43 species and 70 reactions.

Table 2.5.1 Chemical kinetics of dual-fuel composition (n-heptane and propane)

No.	Reactions	A	b	Ea
1	$C_3H_8+O=IC_3H_7+OH$	2.60E	0	18700
2	$C_3H_8+O=nC_3H_7+OH$	3.00E	0	24100
3	$C_3H_8+H=IC_3H_7+H_2$	1.00E	0	34900
4	$C_3H_8+H=nC_3H_7+H_2$	1.30E	0	40600
5	$C_3H_8+OH=IC_3H_7+H2O$	2.80E	0	3600
6	$C_3H_8+OH=nC_3H_7+H_2O$	3.70E	0	6900
7	$nC_3H_7+H_2O_2=HO_2+C_3H_8$	3.78E	2.7	1500
8	$IC_3H_7+H_2O_2=HO_2+C_3H_8$	3.78E	2.7	1500
9	$nC_3H_7+O_2=C_3H_6OOH$	2.00E	0	0
10	$C_3H_6OOH=C_3H_6+HO_2$	1.24E	-8.3	22
11	$C_3H_6OOH+O_2=OC_3H_5OOH+OH$	1.50E	0	-7
12	$OC_3H_5OOH=CH_2CHO+CH_2O+OH$	1.00E	0	43
13	$IC_3H_7+O=C_2H_5+CH_2O$	9.64E	0	0
14	$nC_3H_7+H(+M)=C_3H_8(+M)$	3.61E	0	0
	Low Pressure Limit: 4.42E+61, -1.35E+01, 1.14E+04 H_2 2.0 / H_2O 6.0 / CH4 2.0 / CO 1.5 / CO_2 2.0 / C_2H_6 3.0			
15	$IC_3H_7+H(+M)=C_3H_8(+M)$	3.61E	0	0
	Low Pressure Limit: 4.42E+61, -1.35E+01, 1.14E+04 H_2 2.0 / H_2O 6.0 / CH_4 2.0 / CO 1.5 / CO_2 2.0 / C_2H_6 3.0			
16	$H+nC_3H_7=CH_3+C_2H_5$	4.06E	2.2	890
17	$OH+IC_3H_7=C_2H_5+CH_2OH$	2.41E	0	0
18	$nC_3H_7+HO_2=O_2+C_3H_8$	2.55E	0.3	-943
19	$IC_3H_7+HO_2=O_2+C_3H_8$	2.55E	0.3	-943
20	$IC_3H_7+HO_2=OH+C_2H_5+CH_2O$	2.41E	0	0
21	$IC_3H_7+CH_3=_2C_2H_5$	1.93E	-0.3	0
22	$IC_3H_7+H=C_2H_5+CH_3$	3.70E	-2.9	12505
23	$IC_3H_7+H=C_3H_6+H_2$	1.80E	0	0
24	$IC_3H_7+OH=C_3H_6+H_2O$	2.40E	0	0
25	$nC_3H_7=CH_3+C_2H_4$	2.00E	0	29500

26	C_2H_3+O=CO+CH_3	5.00E	0	0
27	C_2H_2+OH=CH_3+CO	4.83E-	4	-2000
28	C_7H_{16}+OH=C_7H_{15}-2+H_2O	4.80E	1.3	690.5
29	C_7H_{16}+O_2=C_7H_{15}-2+HO_2	2.80E	0	47180
30	C_7H_{16}+H=C_7H_{15}-2+H_2	4.38E	2	4750
31	C_7H_{16}+HO_2=C_7H_{15}-2+H_2O_2	1.10E	0	16950
32	C_7H_{15}-2=IC_4H_9+C_3H_6	1.90E	0	29600
33	C_7H_{15}-2+O_2=$C_7H_{15}O_2$	2.00E	0	0
34	$C_7H_{15}O_2$=$C_7H_{14}O_2H$	6.00E	0	20380
35	$C_7H_{14}O_2H$+O_2=$C_7H_{14}O_2HO_2$	2.38E	0	0
36	$C_7H_{14}O_2HO_2$=C_7KET_{21}+OH	2.97E	0	26700
37	C_7KET_{21}=C_5H_{11}CO+CH_2O+OH	1.00E	0	42400
38	C_5H_{11}CO=C_5H_{11}+CO	1.00E	0	9600
39	C_5H_{11}=IC_4H_8+CH_3	5.00E	0	26000
40	O+OH=O_2+H	6.40E	-0.5	0
41	H_2+O=H+OH	1.82E	1	8900
42	OH+OH=O+H_2O	6.00E	1.3	0
43	H_2O+H=H_2+OH	9.55E	0	20300
44	H_2O_2+OH=H_2O+HO_2	1.00E	0	1800
45	H_2O+M=H+OH+M	2.19E	0	105000
	H_2O 20.0 / CO_2 5.0 / CO 2.0 / H_2 3.3			
46	H+O_2+M=HO_2+M	3.61E	-0.7	0
	N_2 0.7			
47	HO_2+OH=H_2O+O_2	5.01E	0	1000
48	H_2O_2+O_2=HO_2+HO_2	3.98E	0	42640
49	H_2O_2(+M)=OH+OH(+M)	3.00E	0	48500
	Low Pressure Limit: 2.0E+17, 0.0E0, 4.85E+4			
	H_2 2.0 / H_2O 12.0 / CO 1.9 / CO_2 3.8			
50	H_2+M=H+H+M	2.19E	0	96000
	H_2O 6.0 / H_2 3.0 / CO_2 3.8			
51	CO+OH=CO_2+H	6.32E	1.5	-497
52	CO+HO_2=CO_2+OH	1.51E	0	23650

53	$CO+O+M=CO_2+M$	6.17E	0	3000
	N_2 0.7			
54	$HCO+O_2=CO+HO_2$	3.98E	0	0
55	$IC_4H_9=C_2H5+C_2H_4$	2.50E	0	28810
56	$IC_4H_8+O=IC_3H_7+HCO$	7.24E	2.3	-1050
57	$C_3H_6+OH=C_2H_5+CH_2O$	1.00E	0	0
58	$C_3H_6+OH=CH_3+CH_3CHO$	1.00E	0	0
59	$C_2H_5+O_2=C_2H_4+HO_2$	1.00E	0	5000
60	$C_2H_4+OH=CH_3+CH_2O$	2.00E	0	960
61	$C_2H_4+HO_2=CH_3CHO+OH$	2.20E	0	17200
62	$CH_3+HO_2=CH_3O+OH$	4.30E	0	0
63	$CH_3CHO+HO_2=CH_2CHO+H_2O_2$	3.00E	0	15000
64	$CH_3O+M=CH_2O+H+M$	5.01E	0	21000
65	$O_2+CH_2CHO<=>OH+2HCO$	2.35E	0	0
66	$CH_2O+OH=HCO+H_2O$	3.59E	0	170
67	$CH_2O+O=HCO+OH$	5.01E	0	4600
68	$CH_3+HCO=CH_2O+CH_2$	3.00E	0	0
69	$CH_3+O=CH_2O+H$	8.00E	0	0
70	$CH_2+O_2=CO_2+H+H$	1.60E	0	1000

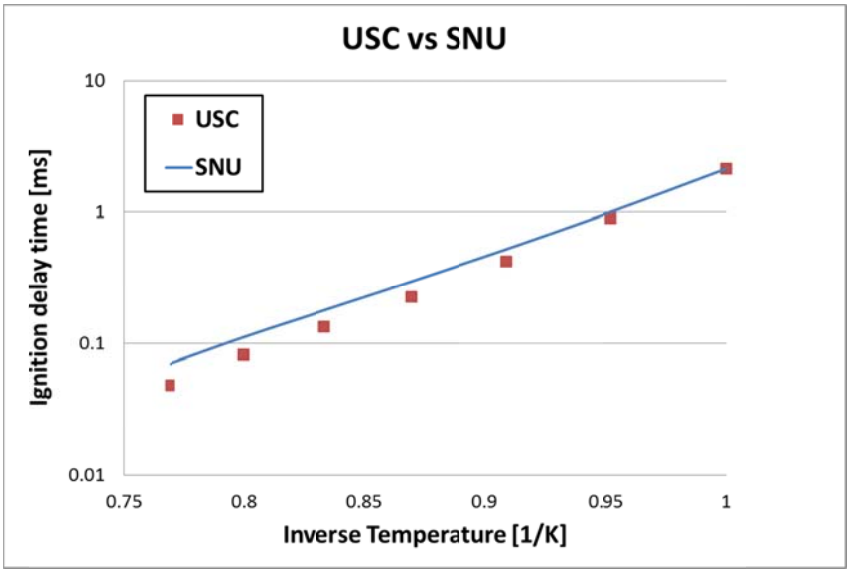

Figure 2.5.1 Comparison of the ignition delay time between new developed propane mechanism and USC mechanism at 40 bar of the initial pressure, 1 of the equivalence ratio and various initial temperature conditions.

2.6 Modeling of Emissions

2.6.1 NOx model

NO and NO2 are usually grouped together as NOx emissions. NOx is the major pollutants in CI engine because NOx could be fatal to human respiratory systems. The famous NOx formation mechanism is extended Zeldovich mechanism. The basic NOx formation and oxidation reactions are

$O + N2 \Leftrightarrow NO + N$
$N + O2 \Leftrightarrow NO + O$
$N + OH \Leftrightarrow NO + O$

The rate constants are listed in Table 2.6.1 which are used successfully at the previous study [85].

2.6.2 Soot model

Hiroyasu developed an empirical soot model[91] consisted of 2 reactions. The first one is soot formation reaction and the other is soot oxidation reaction. The limitation of this simple model is that it needs empirical coefficients to match the calculation data to the experimental data. The first phenomenological soot model was developed by Fusco et al [92]. The fuel is decomposed by pyrolysis into acetylene (C_2H_2) and soot precursor radicals. These are combined by inception and surface growth reactions or oxidized by O2 and OH radical. Combined small soot particles are coagulated into soot particles or oxidized by O2 and OH radical. This basic concept has been developed continuously. Recently, Feng developed the newest phenomenological soot model based on the Fusco's model consists of 9 processes with C_2H_2 and soot precursor radical [93]. Figure 2.6.1 shows the

schematic flow of Feng's phenomenological model and Feng's soot model was used in this study.

Table 2.6.1 Specific reaction-rate constants for NO formation mechanism [94]

NO	NO	NO
1f	$O + N_2 \rightarrow NO + N$	$1.15 \times 10^{14} \exp(-38{,}000/T)$
1b	$NO + N \rightarrow O + N_2$	1.6×10^{13}
2f	$N + O_2 \rightarrow NO + O$	$6.4 \times 10^{9} T(-3{,}150/T)$
2b	$NO + O \rightarrow O_2 + N$	$1.5 \times 10^{9} T\exp(-19{,}500/T)$
3f	$N + OH \rightarrow NO + H$	4.1×10^{13}
3b	$H + NO \rightarrow OH + N$	$2.0 \times 10^{14} \exp(-23{,}650/T)$

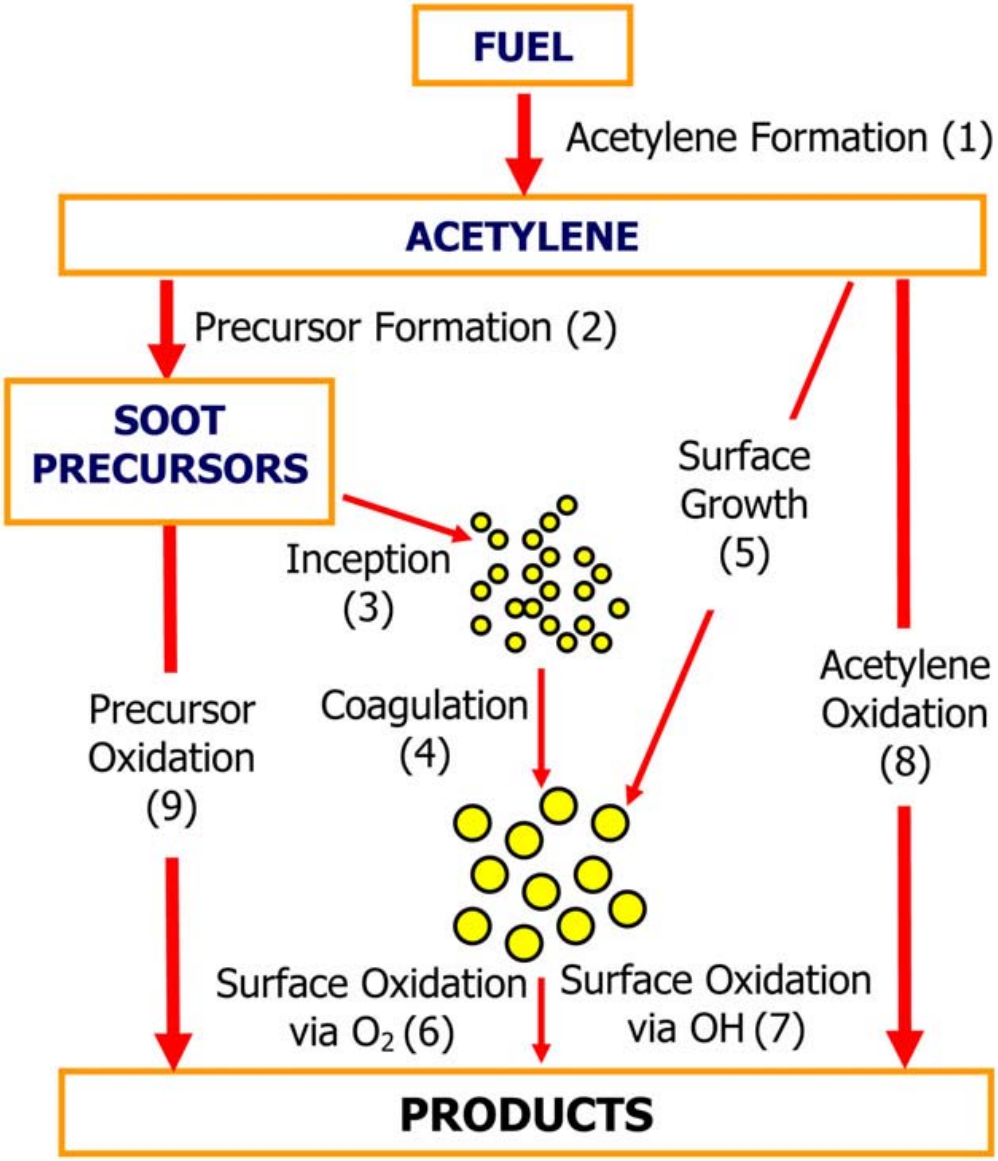

Figure 2.6.1 Schematic diagram of Feng's phenomenological soot model

2.7 Summary of Modeling

Figure 2.7.1 shows the architecture of the combustion model developed in this study. Key topic is that one combustion model could not be applied to the classic dual-fuel combustion only but also be applied to the RCCI combustion. The lower reactivity fuel is injected very early timing for all the classical dual-fuel combustion and RCCI combustion. The injected lower reactivity fuel has enough time to mix to the in-cylinder air during the compression stroke. Therefore, we assume that the lower reactivity fuel is perfectly mixed to the in-cylinder air in both combustion modes.

In the classical dual-fuel combustion case, higher reactivity fuel is injected near TDC. And then the higher reactivity fuel is ignited during the injection timing. Therefore, ignition source is generated from the spray of the higher reactivity fuel. Mixing time of the higher and lower reactivity fuel is not enough because ignition is occurred during the injection duration. This non-premixed combustion of the higher reactivity fuel is described by the RIF model. From the ignition source, flame propagates to the lower reactivity fuel outside of the spray of the higher reactivity fuel. This flame propagation is described by the level-set model.

In the RCCI combustion case, higher reactivity fuel is injected earlier than the classical dual-fuel combustion. Therefore, ignition is not occurred during the injection duration because the in-cylinder pressure and temperature is low. Injected higher reactivity fuel is mixed to the lower reactivity fuel and in-cylinder air but not perfectly mixed because the mixing time is not enough to mix perfectly. And then ignition is occurred near TDC due to high pressure and temperature. The bulk ignition is occurred as PCCI combustion. This PCCI combustion is described by RIF model.

Figure 2.7.2 summarizes the modeling of combustion and emission production of dual-fuel combustion engine in this study. The model was composed to consider the three essential aspects of dual-fuel combustion engine simulation which were

the ignition from the higher reactivity fuel, flame propagation and detailed burned gas composition, respectively. In this study, it is assumed that the first injected lower reactivity fuel is well mixed to the in-cylinder air. Therefore, CFD code solves the governing equations for turbulent flow field of the mixed air. After the second injection of the higher reactivity fuel, RIF model solves the non-premixed flame and ignition is occurred by this model. From the ignition points, flame propagation starts. The flame propagation speed is determined by competition between the ignition propagation from the laminar flamelet model and flame propagation from the level-set model because flame propagation could be occurred by the non-premixed flame and premixed flame together. At this stage, laminar flame speed is pre-calculated for the lower reactivity fuel and used as extensive library. During the combustion simulation, the chemical state of burning or burned flamelet was determined by being interpolated between the initial burned state and the final state extracted from library in accordance with the species equation.

In addition, emissions are solved in this study. NO and NO_2 were solved from reduced NOx mechanism which was developed by Song [95]. NOx were solved with the other species in RIF model and also pre-calculated as burned gas species. CO and THC were solved as the minor species of the chemical kinetics of the low and higher reactivity fuels. Finally, Soot formation by phenomenological model of Feng [93] was included in this study.

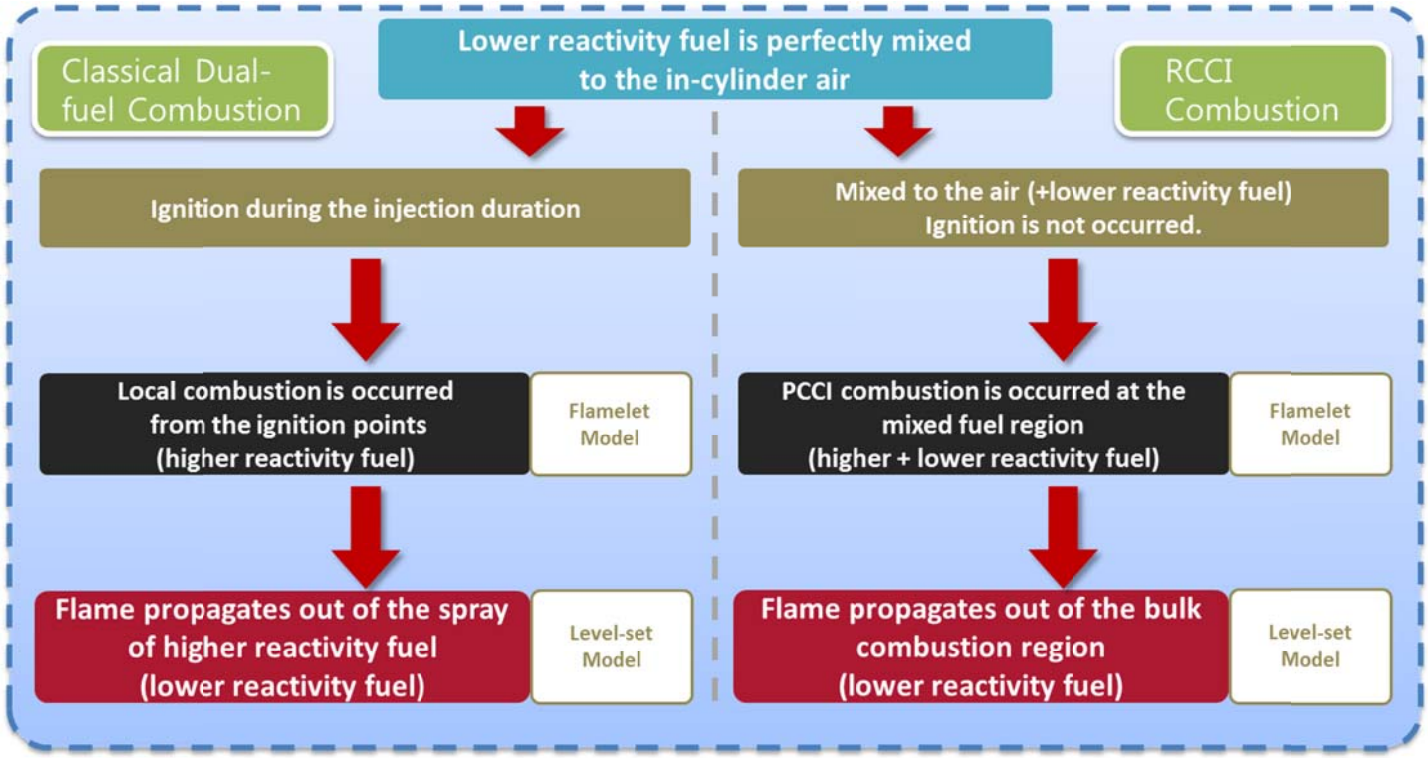

Figure 2.7.1 Model architecture and processes.

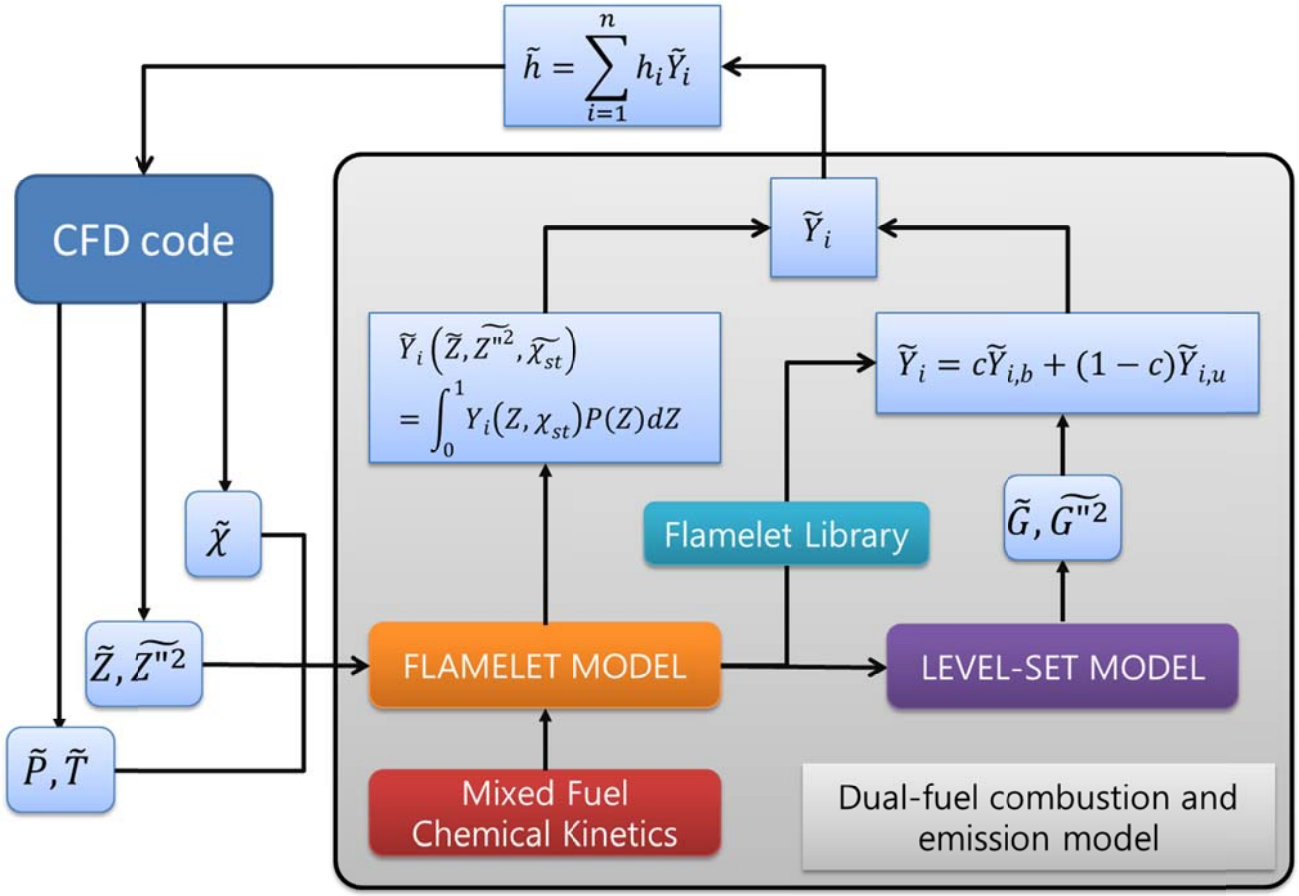

Figure 2.7.2. Schematics of model structure for dual-fuel combustion engine simulation and interaction with CFD code

Chapter 3. Simulation in a Simple Geometry

As documented in Chapter 1.2.1, the combustion characteristics of classical dual-fuel combustion and RCCI combustion is identical in dual-fuel combustion class. In classical dual-fuel combustion, injection timing is the same to the CI engine. Therefore, ignition is occurred during the injection duration and the mixing time between lower reactivity fuel and higher reactivity fuel is deficient. On the other hand, the mixing time between the two fuels is sufficient at RCCI condition because the injection timing of RCCI is very early. The higher reactivity fuel participates to the ignition and then the ignition is converted into flame propagation. In classical dual-fuel combustion, ignition is converted into flame propagation directly. However, in RCCI combustion, ignition is propagating firstly because ignition propagation speed of mixed fuel is faster than the flame propagation speed.

To investigate the fundamentals of ignition propagation and turbulent flame propagation under dual-fuel condition, preliminary simulation was performed in a planar mesh. By applying simple boundary and initial conditions, two simulations are investigated: the ignition propagation speed by well-arranged mixture fraction field and the ignition by injected liquid fuel and flame propagation from ignition points. These phenomena could be captured and the characteristics of combustion model in this study were investigated.

3.1 Flamelet Model Modifications

3.1.1 Boundary Conditions for the Dual-fuel Combustion

For the dual-fuel combustion, the boundary condition should be reset to reflect the first injected fuel and the second injected fuel. In this study, the second injected fuel is the representative fuel to express the mixture fraction. Furthermore, the first

injected lower reactivity fuel is assumed to be mixed and distributed well as oxygen and nitrogen not only in the mixture fraction field but also in the boundary condition where Z=0. Figure 3.1.1 shows the initial profiles of the first injected fuel, second injected fuel, oxygen and nitrogen of the conventional diffusion combustion and dual-fuel combustion conditions. The most distinguishing point between the ordinary diffusion combustion and the dual-fuel combustion is the species composition at the boundary. In the ordinary diffusion combustion, there is no chemical reaction at Z=0 because there is no fuel. However, in the case of dual-fuel combustion condition, the first injected lower reactivity fuel would be fully mixed during the compression stroke by the turbulent flow in the cylinder because the first injected fuel would be injected at the very early timing. Therefore, the first injected fuel is assumed to be fully mixed in the fresh air region. The mass fraction of the first injected fuel was determined by the injected mass and in-cylinder air mass. If temperature and pressure rise during the compression stroke, the first injected fuel and air at Z=0 as well as the second injected fuel and air at $0 < Z < 1$ could be ignited. At Z=1, the species composition at the dual-fuel condition is identical to the single-fuel condition.

From the different profiles of the species, the flame propagation speed from the ignition point to the lean region would be different in two different combustion conditions. Figures 3.1.2 and 3.1.3 show the flame propagation of the ordinary diffusion combustion and dual-fuel combustion with respect to the time. There are some discrepancies in two conditions. Ignition delay time is retarded in dual-fuel combustion because it makes richer fuel condition than the single-fuel condition. However, ignition propagation velocity to the lean mixture fraction is faster in the dual-fuel combustion condition than the single-fuel diffusion combustion condition. In the next chapter, this simple condition would be applied to the simple 3-D geometry.

3.1.2 Computational Setup

Figure 3.1.4 shows a planar mesh generated for preliminary simulation to simulate the modified flamelet model described in chapter 3.1.1. There is no spray because droplet breakup and evaporation processes of the injected fuel would be eliminated in this simple simulation. Therefore, fuel and air are mixed with no EGR condition at each cell. Size of domain was 221 mm in x-direction, 11 mm in y-direction and 1 mm in z-direction. The thickness of y is thin but the length of x-direction is very long because it covers all of the mixture fraction field with very small grid size. The mixture fraction step is 0.001 from Z=0 to Z=0.2 and 0.04 from Z=0.2 to Z=1.0. The reason why the mixture fraction unit from Z=0 to Z=0.2 is very small is because the ignition propagation from the second injected fuel to the mixed fuel region is important.

The boundary condition of Z-direction plain is symmetric condition and the other 4 walls are adiabatic. Initial temperature is 1,000 K and initial pressure is 40 bar. The conditional averaged scalar dissipation rate at stoichiometric mixture is fixed to 1 because it has no turbulent flow field due to no spray and no swirl condition. In the single-fuel condition, only n-heptane exists and there is no iso-octane. In the dual-fuel condition, n-heptane is identical to the single-fuel condition. However, iso-octane exists and the quantity is same to the equivalence ratio, 0.3. The mixture fraction is about 0.025 at Z=0 and 0.0 at Z=1. Figure 3.1.4 shows the initial mixture fraction distribution in this planar mesh. Each species are distributed followed by the mixture fraction.

3.1.3 Simulation Results

Figure 3.1.5 shows the ignition propagation from the ignition point to the lean region in single-fuel diffusion condition. Figure 3.1.6 shows the ignition propagation from the ignition point to the lean region in dual-fuel diffusion condition. As seen in these figures, the ignition propagation speed from ignition point to the lean region is different in two conditions.

In the single-fuel condition, temperature reached 1500 K after 0.33 ms from the simulation started at Z=0.1. Meanwhile, it takes 0.5 ms in the dual-fuel condition. However, the flame propagation speed is different at the two conditions. In the single-fuel condition, temperature reached to 1500 K at 0.36 ms for Z=0.08, 0.39 ms for Z=0.06, 0.48 ms for Z=0.04 and 0.80 ms for Z=0.02. It takes 0.47 ms from Z=0.10 to Z=0.02. We can define a new term, propagation rate to the Z direction, PRZ as

$$PRZ = (Z_1 - Z_2) / \text{time} \qquad (3.1.1)$$

Therefore, the PRZ in the single-fuel condition is about 170 /s. On the other hands, in the dual-fuel condition, temperature reached to 1500 K at 0.53 ms for Z=0.08, 0.56 ms for Z=0.06, 0.61 ms for Z=0.04, 0.73 ms for Z=0.02. Therefore, the PRZ is about 348 /s. It shows doubled quantity than that of single-fuel combustion. The differences of PRZ in the two cases are shown in Figure 3.1.7.

This simple simulation results have some limitations. The geometry is fixed and the initial temperature and pressure is constant. Therefore, the air mass is also fixed. The flamelet model needs mass fraction, not mass so the total fuel mass is different in two conditions. However, this simple simulation is enough to realize the difference of the ignition propagation speed at the non-premixed combustion in the single-fuel condition and dual-fuel condition.

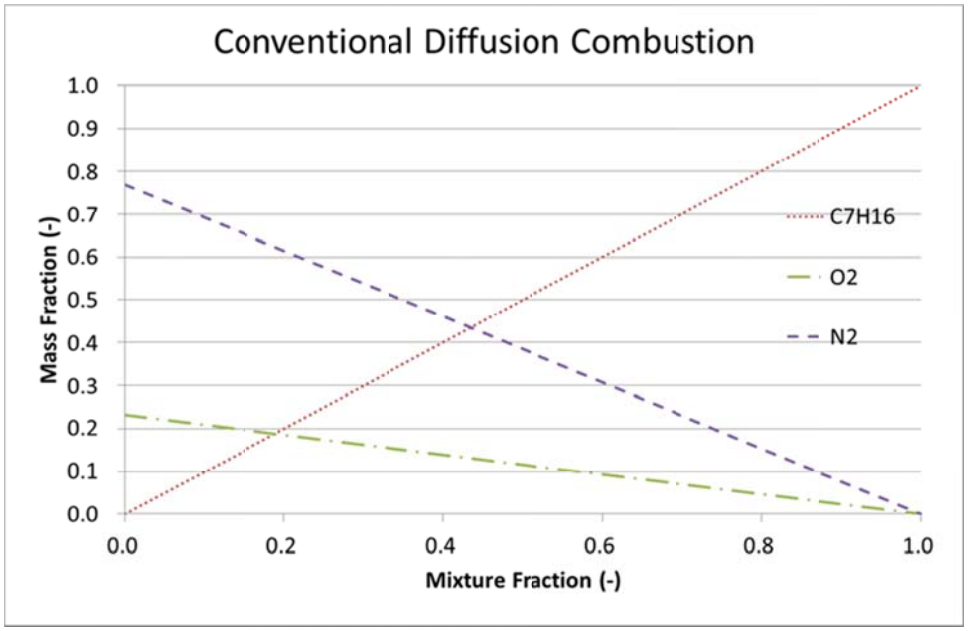

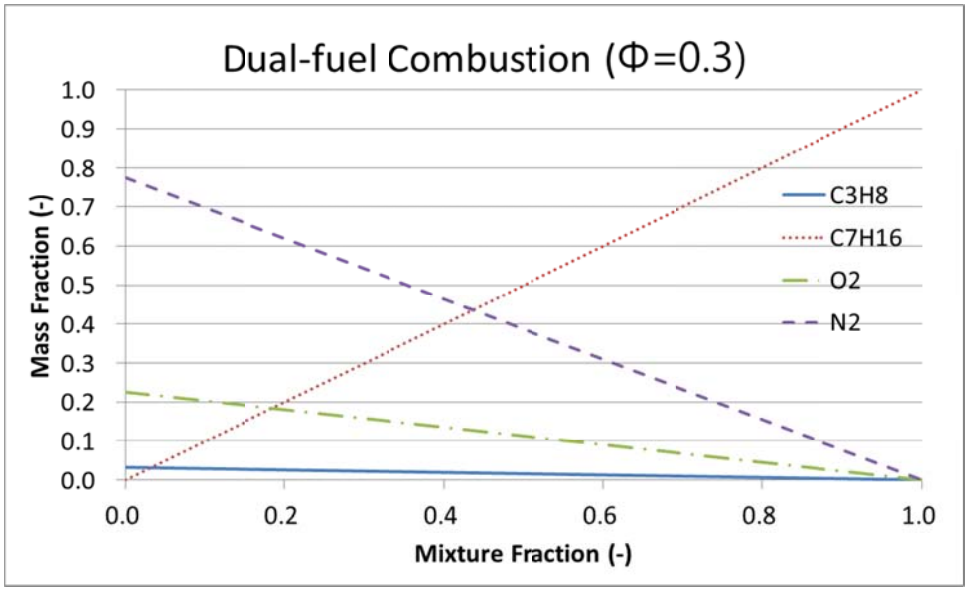

Figure 3.1.1 Initial species profiles with respect to the mixture fraction Z (conventional diffusion combustion: upper; dual-fuel combustion: lower)

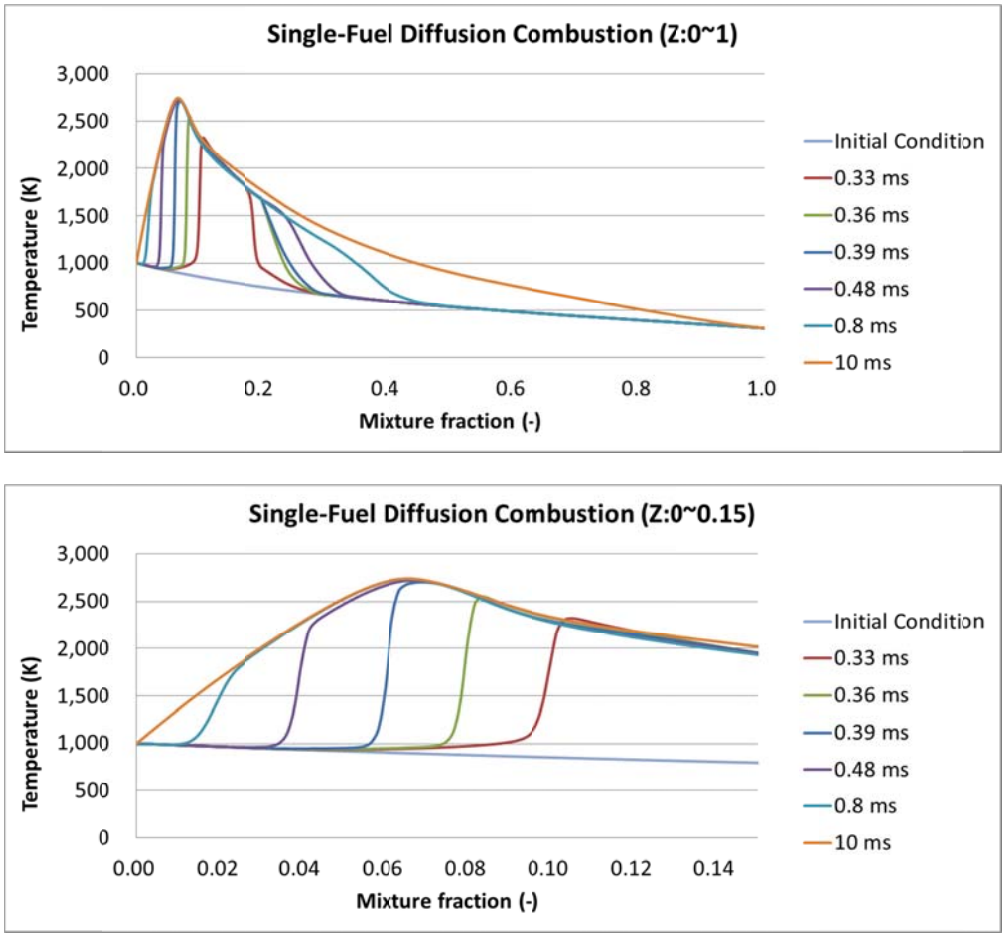

Figure 3.1.2 Changes of temperature profiles according to the time at the single-fuel (n-heptane) condition

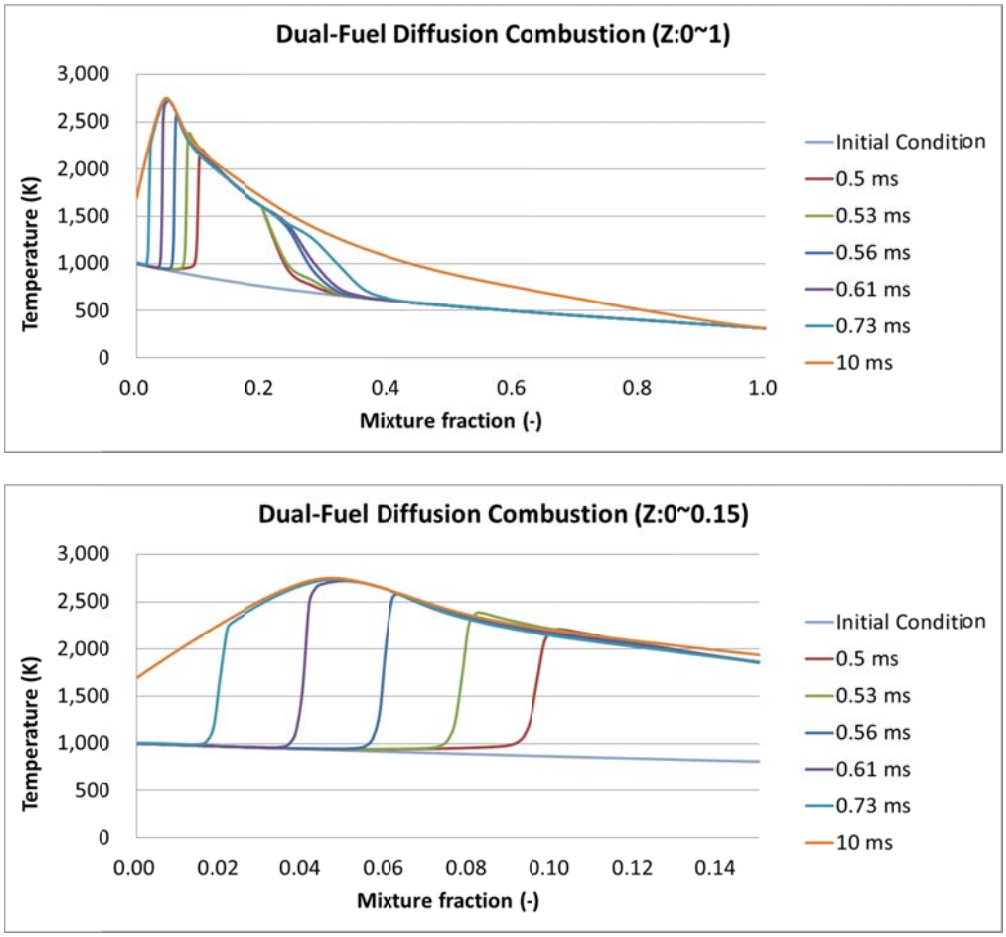

Figure 3.1.3 Changes of temperature profiles according to the time at the dual-fuel (n-heptane and iso-octane) condition

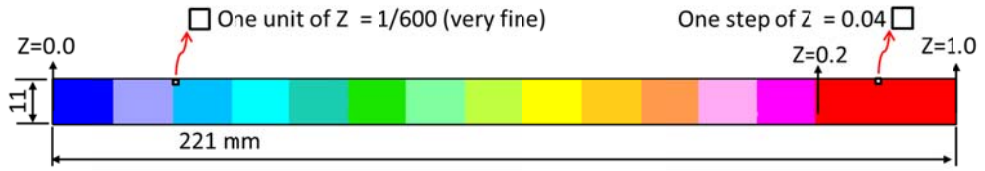

Figure 3.1.4 Initial distribution of mixture fraction in planar mesh.

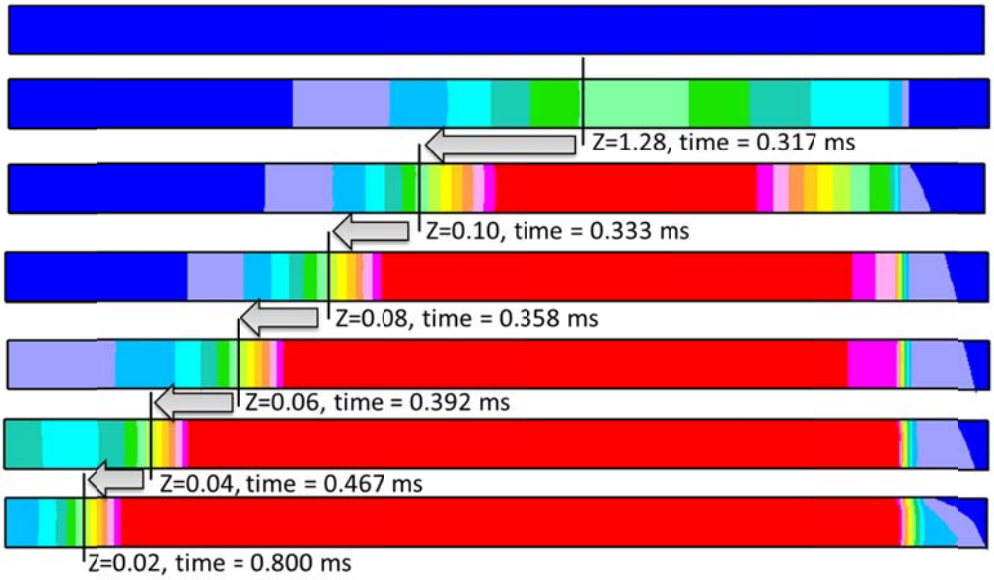

Figure 3.1.5 Ignition propagation to the lean mixture fraction in single-fuel combustion.

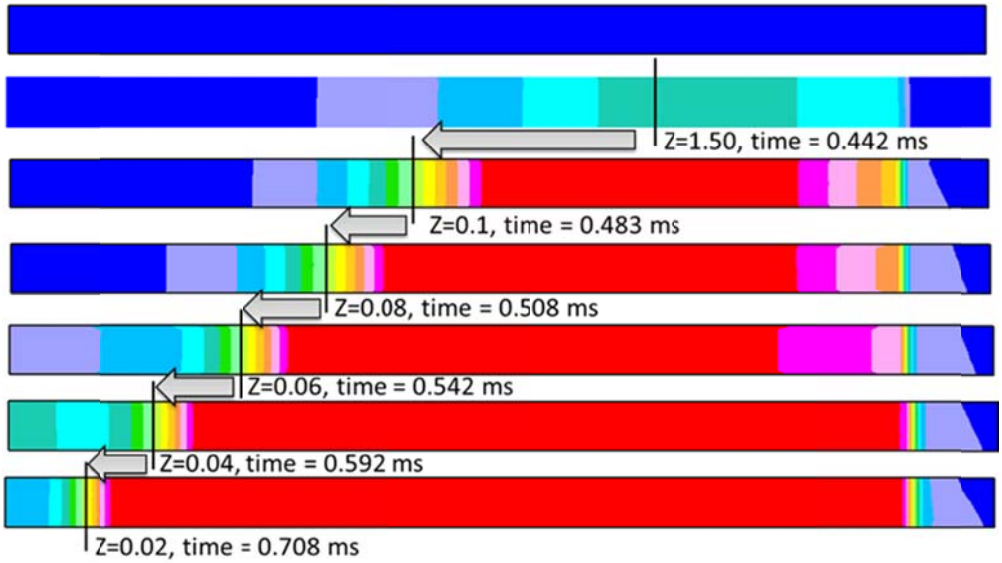

Figure 3.1.6 Ignition propagation to the lean and rich mixture fraction in dual-fuel combustion

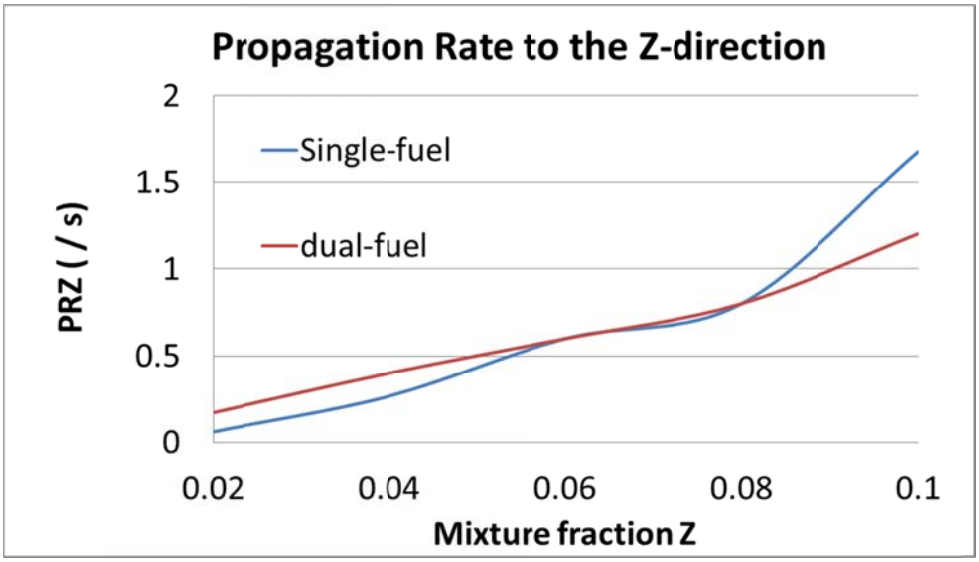

Figure 3.1.7 Propagation rate to the Z-direction in the single-fuel and dual-fuel cases.

3.2 Coupling flamelet model to the Level-set model

3.2.1 Level-set model for the Dual-fuel Combustion

To describe the conversion phenomenon of ignition propagation to flame propagation, laminar flamelet model was coupled with the level-set model. Laminar flamelet model solves the ignition from the higher reactivity fuel and ignition propagation from the ignition point. If the injection timing is very early, ignition points could be multiple. Laminar flamelet model is not only a kind of the ignition models but also a type of the combustion models, so it does not terminate after the ignition was started. Therefore, the laminar flamelet model is an adaptive model to the dual-fuel combustion model.

As documented in chapter 2.6, the level-set model started when the temperature of a cell is over 1,800 K. In a conventional level-set model used in SI engine, a minimum ignition volume should be generated before flame propagation. However, in this model, one cell (1 mm × 1 mm × 1 mm) could be an ignition source because flamelet model could not control the volume of flame sheet. Procedures after the ignition is identical to the ordinary level-set model in SI engine except the flamelet model works outside the flame sheet. Because another ignition sources could be generated from the higher reactivity fuels injected at the early timing.

3.2.2 Computational setup

A simple spray is applied to the simulation. Figure 3.2.1 shows the injection profile with respect to the time. Geometry used in this simulation is identical to the chapter 3.1.1. All the boundary conditions are set to symmetric condition because wall condition could affect the flame propagation behavior. Initial temperature and

pressure are very high enough to evaporate droplets instantaneously (1300 K and 41 bar).

3.2.3 Simulation results

Figure 3.2.2 shows the injection, ignition and flame propagation procedure in a simple simulation. After 0.56 ms from the SOI timing, ignition started from the higher reactivity fuel, n-heptane in this study. Ignition was occurred at vicinity of the stoichiometric surface of injected fuel as the conventional CI combustion and then level-set model is initiated when the temperature of the cell is over 1,800 K by the ignition. Due to the turbulence from the injection of fuel, flame propagates with some disturbances. That is, the turbulent burning velocity is affected by the turbulence flow field in the simple geometry induced by the fuel injection and ignition. However, the flame propagation is not affected just by the turbulent burning velocity. The ignition propagation speed affects the flame propagation speed also. The real flame propagation speed is determined by the competition between the turbulent burning velocity calculated by the level-set model and the ignition propagation speed calculated by the laminar flamelet model as documented in chapter 2.6. The turbulent burning velocity is seen at the Figure 3.2.3 which is the contour of G at each time step. The turbulent burning velocity could be represented as G because the moving speed of G is the turbulent burning velocity expressed in G-equation.

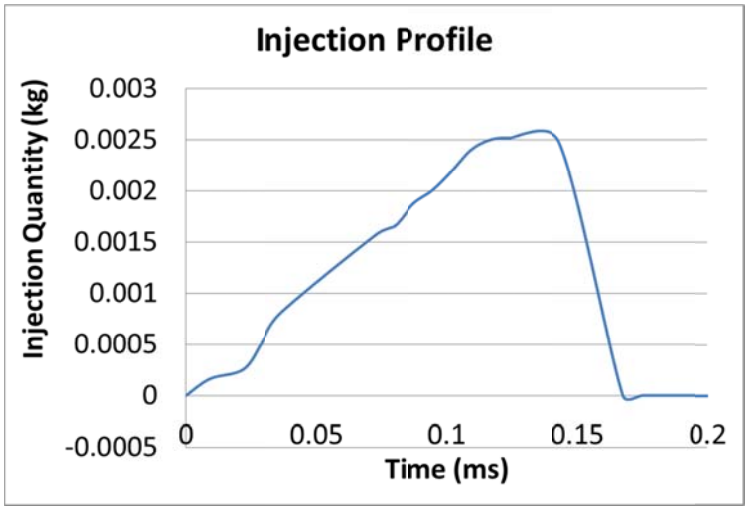

Figure 3.2.1 Injection profile used in the simple simulation.

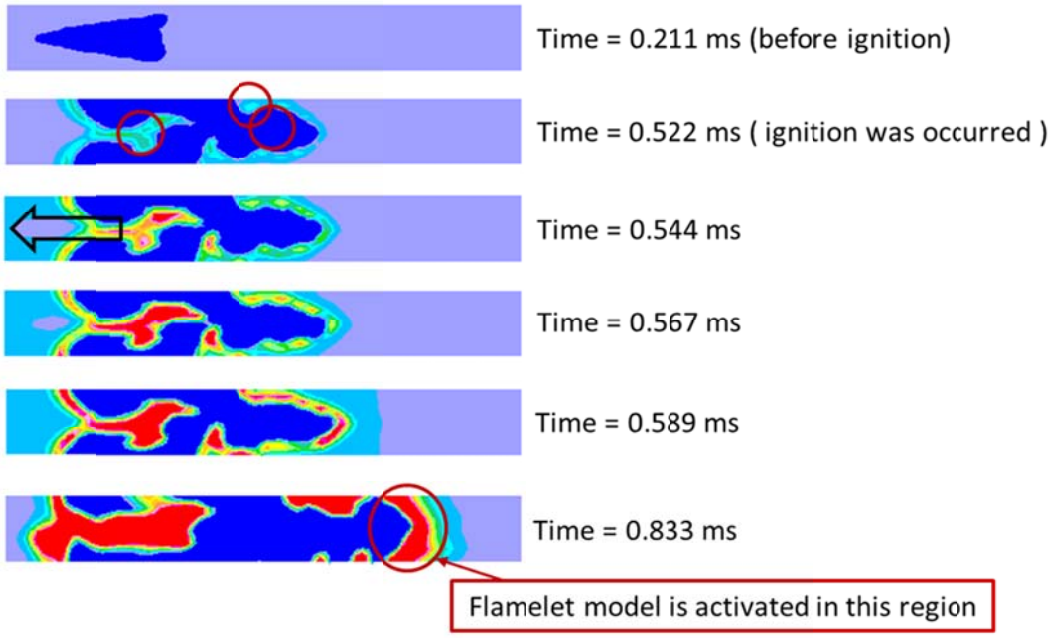

Figure 3.2.2 Injection, ignition and flame propagation from the ignition source using laminar flamelet model and level-set model

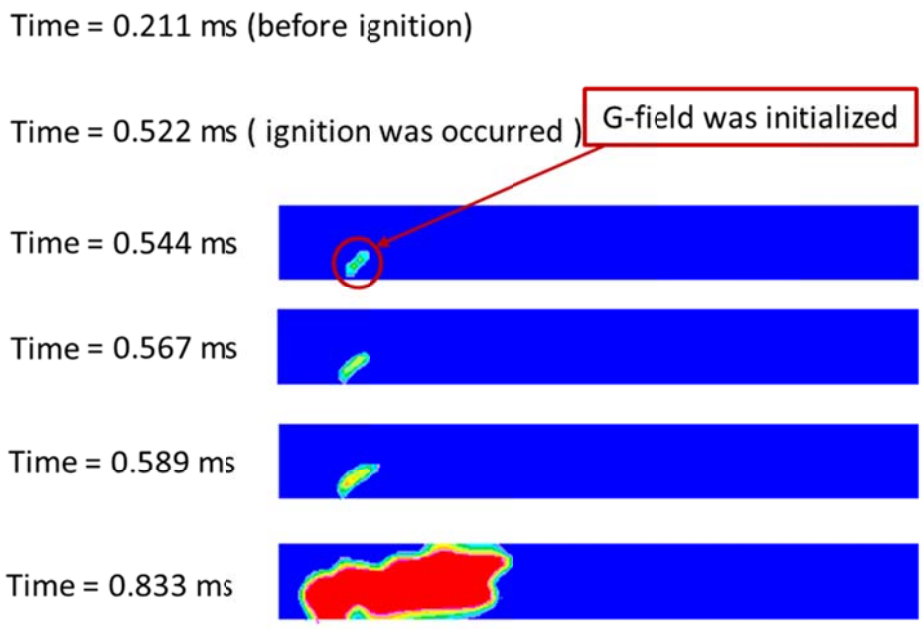

Figure 3.2.3. Contour of G in a simple simulation

Chapter 4. Simulation in an Engine Geometry

The combustion and emission behavior of conventional Diesel engine and dual-fuel combustion engine were investigated and compared experimentally. They showed decided differences in both aspects explicitly. The simulation model was applied to both conditions. The Diesel engine simulation results were used as validation conditions and the dual-fuel combustion model was applied to compare the results with the experimental data.

4.1 Experiments of dual-fuel combustion

4.1.1 Experimental setup

A high speed direct injection (HSDI) single cylinder Diesel engine based on EURO IV standard was used for experiments. A piezo injector which is able to spray up to 1600 bar was equipped with a common rail system. More detailed specifications of the engine are introduced in Table 4.1.1. To control the engine, a 37 kW DC dynamometer was adopted. The temperature of oil and coolant was controlled at near 80 ^{o}C. Also, fuel temperature was maintained at 40 ^{o}C during the experiments. To measure the rate of fuel flow, a mass burette type flow meter (ONO SOKKI, FX-203P) was used. The concentrations of NOx, THC, CO, CO2 and O2 were measured by using an exhaust gas analyzer (Horiba, MEXA 7100DEGR) and PM emission was measured using a smokemeter (AVL, 415S). Thus, EGR rate was calculated from the fractions of CO2 in the exhaust gas and intake gas. To simulate turbo charger and boosting intake-air, compressed shop-air was used. Then, to control the amount of air and maintain the constant flow, sonic orifices and pressure regulators were used. To measure pressures, an absolute pressure transducer (Kistler, 4045A5) was used and a relative pressure transducer

(Kistler, 6055Bsp) was adopted for in-cylinder pressure. Signals from the pressure transducers were recorded by the scale of one crank angle for 200 cycles and each case uses a data acquisition system.

The amount of propane gas was fumigated into intake port as gaseous state. The quantity of propane gas was measured by a flow meter (MK precision co., MFM (TSM-230)) for propane gas only. Also, to maintain the same propane gas rates during experiment periods, the flow rate was controlled using sonic orifices by producing choke flow. The configurations of experimental setup were depicted in Fig.4.1.1. Also, the properties of propane gas and Diesel fuel were listed in Table 4.1.2.

4.1.2 Calculation of Air-Fuel Ratio (AFR) for Dual-fuel Condition

The calculation of AFR was based on Spindt's equation [96]. The composition of a burned mixture of air and hydrocarbons reflects the AFR of the original intake mixture. AFR could be calculated by Spindt's equation that involves only fuel composition and exhaust emissions which are CO, THC, O2 and NOx emissions. The entire equations were introduced in Eq. 4.1.1 below

$$AFR = F_b[11.492 \times F_c\left(\frac{1+0.5R+Q}{1+R}\right) + \frac{120(1-F_c)}{3.5+R}] \quad (4.1.1)$$

$$F_b = \frac{P_{CO} + P_{CO}}{P_{CO} + P_{CO_2} + P_{CH}}, F_c = \frac{M_C}{M_C + M_H + \frac{C}{H}}, R = \frac{P_{CO}}{P_{CO_2}}, Q = \frac{P_{O_2}}{P_{CO_2}}$$

To calculate AFR of a dual fuel condition, it was essential to know the ratio of mass of carbon per hydrogen. Since conventional Diesel combustion used Diesel fuel only, the value of C/H was 1.8. However, AFR of a dual fuel condition was complicated to determine because two fuels were related during combustion.

For calculating AFR of dual fuel combustion, new C/H value was needed as various propane ratios for Diesel fuel. New C/H value was calculated by following procedures.

1) Check Diesel fuel weight at 50 % of low heating value (LHV) for the total fuel base.

2) Calculate propane gas weight at 50 % of LHV for the total fuel base.

3) Calculate the mole fraction and molecular weight of Diesel ($C_nH_{1.8n}$) and propane gas (C_3H_8).

4) Sum of each carbon mass and hydrogen mass and then calculate carbon mass per hydrogen mass.

4.1.3 Experimental results

There are two conditions, the first condition is pure Diesel CI combustion and the other is Diesel-propane dual-fuel combustion. CI combustion was used as an index of dual-fuel combustion condition. The fuel quantity of propane is determined by LHV. That is, the same LHV value is applied to both conditions. The LHV of Diesel is about 43.2 MJ and the LHV of propane is about 46.4 MJ. Therefore, the injection quantity of propane is less than that of Diesel about 93%. More detailed operating conditions are listed in Table 4.1.3. EGR was not applied to the experiments. Start of Diesel injection timing is set to equal, at BTDC 18 CAD.

Figure 4.1.2 shows the cylinder pressure w.r.t. the CAD in two cases. They show big difference in pressure curves. In the case A, Diesel fuel was injected about 7 times compared to CASE B and it could form powerful turbulence field. This could cause the ignition delay shorter than case B. In addition, the equivalence ratio of lower reactivity fuel of case B is not 1 but about 0.4. Therefore, the laminar flame speed is very low than that at the equivalence ratio is 1. It is the reason why these two cases show different pressure curves.

Due to the lean mixture fraction of case B, temperature is lower than that of case A. It induces much smaller quantity of NOx emissions. The early injection timing of lower reactivity fuel produces much smaller quantity of soot emissions as well. However, case B produces much greater amount of CO and THC than case A because of the slow laminar flame speed. Mixtures at the corner of the cylinder could not combust until the exhaust valve opens. The emissions in these experiments are summarized in Table 4.1.4.

Table 4.1.1 Specification of single-cylinder research engine

Specifications	Values
Displacement (cc)	497
Bore × Stroke (mm × mm)	83 × 92
Compression Ratio	15.5
Connecting rod length (mm)	145.8
HFR (cc/100 bar/30 s)	380
Spray angle (^{o})	153
Nozzle diameter (mm)	0.128
Number of nozzle holes	7

Table 4.1.2 Properties of propane gas and Diesel fuel

Properties	Diesel	Propane
Chemical formula	$C_xH_{1.8x}$	C_3H_8
Molecular weight (g)	190-220	44.1
Density (g/cm^3)	0.831	21.7
Low heating value (MJ/kg)	44	46.33
Auto-ignition temperature (K)	523	763
Stoichiometric ratio of AF (wt. %)	14.6	15.6

Table 4.1.3 Operating conditions of Diesel and Diesel-propane engine

Specifications	Case A	Case B
Fuel	Diesel 100%	Diesel 15%, Propane 85%
Engine speed (rpm)	1500	
BMEP (bar)	4	
AF	31	33.96
Intake Pressure (bar)	1.14	
EGR (%)	0	

Table 4.1.4 Emissions of Diesel and Diesel-propane engine

Specifications	Case A	Case B
NOx (ppm)	2833	231
PM (FSN)	1.052	0.127
CO (ppm)	356	1816
THC (ppm)	607	4860

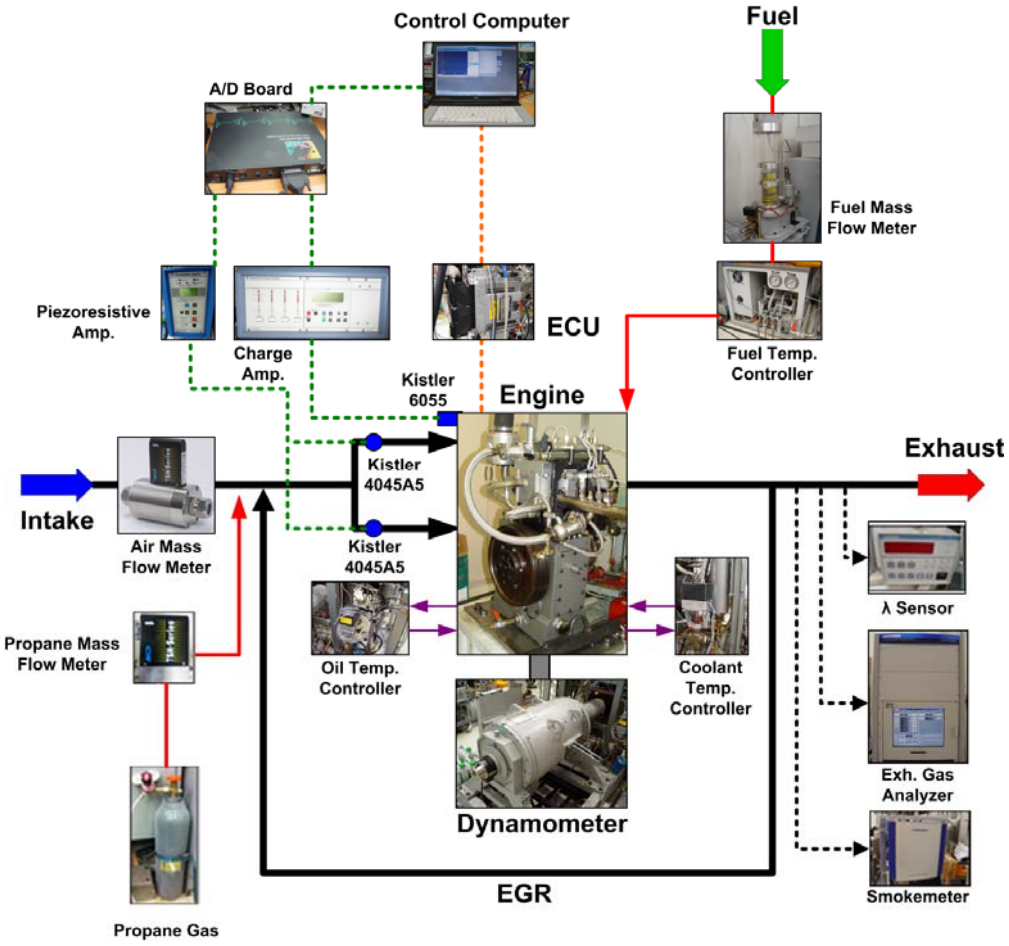

Figure 4.1.1 Experimental apparatus of experimental setup

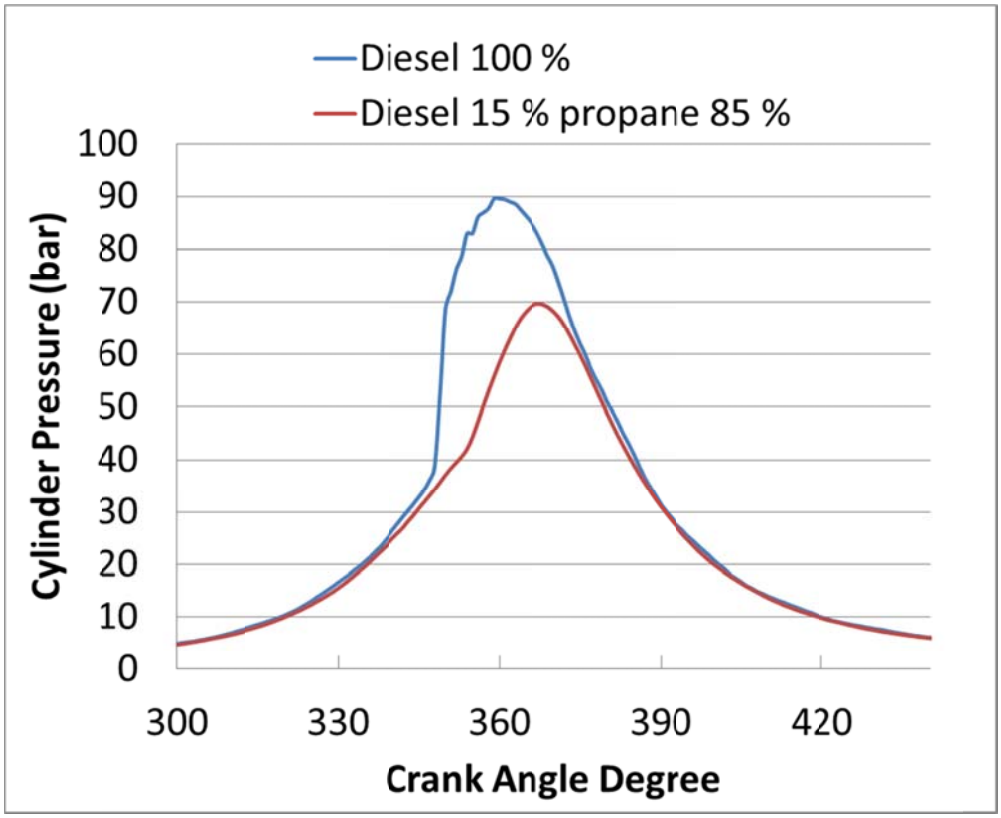

Figure 4.1.2. Comparison of cylinder pressure between Diesel combustion and Diesel-propane dual-fuel combustion at 1,500 rpm and 1.04 bar intake pressure.

4.2 Computational setup

4.2.1 Numerical modeling of practical dual-fuel engine

Figure 4.2.1 shows computational mesh of a practical dual-fuel engine generated for three-dimensional CFD simulation. The computational mesh, consisting of approximately 53,000 cells at BDC and 17,000 cells at TDC, represented 1/7th of the entire combustion chamber since the Diesel engine geometry is symmetric. The mesh density was similar to the previous work [97]. Refined meshes were applied near the wall in order to consider the heat loss from the piston and the cylinder liner. General specifications of the engine are listed in Table 4.1.1.

For the boundary conditions, standard wall with non-slip condition was applied to all of solid walls in the engine combustion chamber while cyclic boundaries are applied to the side of cylinder. The wall temperatures used in this study are listed in Table 4.2.1 and other numerical setups were identical to the preliminary simulations.

4.2.2 Calculation conditions

The calculation conditions for the combustion simulation of conventional Diesel engine and dual-fuel combustion engine were listed in Table 4.1.3.

General governing equations of flow field were solved by a commercial CFD code, STAR-CD. Furthermore, the turbulent mean reactions rates of scalars were calculated by the combustion and emission model developed in this study. Other numerical setups are summarized in Table 4.2.2. To verify the real compression

ratio of the research engine, in-cylinder pressure operated by the dynamometer only is compared to the simulated pressure data with no combustion model.

Table 4.2.1 Temperature of solid walls in engine combustion chamber

Region	Temperature (K)
Cylinder Wall	400
Engine Head	450
Piston Top Surface	450

Table 4.2.2 Numerical models and schemes for numerical simulation

Item	Modeling
Equation of state	Ideal f(T,P)
Molecular viscosity	Multi-component Model
Conductivity	Multi-component Model
Temporal discretization	Implicit Scheme
Spatial discretization	MARS Scheme
Transient Calculation Algorithm	k-ε / RNG

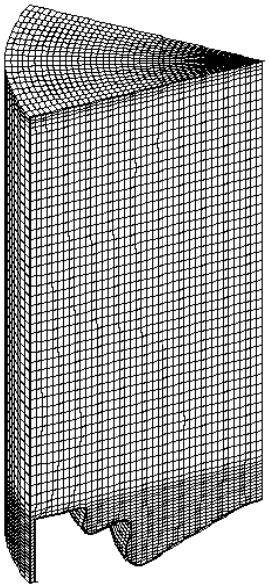

Figure 4.2.1 Three-dimensional computational mesh of a practical dual-fuel engine

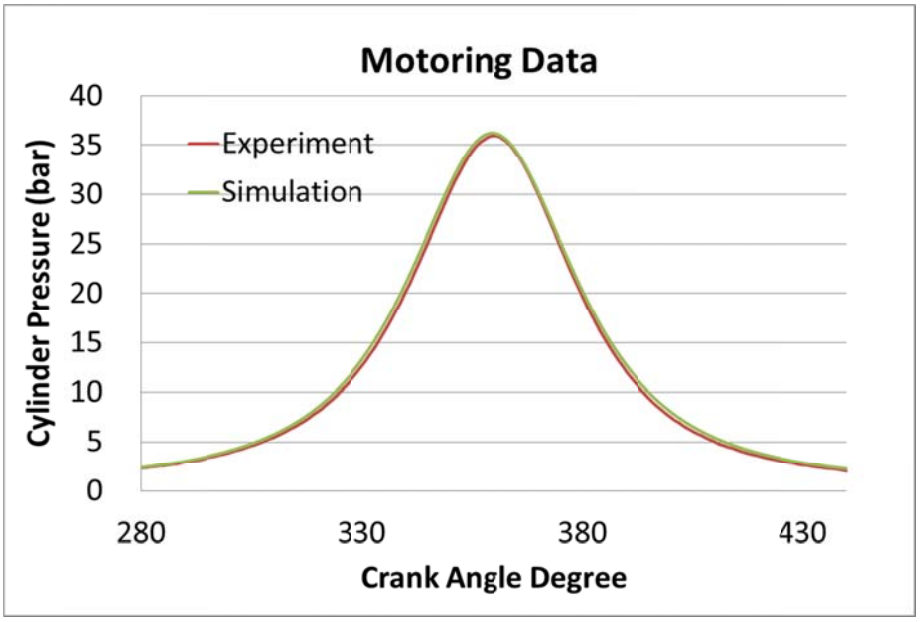

Figure 4.2.2 Motoring data from the experiment and simulation

4.3 Simulation results

4.3.1 Comparison with experimental results

The simulation results of combustion and emissions for cases A and B in Table 4.1.2. were compared with the experimental data. Figures 4.3.1 and 4.3.2 show the comparison of cylinder pressure between experimentally measured data and engine simulation results. Case 1 is calculated by RIF model only because it only uses diffusion flame. Case 2 uses dual-fuel combustion model and it showed very good agreement with the experimental results.

Figures 4.3.3 - 4.3.5 show the comparison of emission index in terms of NOx, soot number density (SND) and THC for case B. In dual-fuel combustion, NOx and soot are decreased compared to the CI combustion. On the other hand, CO and THC are increased. In three-dimensional CFD simulation, these trends are well captured by the dual-fuel combustion and emission models in this study. More details are followed at the next chapters.

Figure 4.3.7 shows temperature development of the conventional Diesel combustion (left) and classical dual-fuel combustion (right) by the in-cylinder section view. The ignition is occurred earlier for the Diesel combustion than dual-fuel combustion. After 6.7 CAD from the SOI timing (2 CAD is the mechanical injection delay time), maximum temperature was over 1,500 K in the case of Diesel combustion. In addition, the combustion duration is shorter for the Diesel combustion than dual-fuel combustion. Combustion was propagated to the almost all in-cylinder region within about 2~3 CAD. In the case of dual-fuel combustion, not only the ignition timing is retarded but the flame propagation speed is also slower. After 9.4 CAD from the SOI timing, maximum temperature was over 1,500 K in the case of dual-fuel combustion due to the small quantity of Diesel fuel and the rich region from the propane gas. Combustion had not reached to the in-cylinder wall even after 6.6 CAD from the ignition timing for the dual-fuel

combustion case because the ignition propagation speed and the turbulent burning velocity are both slower than the diffusion flame speed. Also, the temperature combustion is much lower for the dual-fuel combustion. Figure 4.3.8 shows the comparison of heat release rates between the Diesel combustion and dual-fuel combustion conditions. As mentioned before, the ignition timing for the Diesel combustion is earlier than the dual-fuel combustion and the combustion duration is shorter for the Diesel combustion.

4.3.2 Simulation of ignition and flame propagation process

After 11.5 CAD from the SOI timing of the higher reactivity fuel, the ignition was occurred at the vicinity of stoichiometric region of the flamelet for the case B. At the start of ignition, the combustion propagated not by the turbulent burning velocity but by the ignition propagation speed from the flamelet model. Figure 4.3.9 shows the temperature and scalar G distributions of case B at 6.5, 5 and 1^{o} BTDC. At 6.5^{o} BTDC, ignition was occurred at the vicinity of the higher reactivity fuel spray. At that time, distribution of the scalar G was initiated by the level-set model and scalar G propagates to the unburned region. At 6^{o} BTDC, two G-sphere met and they are combined into one.

Up until the ignition propagation speed of the higher and lower reactivity fuels is slower than the turbulent burning velocity of the premixed lower reactivity fuel, ignition propagation speed by the flamelet model is the dominant flame propagation speed of the dual-fuel engine. It seems that the mass fraction of the higher reactivity fuel is very small, and then the ignition propagation speed is decreased. This phenomenon was seen at Chapter 3. This trend holds out until the non-premixed combustion from the higher reactivity fuel is terminated.

Figure 4.3.6 shows the mass fraction of the lower reactivity fuel, propane. As shown in this figure, a part of propane is mixed to the higher reactivity fuel, n-heptane, and consumed with the n-heptane.

4.3.3 Simulation of pollutant formation process

As seen in Figures 4.3.3 - 4.3.5, the emissions of dual-fuel engine are well described by the emission models in this study. The contours of NO mass fraction and soot number density at 6.5, 5 and 1 ^{o} BTDC are shown in Figure 4.3.10. At the SOC timing, the NO emission is generated at the flame regions. However, the combustion phase is changed from the non-premixed combustion to the premixed combustion and hence the NO emission is generated from the burned region which is produced by the premixed combustion in the cylinder. Therefore, the region which has rich NO emission is widened. However, the produced NO emission quantity is small due to the low combustion temperature.

On the other hand, production of soot emission is dominated by the local equivalence ratio of the in-cylinder fuel. Therefore, the dual-fuel combustion produces smaller amount of soot emission than the conventional Diesel engine because the lower reactivity fuel is well mixed to the air by the early injection timing and the equivalence ratio is also smaller. In these figures, the soot production is activated at the center of the spray at 6 ^{o} BTDC because this region is rich at the SOC timing. However, the soot emission is produced at the burned region when the premixed combustion is activated.

Basically, dual-fuel combustion injects the lower reactivity fuel at the very early timing, so the fuel exists at the crevice volume. If the premixed combustion is not reached to the crevice volume until the exhaust valve open timing, this fuel is emitted out of the cylinder. Therefore, dual-fuel combustion produces very much THC emission compared to the conventional CI engine.

4.3.4 Effects of Operating Conditions

4.3.4.1 Swing of the injection timings

Numerical approach in internal combustion engine research takes advantages of easy modification of the engine. In this study, the injection timing of the higher reactivity fuel was modified. The injection timing of the second fuel at Chapter 4.3.2. was 18 ^{o} BTDC. Therefore, the injection timing was modified from +10 ^{o} to -10 ^{o} to verify the effect of injection timing in dual-fuel combustion engine. So, the cases are 28 ^{o} BTDC (case C), 18 ^{o} BTDC (case B) and 8 ^{o} BTDC (case D).

Figure 4.3.11 shows the pressure comparison among the case B, C and D. Whereas the case B and D are the classical dual-fuel combustion, case C is a kind of RCCI combustion. In the case of B and D, ignition was occurred during the injection duration. While in the case of C, due to the early injection timing, ignition has not occurred until the end of injection duration and ignition was occurred at the latest among all the cases. This combustion behavior coincides with the PCCI combustion behavior.

Figure 4.3.12 shows the comparison of heat release rates between the classical dual-fuel combustion and RCCI combustion conditions. This figure seems to show the evidence of the PCCI combustion. Ignition timing is definitely retarded for the RCCI combustion condition than classical dual-fuel combustion condition. Also, for the RCCI combustion, the heat release rate curve is narrower and higher than the classical dual-fuel combustion condition. However this is not the perfect evidence. Therefore additional in-cylinder view should be provided to verify the RCCI combustion. Figure 4.3.13 shows the temperature development of the RCCI combustion by the in-cylinder section view. The ignition is occurred after 20 ^{o} CA from the SOI timing of higher reactivity fuel and even after the TDC. Also, the ignition sources are generated all in-cylinder region from the mixed fuel of the higher and lower reactivity fuels. The mixed fuel is ignited and the ignition was propagated most of the in-cylinder region. This phenomenon shows that the combustion behavior seems to be similar to the PCCI combustion.

Figure 4.3.14 shows the comparison of NOx emissions among the case B, C and D. Figure 4.3.15 shows the comparison of soot emissions among the case B, C and D. From the PCCI combustion, case C showed the least NOx emission and soot emission production among them. In the case of soot number density, the

production rate is the smallest in case C. However, in the case of soot, the RCCI combustion showed the worst oxidation rate.

4.3.4.2 Swing of the EGR rates

EGR rate was changed to investigate the effect of EGR rates in dual-fuel combustion. The EGR rate of the basic condition (case B) was 0%. In this chapter, EGR rates were varied from 20% to 40%.

Figure 4.3.16 shows the pressure comparison among the cases of EGR 0%, 20% and 40%. As more EGR is applied, ignition delay time is retarded and the peak pressure is lowered. Generally, the ignition timing is delayed when EGR is applied. In this study, as EGR rates are increased, ignition timing was delayed. Especially, ignition was occurred after the end of injection duration for the case of EGR 20% and 40%. It shows that the possibility of RCCI combustion without modifying the injection timing of the higher reactivity fuel and as EGR rates are increased, the possibility of RCCI combustion is also increased. It shows the possibility of RCCI combustion using applying EGR. If optimized EGR rate and injection timing are applied to the dual-fuel combustion engine, RCCI can be achieved without applying excessively advanced injection timing.

Figure 4.3.17 shows the comparison of NOx emissions among the cases of EGR 0%, 20% and 40% and figure 4.3.18 shows the comparison of soot emissions among the cases of EGR 0%, 20% and 40%. As EGR rates are increased, combustion temperatures of the dual-fuel combustion engine are lowered and ignition delay time is getting closed to the TDC. Thus, the NOx emissions are also decreased. In the case of soot emission, the emissions are almost the same level in all cases. Soot production rate for the EGR 20% case is the highest among the all cases due to applying EGR. However, the soot production rate for the EGR 40% case is the lowest among the all cases. It seems that the possibility of PCCI combustion for the EGR 40% case.

4.3.4.3 High load condition

The mass of the propane gas was added to investigate the effect of the load in dual-fuel combustion. The propane mass of the basic condition was about 14 mg. The AF ratio and BMEP corresponding to the basic condition is about 34 and 4 bar, respectively. In this chapter, the mass of the propane gas was increased by 50% (about 21 mg).

Figure 4.3.19 shows the pressure comparison between the cases of propane mass 100% and 150%. As more propane is applied, ignition delay time is retarded due to the specific heat constant of the propane. However, peak pressure increases because the fuel mass is increased.

Figure 4.3.20 shows the comparison of NOx emissions between the cases of propane mass 100% and 150% and figure 4.3.21 shows the comparison of soot emissions between the cases of propane mass 100% and 150%. As the mass of propane gas is increased, combustion temperatures of the dual-fuel combustion engine are getting raised because the equivalence ratio of the fuel approaches to 1. Thus, the NOx emissions are also increased although the ignition delay time is delayed . In the case soot, the oxidation rate is lower for the high load condition than the low load condition. Therefore, the resultant soot emission is larger for the high load condition.

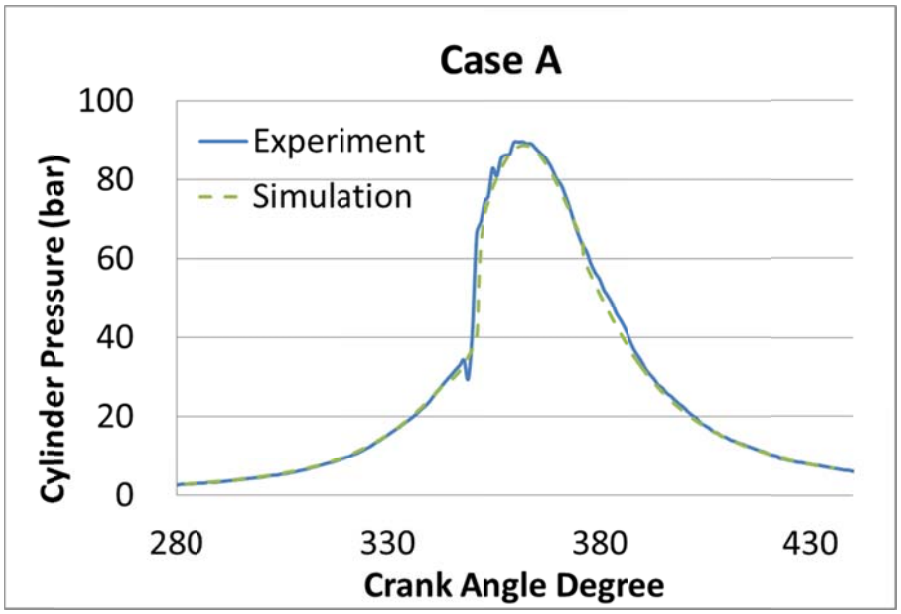

Figure 4.3.1. Comparison of cylinder pressure between experimental data and simulation result at 1500 rpm and 1.14 bar intake pressure (Case 1)

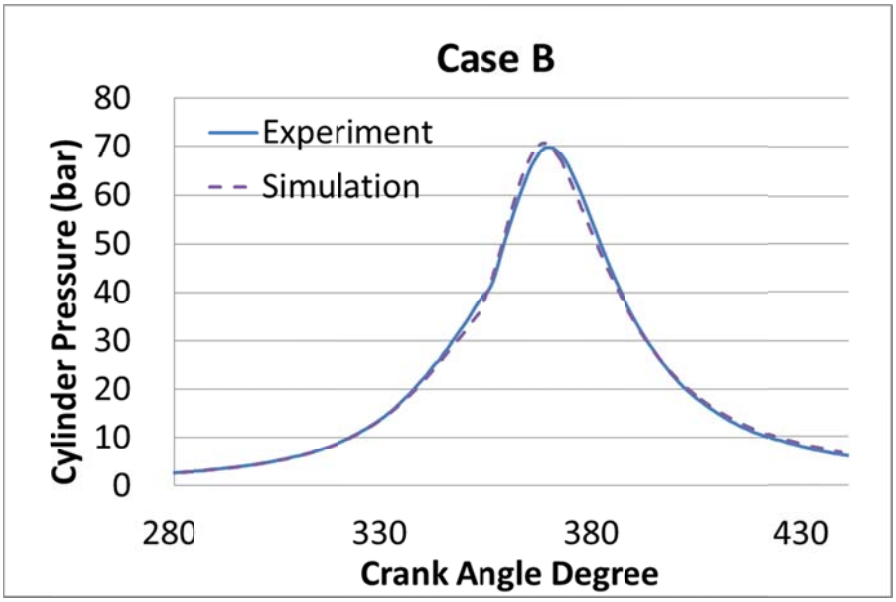

Figure 4.3.2. Comparison of cylinder pressure between experimental data and simulation result at 1500 rpm and 1.14 bar intake pressure (Case 2)

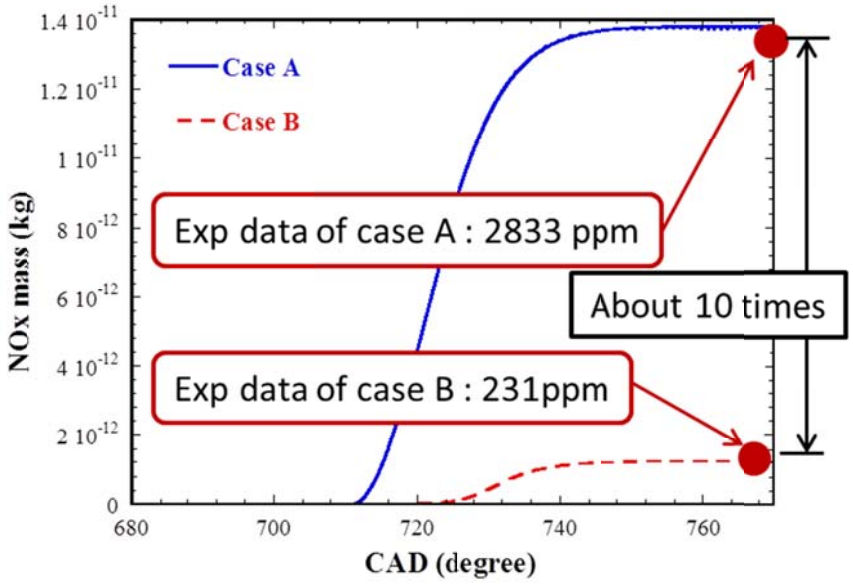

Figure 4.3.3 Comparison of NOx emissions for the case A and B according to the crank angle degree.

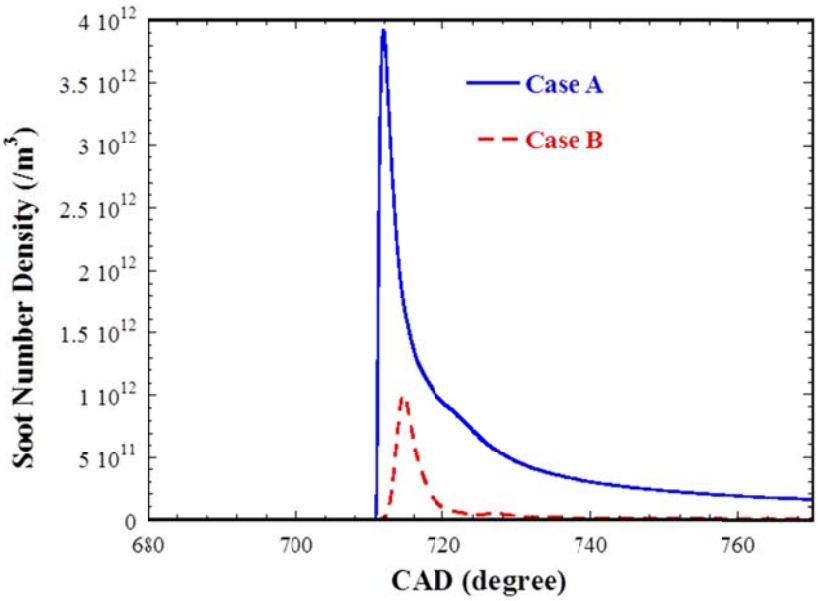

Figure 4.3.4 Comparison of soot number density for the case A and B according to the crank angle degree

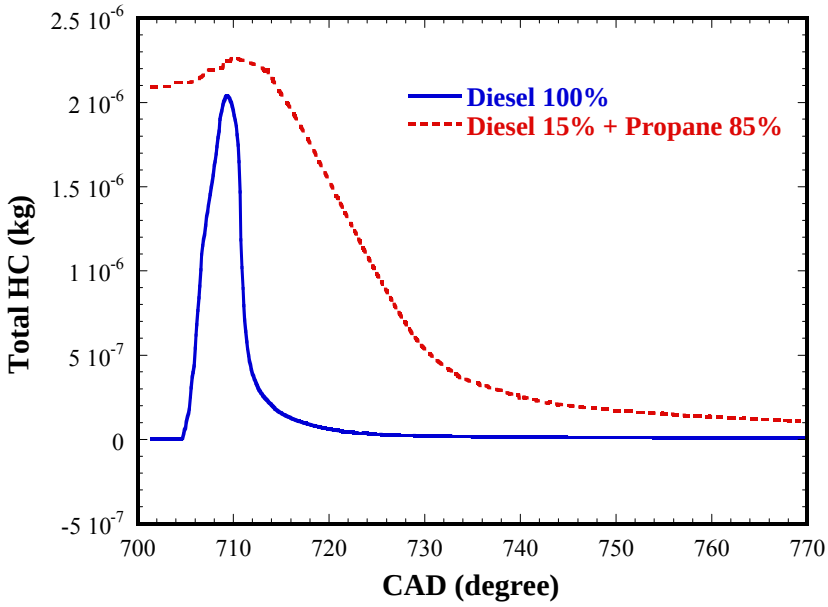

Figure 4.3.5 Comparison of total hydrocarbon for the case A and B according to the crank angle degree

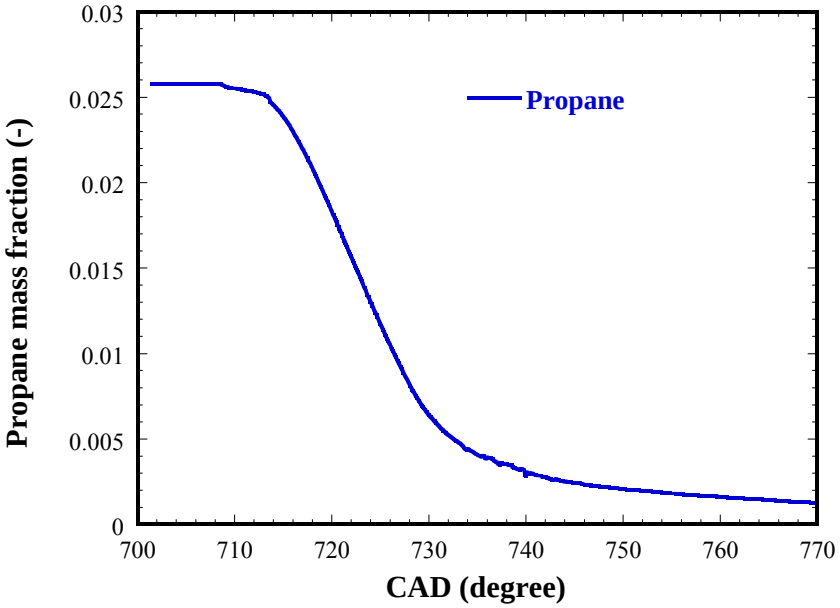

Figure 4.3.6 mass fraction of the propane in dual-fuel combustion

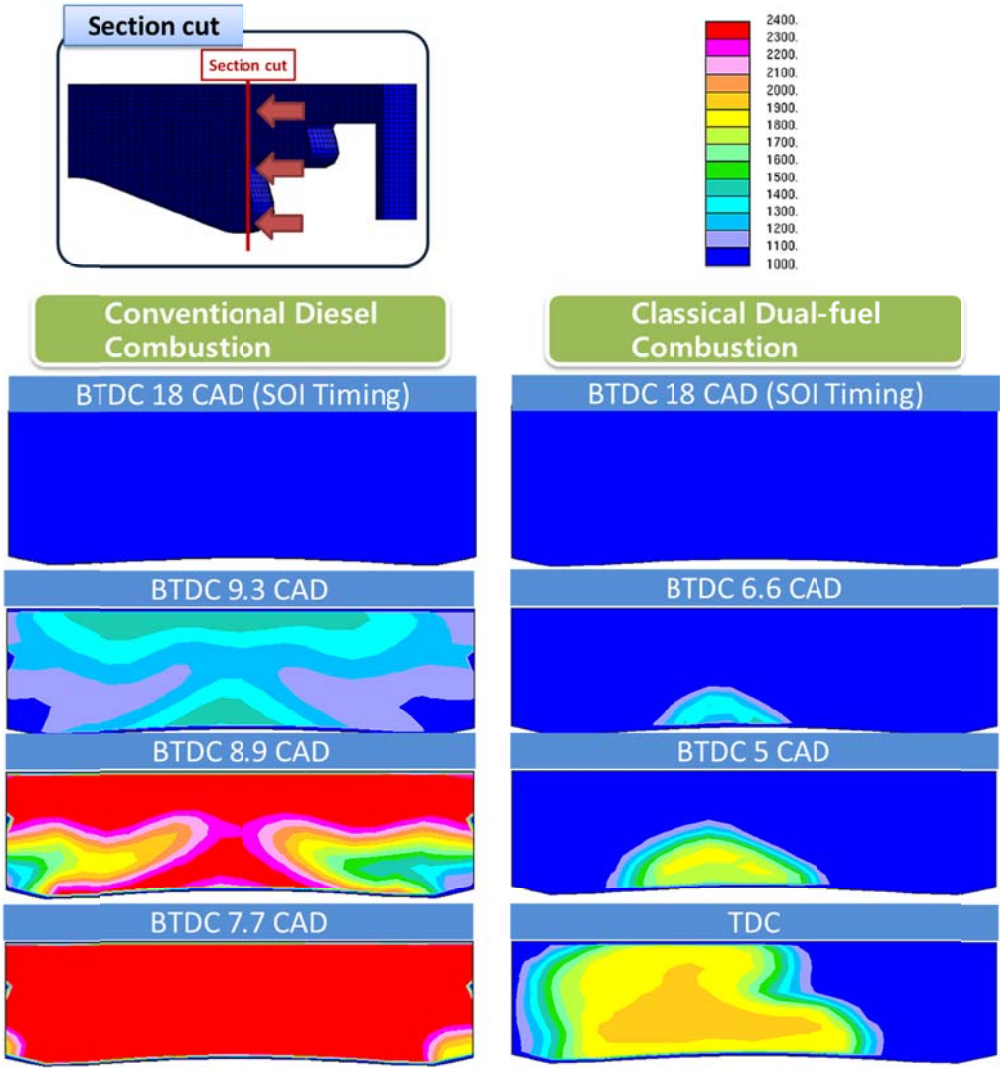

Figure 4.3.7 Temperature development of the conventional Diesel combustion(left) and classical dual-fuel combustion(right) from the in-cylinder section view

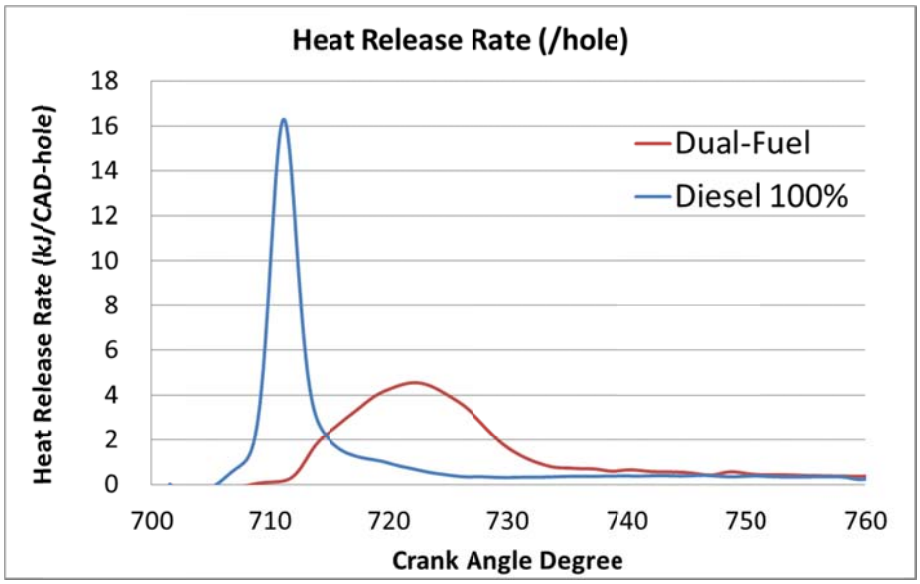

Figure 4.3.8 Comparison of heat release rates between Diesel combustion and dual-fuel combustion conditions.

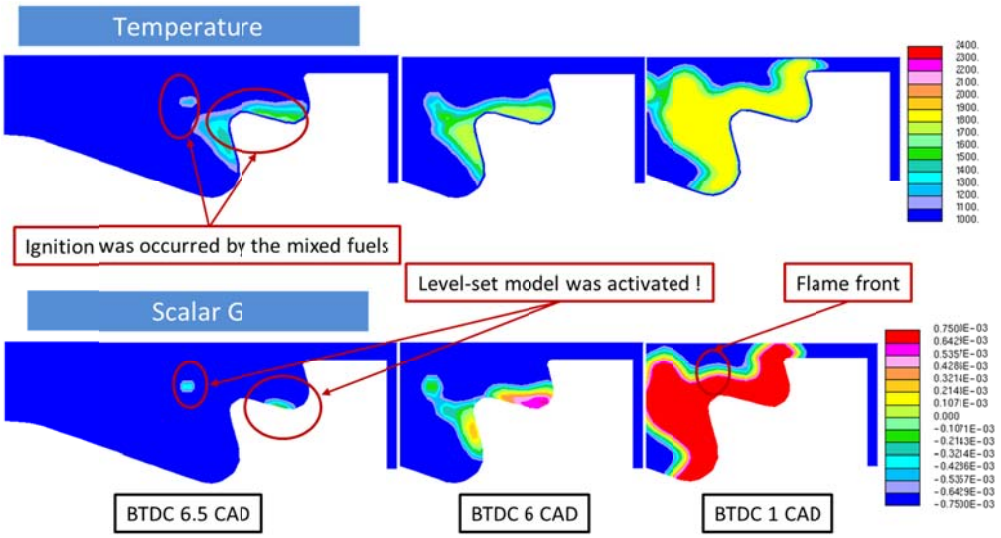

Figure 4.3.9 Temperature and scalar G distributions of case B

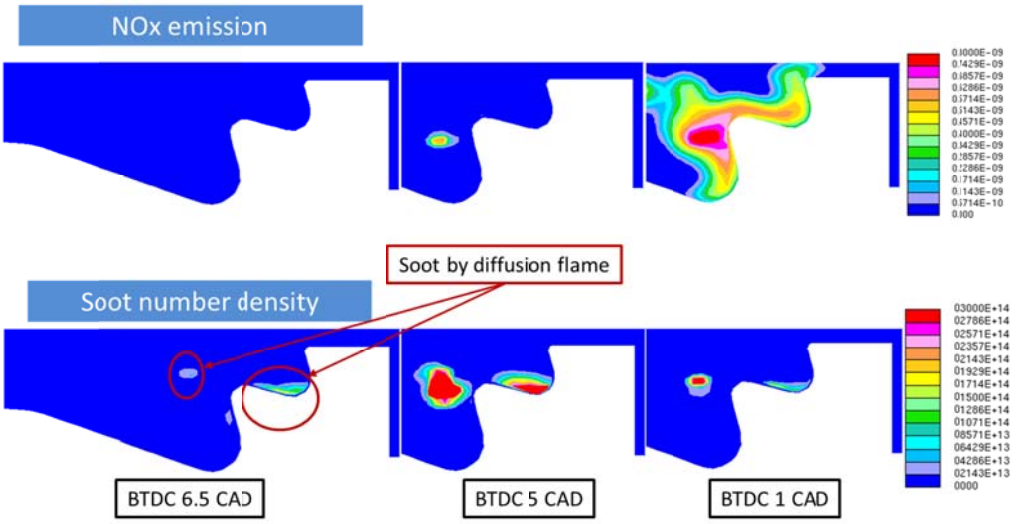

Figure 4.3.10 NO mass fraction and soot number density contour of case B

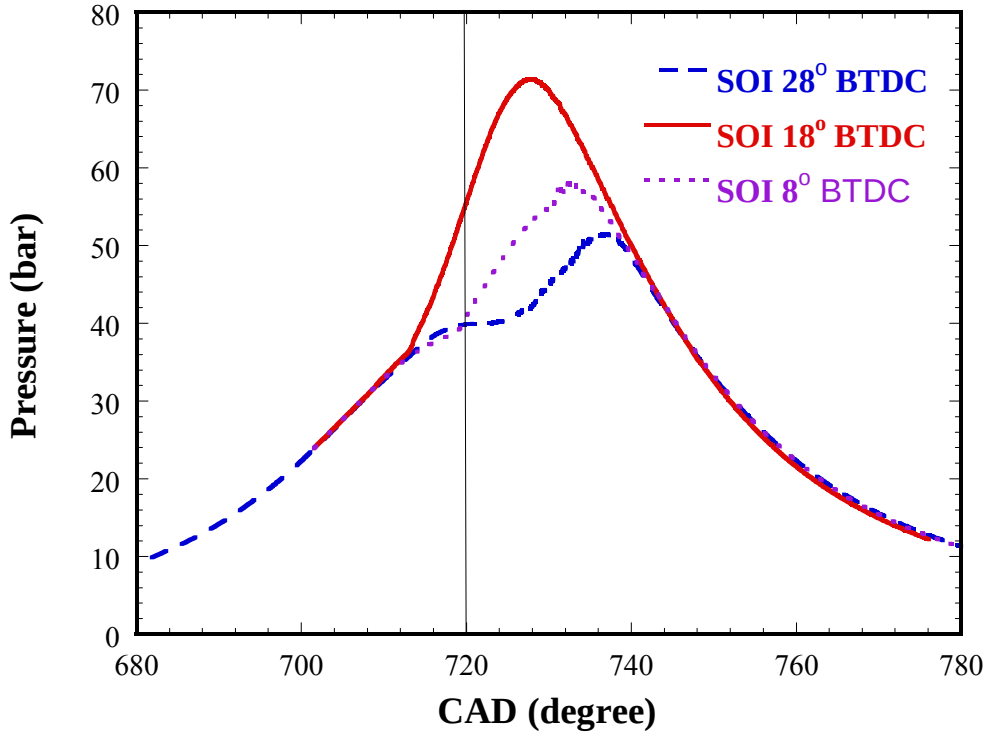

Figure 4.3.11. Pressure comparison among case A, B and C according to the crank angle degree

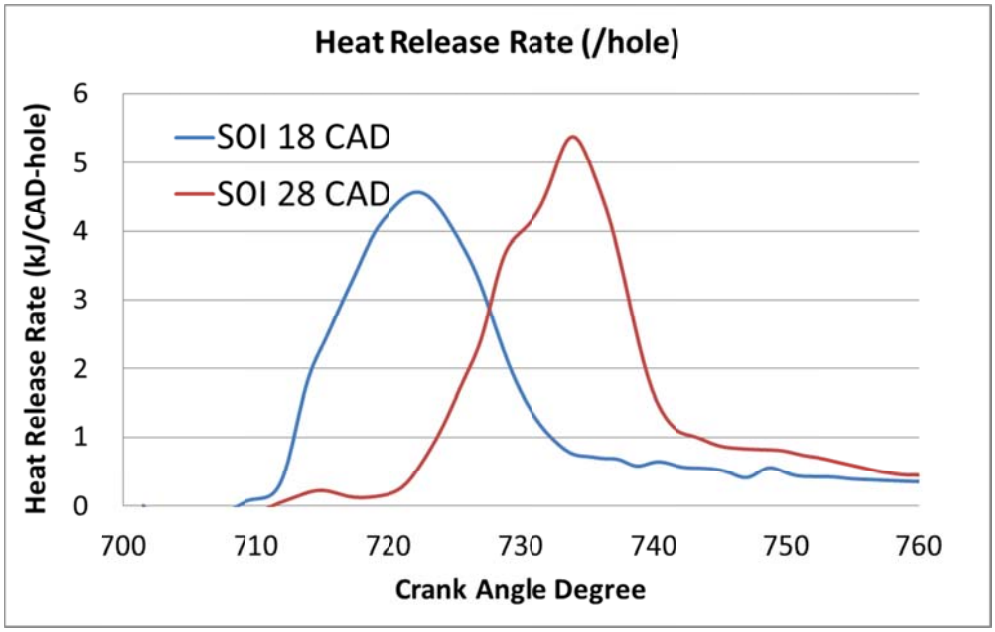

Figure 4.3.12 Comparison of heat release rates between classical dual-fuel combustion and RCCI combustion conditions.

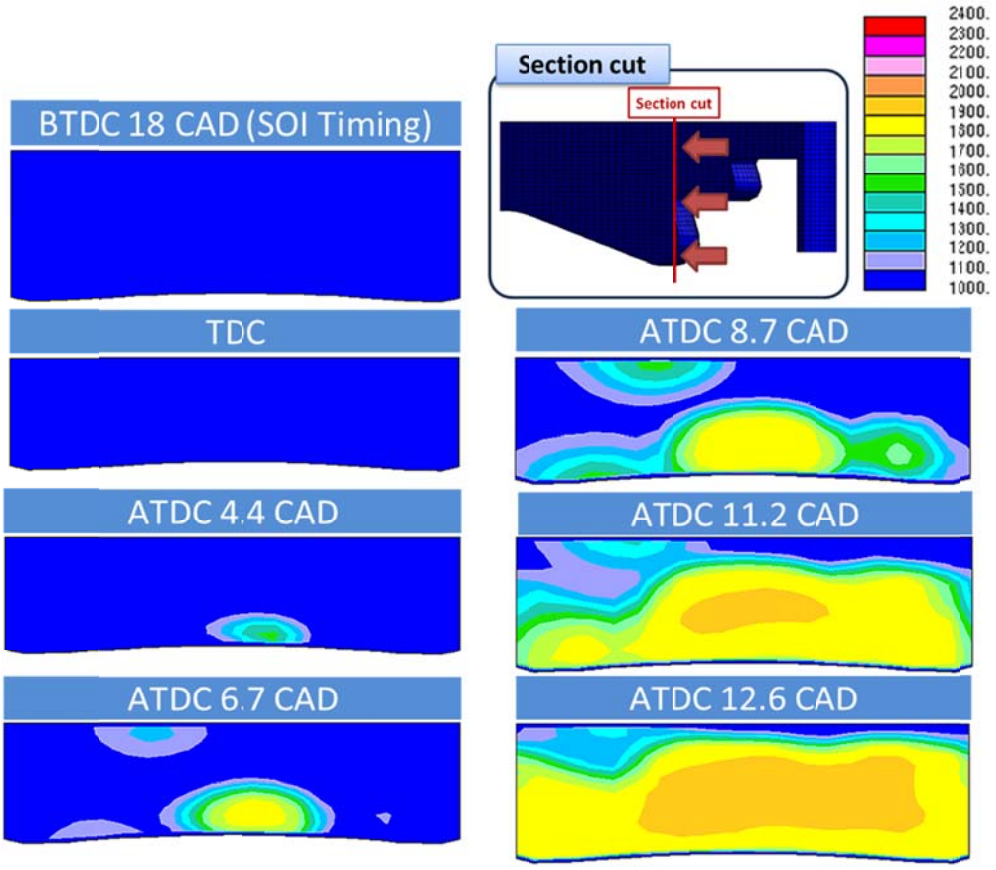

Figure 4.3.13 Temperature development of RCCI combustion from the in-cylinder section view

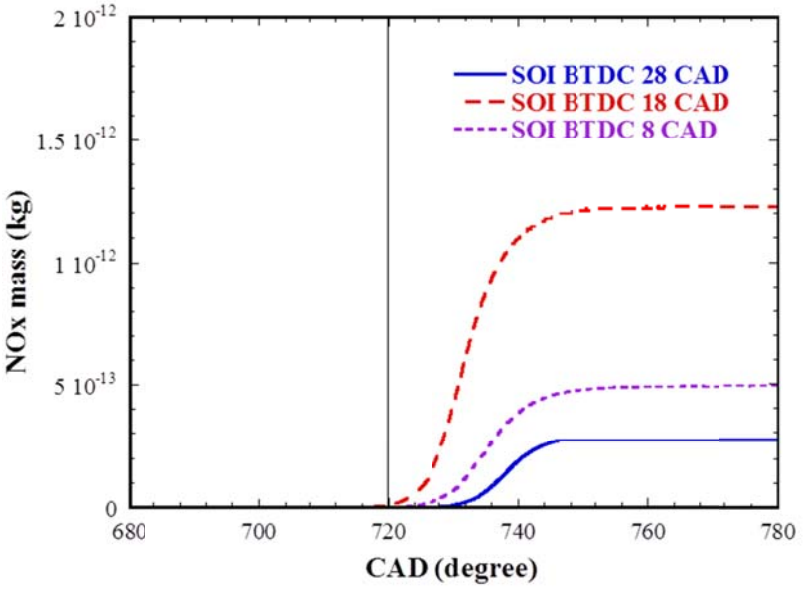

Figure 4.3.14 NOx emissions comparison among case A, B and C according to the crank angle degree

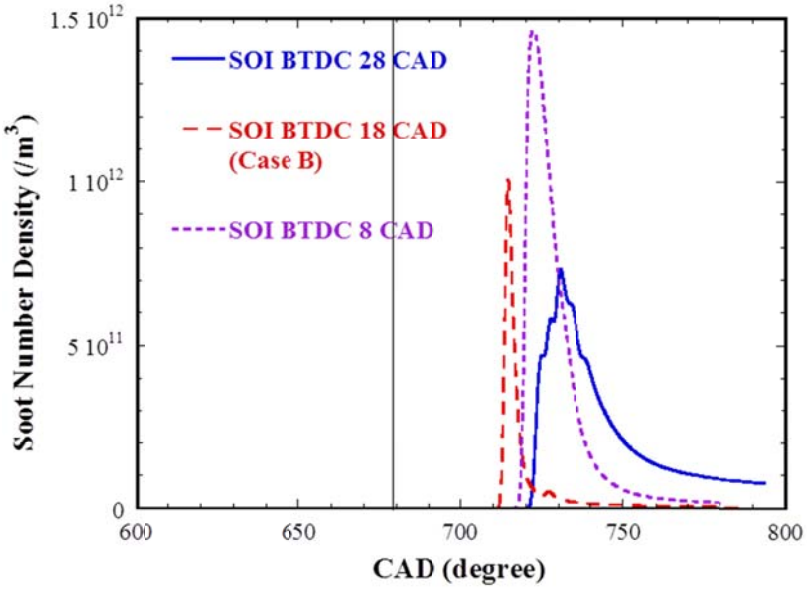

Figure 4.3.15 Soot number density comparison among case A, B, and C according to the crank angle degree

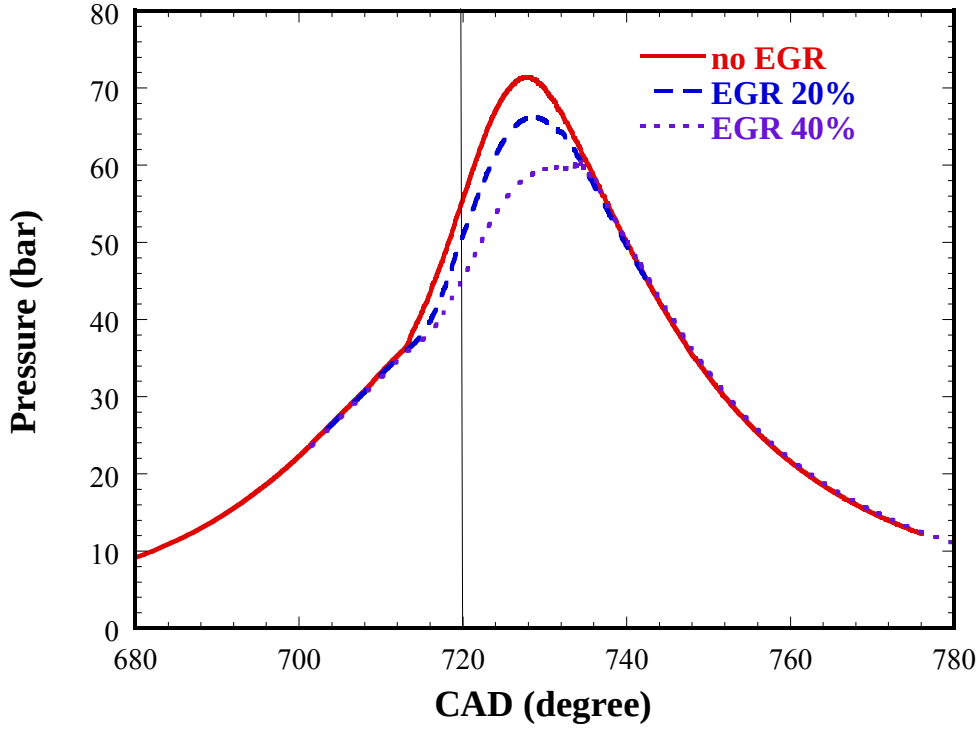

Figure 4.3.16 Pressure comparison among the cases of EGR 0%, 20% and 40% according to the crank angle degree

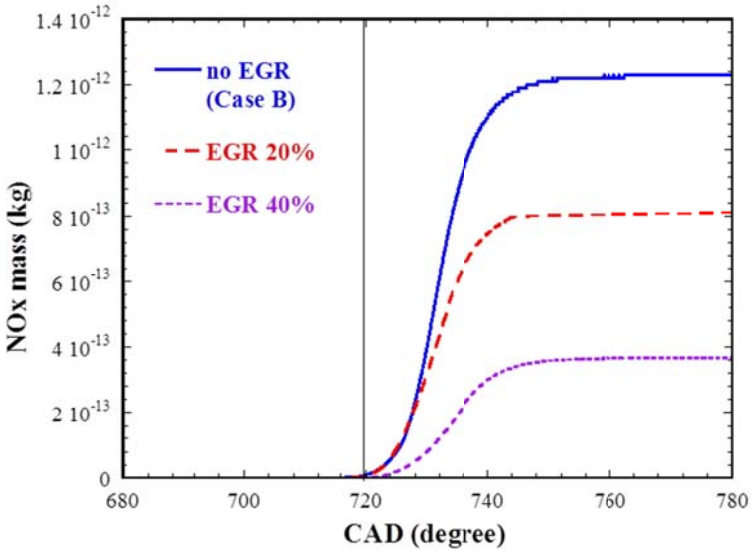

Figure 4.3.17 NOx emissions comparison among the cases of EGR 0%, 20% and 40% according to the crank angle degree

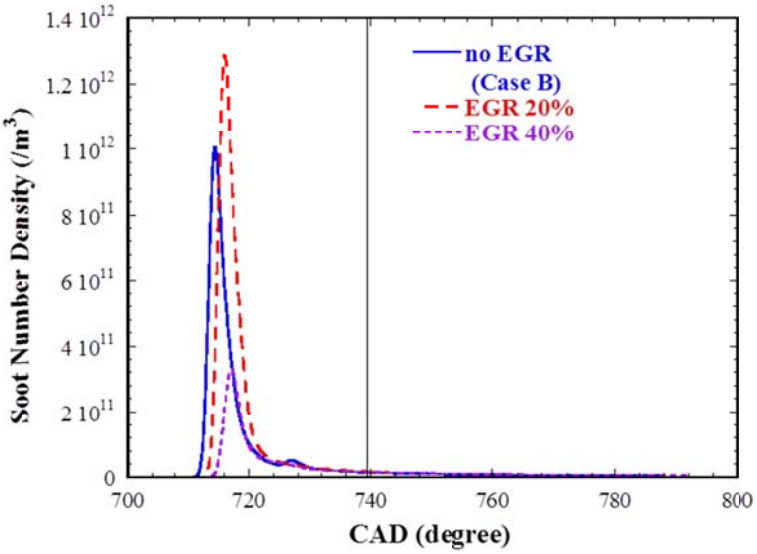

Figure 4.3.18 Soot number density comparison among the cases of EGR 0%, 20% and 40% according to the crank angle degree

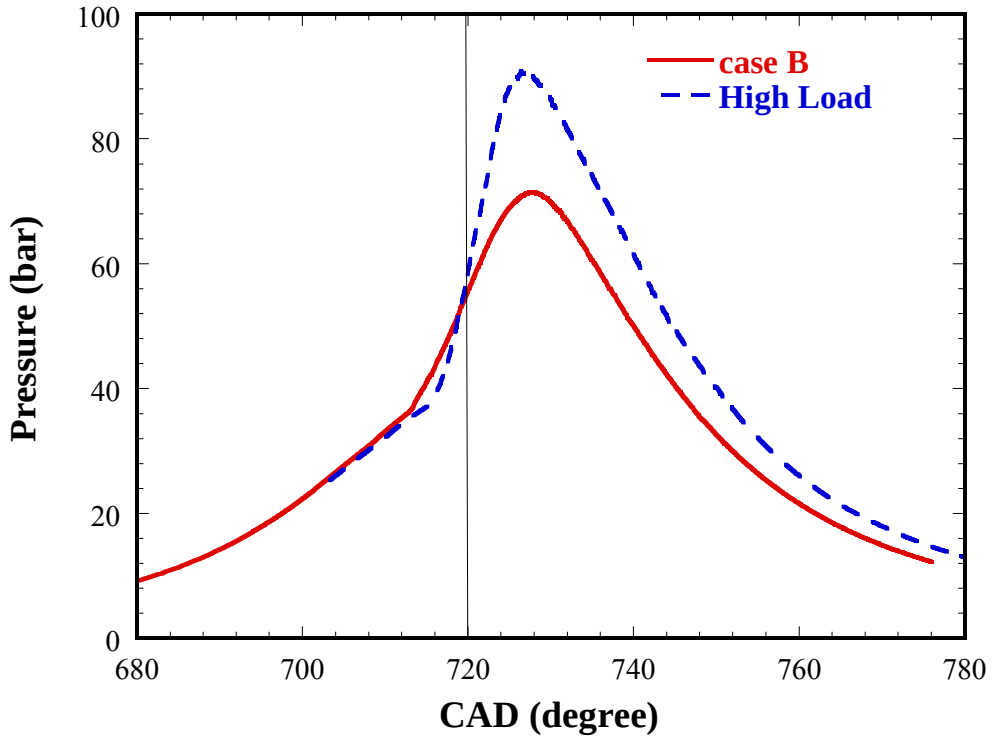

Figure 4.3.19 Pressure comparison between the case B and high load condition according to the crank angle degree

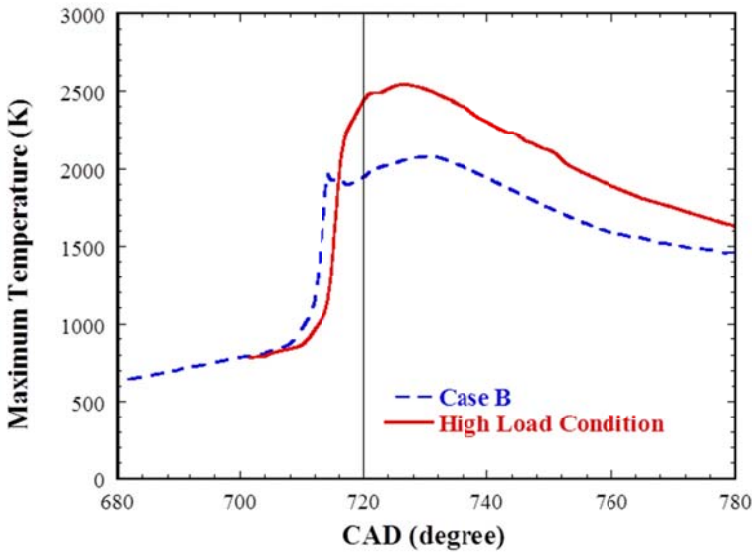

Figure 4.3.20 NOx emissions comparison between the case B and high load condition according to the crank angle degree

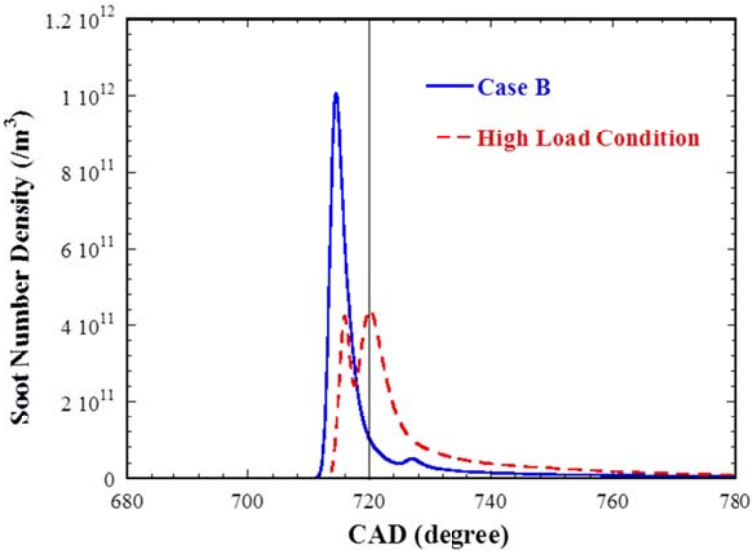

Figure 4.3.21 Soot number density comparison between the case B and high load condition according to the crank angle degree

Chapter 5. Conclusions

In this study, the combustion process and emissions production in a dual-fuel combustion engine were modeled by combining and modifying the laminar flamelet model for diffusion flame and level-set model for premixed flame, and the results of three dimensional simulations performed in an 1/8 engine geometry were compared to the experimental data.

For the modeling of non-premixed combustion of the higher reactivity fuel, laminar flamelet model was adopted in this study. In conventional laminar flamelet model for diffusion flame, a fuel is distributed along the mixture fraction and oxidizer is also distributed along the mixture fraction. However, at dual-fuel combustion, laminar flamelet model should be modified because one more fuel (lower reactivity fuel) exists in a dual-fuel engine. Generally, the lower reactivity fuel is injected at the early timing. Therefore, we assumed that the lower reactivity fuel is well mixed to the in-cylinder air and modified the laminar flamelet model to have one more reactant.

For the modeling of turbulent flame propagation, level-set model was adopted in this study. The ignition points are generated by the laminar flamelet model. To apply the turbulent burning velocity of the lower reactivity fuel, its laminar flame speed library was pre-calculated by CHEMKIN method with the detailed chemical kinetics of lower reactivity fuel in a wide range of temperature, pressure and equivalence ratio conditions. Based on the laminar flame speed and instantaneous turbulent flow field, turbulent burning velocity was calculated.

For the determinacy of species concentration at the burned region and flame sheet, conventional models use the simple method: only O2 and fuel was considered for lean and rich burned mixture, respectively. However, the actual chemical state of burned gas was found to be much more complicated according to

the equivalence ratio. Therefore, the burned gas species are calculated using the flamelet model with the detailed chemical kinetics of lower reactivity fuel. According to the fast chemistry assumption, solution sets of steady flamelet equation were obtained rather than solving the transient equation. Therefore, we can use the steady-state solution which is pre-calculated in the wide range of temperature, equivalence ratio and scalar dissipation rate. In this method, no additional time cost is needed during the actual CFD run time.

These models are coupled to describe the dual-fuel combustion. The flame propagation speed is determined the larger speed between the ignition propagation speed of the mixed fuel and the turbulent burning velocity of the lower reactivity fuel. The NOx formation process was modeled by extended Zeldovich mechanism, which was widely used for prediction of thermal NOx formation in internal combustion engines. To match with the experimental results, some of collision frequency factor was adjusted. The soot formation process was modeled by a phenomenological model, which took account the physics of particle inception, growth, oxidation and coagulation with global reaction rate expression. This model was originally proposed for Diesel combustion, but applied to dual-fuel combustion engine simulation with some adjustments in reaction rate constants. THC and CO emissions are calculated and post-processed from the chemical kinetics of fuels which are used in this study.

The developed model was firstly applied to a simple geometry to investigate the flame propagation speed. In this simulation, the ignition propagation speed was investigated with the mixed fuel. And then, the level-set model coupled with the laminar flamelet model was applied to the simulation. In this calculation, the turbulent burning velocity was investigated. After that, combustion and emission simulations were performed in a three dimensional engine mesh with 1500 rpm and bmep 4 of operating conditions. In this condition, cylinder pressure curve predicted by CFD simulation showed very good agreement with the experimental data. The emission data was also compared between simulation and experiment at Diesel CI

combustion and dual-fuel combustion conditions. There were general trend for NOx and soot emissions to decrease with dual-fuel combustion, while THC was correlated inversely. Although there were some quantitative discrepancies between experimentally measured emission data and simulation results, their general trends was well captured by the emission model.

Finally, the engine operating conditions are modified numerically such as injection timing, EGR rate, and propane mass to verify the effects of operating conditions in dual-fuel combustion. At first, injection timing was swung by 10^{o} compared to the basic condition, SOI 18^{o} BTDC. As the results, the combustion characteristics seem to be different in these cases. The classical dual-fuel combustion behaviors were seen in SOI 8^{o} and 18^{o} BTDC cases however, RCCI combustion behavior was observed for the SOI 28^{o} BTDC injection case. And next, three different EGR conditions (0, 20, 40%) are applied to the dual-fuel combustion. From the result, high EGR rate could be a key of PCCI combustion in dual-fuel combustion. Therefore, applying optimized injection timing and EGR rate could make dual-fuel combustion to RCCI combustion. RCCI combustion produced the smallest NOx and soot emissions compared to the classical dual-fuel combustion. However, soot emissions in RCCI combustion showed the worst coagulation rate due to the well mixed fuels. For the high load condition with additional propane, ignition timing was delay due to the specific heat constant of the additional propane but the combustion behavior was not changed. NOx and soot emissions are increased as additional propane mass.

Bibliography

1. Takagi, Y., et al., *Simultaneous Attainment of Low Fuel Consumption, High Output Power and Low Exhaust Emissions in Direct-Injection SI Engines (980149).* PROGRESS IN TECHNOLOGY, 2000. **80**: p. 45-54.
2. Koike, M., et al., *Research and Development of a New Direct Injection Gasoline Engine, SAE Paper 2000-01-0530.*
3. Stan, C., *Direct injection systems for spark-ignition and compression-ignition engines*. 1999.
4. Chen, S.K., *Simultaneous Reduction of NO~ x and Particulate Emissions by Using Multiple Injections in a Small Diesel Engine.* SAE transactions, 2000. **109**(3): p. 2127-2136.
5. Benajes, J., S. Molina, and J.M. García, *Influence of pre-and post-injection on the performance and pollutant emissions in a HD Diesel engine.* SAE paper, 2001: p. 01-0526.
6. Badami, M., et al., *Influence of multiple injection strategies on emissions, combustion noise and BSFC of a DI common-rail Diesel engine.* SAE TRANSACTIONS, 2002. **111**(3): p. 1118-1129.
7. Mori, K., et al., *Technology for Environmental Harmonization and Future of the Diesel Engine.* SAE Technical Paper 2009-01-0318, 2009.
8. Kimura, S., et al., *Ultra-clean combustion technology combining a low-temperature and premixed combustion concept for meeting future emission standards.* SAE TRANSACTIONS, 2001. **110**(4): p. 239-246.
9. Hardy, W.L., *An experimental investigation of advanced Diesel combustion strategies for emissions reductions in a heavy-duty Diesel engine at high speed and medium load*, 2005, University of Wisconsin--Madison.
10. Stanglmaier, R.H. and C.E. Roberts, *Homogeneous charge compression ignition (HCCI): benefits, compromises, and future engine applications.* SAE Paper 1999013682, 1999. **1999**.

11. Hasegawa, R. and H. Yanagihara, *HCCI combustion in Dl Diesel engine.* SAE transactions, 2003. **112**(3): p. 1070-1077.
12. Tsolakis, A. and A. Megaritis, *Partially premixed charge compression ignition engine with on-board H2 production by exhaust gas fuel reforming of Diesel and bioDiesel.* International journal of hydrogen energy, 2005. **30**(7): p. 731-745.
13. Lee, C.S., K.H. Lee, and D.S. Kim, *Experimental and numerical study on the combustion characteristics of partially premixed charge compression ignition engine with dual fuel< sup> ☆</sup>*. Fuel, 2003. **82**(5): p. 553-560.
14. Lee, S., H. Choi, and J. Chung, *The Effects of Injection Timing and Piston Bowl Shape on PHCCI Combustion with Split injections.* SAE Technical Paper, 2010: p. 01-0359.
15. Liu, Z., *An examination of the combustion characteristics of compression ignition engines fuelled with gaseous fuels*. 1995: Mechanical Engineering, University of Calgary.
16. Selim, M.Y.E., *Sensitivity of dual fuel engine combustion and knocking limits to gaseous fuel composition.* Energy conversion and management, 2004. **45**(3): p. 411-425.
17. Uma, R., T. Kandpal, and V. Kishore, *Emission characteristics of an electricity generation system in Diesel alone and dual fuel modes.* Biomass and Bioenergy, 2004. **27**(2): p. 195-203.
18. Papagiannakis, R. and D. Hountalas, *Combustion and exhaust emission characteristics of a dual fuel compression ignition engine operated with pilot Diesel fuel and natural gas.* Energy Conversion and Management, 2004. **45**(18): p. 2971-2987.
19. Mansour, C., et al., *Gas–Diesel (dual-fuel) modeling in Diesel engine environment.* International journal of thermal sciences, 2001. **40**(4): p. 409-424.
20. Nwafor, O., *Combustion characteristics of dual-fuel Diesel engine using pilot injection ignition.* Journal of the Institution of Engineers(India), Part MC, Mechanical Engineering Division, 2003. **84**: p. 22-25.

21. Abd Alla, G., et al., *Effect of injection timing on the performance of a dual fuel engine.* Energy conversion and Management, 2002. **43**(2): p. 269-277.
22. Krishnan, S.R., et al., *Strategies for reduced NOx emissions in pilot-ignited natural gas engines.* Journal of engineering for gas turbines and power, 2004. **126**(3): p. 665-671.
23. Selim, M.Y.E., *Pressure–time characteristics in Diesel engine fueled with natural gas.* Renewable energy, 2001. **22**(4): p. 473-489.
24. Nwafor, O.M.I., *Effect of advanced injection timing on the performance of natural gas in Diesel engines.* Sadhana, 2000. **25**(1): p. 11-20.
25. Curran, S.J., et al., *In-cylinder fuel blending of gasoline/Diesel for improved efficiency and lowest possible emissions on a multi-cylinder light-duty Diesel engine.* SAE Technical Paper, 2010: p. 01-2206.
26. Kokjohn, S., et al., *Fuel Reactivity Controlled Compression Ignition (RCCI) Combustion in Light-and Heavy-Duty Engines.* SAE International Journal of Engines, 2011. **4**(1): p. 360-374.
27. Hanson, R., et al., *Fuel Effects on Reactivity Controlled Compression Ignition (RCCI) Combustion at Low Load.* SAE International Journal of Engines, 2011. **4**(1): p. 394-411.
28. Nieman, D.E., A.B. Dempsey, and R.D. Reitz, *Heavy-Duty RCCI Operation Using Natural Gas and Diesel.* 2012.
29. Hanson, R., et al., *Piston Bowl Optimization for RCCI Combustion in a Light-Duty Multi-Cylinder Engine.* 2012.
30. Splitter, D., S. Kokjohn, and R. Reitz, *Effect of Compression Ratio and Piston Geometry on RCCI Load Limits and Efficiency.* 2012.
31. Castagné-IFP, M., et al., *Advanced tools for analysis of gasoline direct injection engines.* SAE Technical Paper, 2000: p. 01-1903.
32. Sinha, N., et al., *Efficient CFD Simulations for In-Cylinder Flows Using Hybrid Grids.* SAE Technical Paper, 1999: p. 01-1184.
33. Ge, H., et al., *Engine development using multi-dimensional CFD and computer optimization.* SAE Technical Paper, 2010: p. 01-0360.

34. Zhang, Y., S.C. Kong, and R. Reitz, *2003-01-0755 Modeling and Simulation of a Dual Fuel (Diesel/Natural Gas) Engine With Multidimensional CFD.* SAE SP, 2003: p. 107-118.
35. Tamagna, D., Y. Ra, and R. Reitz, *Multidimensional Simulation of PCCI Combustion Using Gasoline and Duel-Fuel Direct Injection with Detailed Chemical Kinetics.* SAE paper, 2007: p. 01-0190.
36. Kokjohn, S.L., et al., *Experiments and Modeling fo Dual-Fuel HCCI and PCCI Combustion using In-Cylinder Fuel Blending.* SAE 2009, 2009. **2009-01-2647**.
37. Splitter, D., et al., *Effect of Compression Ratio and Piston Geometry on RCCI Load Limits and Efficiency.* SAE Technical Paper, 2012: p. 01-0383.
38. Shi, Y., R.P. Hessel, and R.D. Reitz, *An adaptive multi-grid chemistry (AMC) model for efficient simulation of HCCI and DI engine combustion.* Combustion Theory and Modelling, 2009. **13**(1): p. 83-104.
39. Shi, Y., et al., *Efficient multidimensional simulation of HCCI and DI engine combustion with detailed chemistry.* SAE paper, 2009: p. 01-0701.
40. Pettinger, T. *http://www.economicshelp.org/blog/583/oil/why-is-the-price-of-oil-rising/*. 2008.
41. Eminox. *http://www.eminox.com/europe-on-road-emissions-regulations/*.
42. Karim, G.A., *A review of combustion processes in the dual fuel engine--The gas Diesel engine.* Progress in Energy and Combustion Science, 1980. **6**(3): p. 277-285.
43. Carlucci, A.P., D. Laforgia, and R. Saracino, *Effects of in-Cylinder Bulk Flow and Methane Supply Strategies on Charge Stratification, Combustion and Emissions of a Dual-Fuel DI Diesel Engine.* SAE Technical Paper, 2009: p. 01-0949.
44. Kokjohn, S., et al., *Investigation of Fuel Reactivity Stratification for Controlling PCI Heat-Release Rates Using High-Speed Chemiluminescence Imaging and Fuel Tracer Fluorescence.* SAE International Journal of Engines, 2012. **5**(2): p. 248-269.
45. Ma, Z., et al., *Combustion and emission characteristics of a Diesel engine fuelled with Diesel-propane blends.* Fuel, 2008. **87**(8-9): p. 1711-1717.
46. Hountalas, D. *The effect of operating parameters on the net and gross heat release rates of a direct injection Diesel engine*. 1994.

47. Kusaka, J., et al., *Combustion and exhaust gas emission characteristics of a Diesel engine dual-fueled with natural gas.* JSAE review, 2000. **21**(4): p. 489-496.
48. Sahoo, B., N. Sahoo, and U. Saha, *Effect of engine parameters and type of gaseous fuel on the performance of dual-fuel gas Diesel engines--A critical review.* Renewable and Sustainable Energy Reviews, 2009. **13**(6-7): p. 1151-1184.
49. Karim, G., Z. Liu, and W. Jones, *Exhaust emissions from dual fuel engines at light load.* SAE paper, 1993. **932822**.
50. Curran, S.J., et al., *In-cylinder fuel blending of gasoline/Diesel for improved efficiency and lowest possible emissions on a multi-cylinder light-duty Diesel engine.* SAE paper, 2010: p. 01-2206.
51. Peters, N., *Four lectures on turbulent combustion.* ERCOFTAC Summer School, Aachen, 1997.
52. Pope, S.B., *Turbulent flows*. 2000: Cambridge university press.
53. Tennekes, H. and J.L. Lumley, *A first course in turbulence*. 1972: The MIT press.
54. Jones, W.P., *Turbulence Modeling and Numerical Solution Methods for Variable Density and Combusting Flows.* Turbulent Reacting Flows, Academic Press., 1994: p. 309-374.
55. Boussinesq, J., *Théorie de l'écoulement tourbillant.* Mem. Présentés par Divers Savants Acad. Sci. Inst. Fr, 1877. **23**(46-50): p. 6.5.
56. Launder, B. and B. Sharma, *Application of the energy-dissipation model of turbulence to the calculation of flow near a spinning disc.* Letters Heat Mass Transfer, 1974. **1**: p. 131-137.
57. Yakhot, V., et al., *Development of turbulence models for shear flows by a double expansion technique.* Physics of Fluids A: Fluid Dynamics, 1992. **4**(7): p. 1510-1520.
58. Fan, L., et al., *Modeling fuel preparation and stratified combustion in a gasoline direct injection engine.* SAE paper, 1999: p. 01-0175.
59. Fan, L., R.D. Reitz, and N. Trigui, *Intake flow simulation and comparison with PTV measurements.* SAE paper, 1999: p. 01-0176.

60. Han, Z. and R.D. Reitz, *Turbulence modeling of internal combustion engines using RNG κ-ε models.* Combustion Science and Technology, 1995. **106**(4-6): p. 267-295.
61. Peters, N. and A. Kanury, *Turbulent combustion.* Applied Mechanics Reviews, 2001. **54**: p. B73.
62. Juneja, A. and S. Pope, *A DNS study of turbulent mixing of two passive scalars.* Physics of Fluids, 1996. **8**: p. 2161.
63. Peters, N., *Length scales in laminar and turbulent flames.* Numerical approaches to combustion modeling(A 92-16977 04-25). Washington, DC, American Institute of Aeronautics and Astronautics, Inc., 1991, 1991: p. 155-182.
64. Seshadri, K., N. Peters, and F. Williams, *Asymptotic analyses of stoichiometric and lean hydrogen-air flames.* Combustion and flame, 1994. **96**(4): p. 407-427.
65. Peters, N. and F.A. Williams, *Lift-off characteristics of turbulent jet diffusion flames.* AIAA Pap.;(United States), 1982. **82**(CONF-820106-).
66. Peters, N. and F. Williams, *The asymptotic structure of stoichiometric methane---air flames.* Combustion and Flame, 1987. **68**(2): p. 185-207.
67. Peters, N., *Laminar diffusion flamelet models in non-premixed turbulent combustion.* Progress in Energy and Combustion Science, 1984. **10**(3): p. 319-339.
68. Hergart, C. and N. Peters, *Applying the representative interactive flamelet model to evaluate the potential effect of wall heat transfer on soot emissions in a small-bore direct-injection Diesel engine.* Journal of engineering for gas turbines and power, 2002. **124**: p. 1042.
69. Hellstrom, T., *RIF implementation and testing*, 1997, Technical Report 01.07. 1996-31.12. 1996, Diesel, Technical Report.
70. Pitsch, H. and N. Peters, *A consistent flamelet formulation for non-premixed combustion considering differential diffusion effects.* Combustion and Flame, 1998. **114**(1-2): p. 26-40.
71. Lim, J., S. Lee, and K. Min, *Combustion Modeling of Split Injection in HSDI Diesel Engines.* Combustion Science and Technology, 2010. **183**(2): p. 180-201.

72. Abraham, J., F. Williams, and F. Bracco, *Discussion of turbulent flame structure in premixed charges. 1985 SAE Congress, Paper No. 850345*, 1985, Princeton Univ., NJ (USA). Dept. of Mechanical and Aerospace Engineering.
73. Weller, H., et al. *Prediction of combustion in homogeneous-charge spark-ignition engines*. 1994.
74. Weller, H.M., et al. *Validation of SI combustion model over range of speed, load, equivalence ratio and spark timing*. 1998. Citeseer.
75. Sussman, M., et al., *An improved level set method for incompressible two-phase flows.* Computers & Fluids, 1998. **27**(5-6): p. 663-680.
76. Williams, F., *Turbulent combustion.* the Mathematics of combustion, 1985: p. 97-131.
77. Patterson, M.A. and R.D. Reitz, *Modeling the effects of fuel spray characteristics on Diesel engine combustion and emissions.* 1998.
78. Matalon, M. and B. Matkowsky, *Flames as gasdynamic discontinuities.* Journal of Fluid Mechanics, 1982. **124**(1): p. 239-259.
79. SETHIAN, J., *LEVEL SET METHODS: EVOLVING INTERFACES IN GEOMETRY, FLUID MECHANICS*. 1999.
80. Ewald, J., *A level set based flamelet model for the prediction of combustion in homogeneous charge and direct injection spark ignition engines*. 2006: Cuvillier.
81. Bounaceur, R., et al., *Modeling the Laminar Flame Speed of Natural Gas and Gasoline Surrogates.* SAE Technical Paper, 2010: p. 01-0546.
82. Kee, R.J., et al., *PREMIX: a Fortran program for modeling steady laminar one-dimensional premixed flames.* Sandia report SAND85-8240, 1985.
83. Kee, R., et al., *FORTRAN computer code package for the evaluation of gas-phase multi-component transport properties. Sandia Labs*, 1986, TR SAND86-8246.
84. Kee, R.J., et al., *CHEMKIN-III: A FORTRAN chemical kinetics package for the analysis of gas-phase chemical and plasma kinetics*. 1996: Sandia National Laboratories Livermore, CA.

85. Kwon, H., *Combustion and Emission Modeling of a Direct Injection Spark Ignition Engine by Combining Flamelet Models for Premixed and Diffusion Flame.* Ph.D thesis, 2011.
86. Peters, N., *The turbulent burning velocity for large-scale and small-scale turbulence.* Journal of Fluid Mechanics, 1999. **384**(1): p. 107-132.
87. Chen, M., M. Herrmann, and N. Peters, *Flamelet modeling of lifted turbulent methane/air and propane/air jet diffusion flames.* Proceedings of the Combustion Institute, 2000. **28**(1): p. 167-174.
88. Hu, B. and C.J. Rutland, *Flamelet modeling with LES for Diesel engine simulations.* SAE paper, 2006: p. 01-0058.
89. Toninel, S., et al., *Implementation and Validation of the G-equation Model Coupled with Flamelet Libraries for Simulating Premixed Combustion in IC Engines.* SAE International Journal of Engines, 2009. **2**(1): p. 674-690.
90. Lee, K., Y. Kim, and K. Min, *Development of a reduced chemical kinetic mechanism for a gasoline surrogate for gasoline HCCI combustion.* Combustion Theory and Modelling, 2010. **15**(1): p. 107-124.
91. Hiroyasu, H. *Diesel engine combustion and its modeling*. in *Proceedings of 1st International Symposium on Diagnostics and Modeling of Combustion in internal Combustion Engines. Tokyo, Japan*. 1985.
92. Fusco, A., A. Knox-Kelecy, and D. Foster. *Application of a phenomenological soot model to Diesel engine combustion*. in *International Symposium COMODIA*. 1994.
93. Tao, F., et al., *Nine-step phenomenological Diesel soot model validated over a wide range of engine conditions.* International Journal of Thermal Sciences, 2009. **48**(6): p. 1223-1234.
94. Bowman, C.T., *Kinetics of pollutant formation and destruction in combustion.* Progress in energy and combustion science, 1975. **1**(1): p. 33-45.
95. Sun, Y., *Diesel combustion optimization and emissions reduction using adaptive injection strategies (AIS) with improved numerical models*. 2007: ProQuest.
96. Spindt, R., *Air-fuel ratios from exhaust gas analysis.* SAE paper, 1965. **650507**(9).

97. Hergart, C., H. Barths, and N. Peters, *Modeling the combustion in a small-bore Diesel engine using a method based on representative interactive flamelets.* SAE paper, 1999: p. 01-3550.

초 록

혼소 연소는 두 가지의 연료를 따로 분사하여 두 번째 분사된 연료로부터 점화를 시키고 이로부터 첫 번째 분사된 연료를 착화시키는 방식이다. 액체 연료의 절감을 위해 혼소 연소 방식은 이전부터 꾸준히 연구되어 왔으며 최근 예혼합 압축착화 방식과 연계되어 다시 주목 받고 있어 이에 대한 연구가 활발히 진행되고 있다. 그러나 이에 대한 수치해석적 연구는 직접적인 화학반응 계산을 이용한 방식에 그치고 있어 계산 시간과 비용이 많이 들기 때문에 이를 줄이기 위한 연소 모델의 개발이 필요한 실정이다. 기존의 혼소 연소와 최근 각광받고 있는 RCCI 로 알려진 연소 방식은 연소 특성이 거의 동일하기 때문에 동일한 연소 모델을 적용 가능하다. 즉, 혼소 연소에서는 액체 연료, RCCI 에서는 고반응성 연료로부터 점화가 발생하며 이로부터 연소가 확장되는 특성을 보인다. 따라서 확산 화염의 연소 특성과 예혼합 화염의 연소 특성을 동시에 보이는 방식으로 정리할 수 있다. 이로부터 본 연구에서는 혼소 연소의 연소 및 배기 배출물 예측을 위해 확산 화염을 모사할 수 있는 화염소 모델과 예혼합 연소를 모사하기 위한 화염 전파 모델을 접목하여 적용하였다.

우선 화염편 모델을 도입하여 확산 연소 모델링을 모사하였다. 두 번째 분사된 연료는 점화 플러그의 도움 없이 고온고압의 조건에 의해 점화가 되며 또한 첫 번째 분사된 연료 역시 자발화될 가능성이 있기 때문에 이 역시 고려되었다. 두 번째 분사가 조기 분사가 되었을 때도 실린더 내부에서 다점 점화의 모사가 가능하다.

두 번째로 레벨셋 모델을 도입하여 점화된 부분에서 첫 번째 분사된 연료에 의한 화염 전파의 발생을 모사하였다. 이 화염 전파의 속도는 레벨셋 모델에서의 난류 화염 속도와 화염편 모델의 확산 화염의 전파 속도 중 더 빠른 속도로 결정된다. 또한 이 때 기연 영역과 화염 브러시의 화학종 농도는 화염편 모델에 의해 미리 계산된 화학종의 데이터베이스를 이용해 계산했다.

2 차원 평판 격자의 계산 결과를 통해 본 연구의 연소 모델이 혼소 연소의 화염 구조를 효과적으로 모사할 수 있음을 확인하였으며 3 차원 엔진 형상 계산 격자에서의 전산 유체 해석을 통해 이 모델의 결과를 실험과 비교하여 검증하였다. 2 개 운전 조건에서 예측된 연소압 곡선은 실험 결과와 잘 일치하였으며 배기 배출물 농도 역시 혼소 연소의 경향을 효과적으로 추종하고 있음을 확인하였다.

주요어 : 혼소 연소 엔진, 3 차원 전산 유체 해석, 화염소 모델, 레벨셋 모델, 질소 산화물, 입자상 물질, 혼소 연소 모델

학번 : 2008-30291